Advanced Fluorescence Lifetime Imaging and Spectroscopy Techniques for Biological Samples

Chung, Pei-Hua

Awarding institution:
King's College London

Title: Advanced Fluorescence Lifetime Imaging and Spectroscopy Techniques for Biological Samples

Author: Pei-Hua Chung

Advanced Fluorescence Lifetime Imaging and Spectroscopy Techniques for Biological Samples

Pei-Hua Chung

Physics Department

King's College London

A thesis submitted for the degree of

Doctor of Philosophy

March 2012

Abstract

Intracellular viscosity is correlated with cause of diseases, and it also affects the metabolism and chemical signalling. In this thesis, fluorescence-based studies were conducted on a fluorescent molecular rotor, BODIPY-C_{12}, which was used to measure the intracellular viscosity.

BODIPY-C_{12} is insensitive to the surrounding polarity using solvatochromic methods. It was demonstrated that the fluorescence lifetime of BODIPY-C_{12} in methanol/glycerol mixtures is related to viscosity via the Förster-Hoffmann equation, and the rotational correlation time depends on viscosity based on the Stokes-Einstein-Debye equation. The intracellular viscosity is measured via FLIM, time-resolved and steady-state fluorescence anisotropy. The relationship between the fluorescence lifetime and rotational correlation time of BODIPY-C_{12} in methanol/glycerol mixtures agrees with the combination of the Förster-Hoffmann equation and the Stokes-Einstein-Debye equation and is different to that of a rigid fluorophore. From the fluorescence imaging and counterstaining experiments, it appears that BODIPY-C_{12} is located in lipid droplets and the endoplasmic reticulum of cells. Particle tracking provided further evidence of lipid droplet staining. It seems that there are two different lifetimes in lipid droplets and the endoplasmic reticulum via time-resolved fluorescence anisotropy measurements, which indicate of two different environments for both locations. The lifetime is not a function of rotational correlation time for BODIPY-C_{12} in cells. An appropriate medium has to use to create a calibration of lifetime versus viscosity for measuring the microviscosity of cells. It is also found that BODIPY-C_{12} fails to measure viscosity in non-polar silicone oils.

In addition, spectroscopic studies of Nile red, Rhodamine 123, Pyrromethene 546 and BODIPY-C_{12} in methanol/glycerol mixtures were carried out to examine the relationship between the radiative rate constant and refractive index according to the Strickler-Berg equation and an advanced model by Toptygin et al. The transition dipole moment and the shape of the fluorophore can be analyzed using a model also by Toptygin et al.

Time-resolved fluorescence imaging and spectroscopy offer a very powerful and versatile method for applications in the life sciences.

Publications

1. K. Suhling, J. A. Levitt, P.-H. Chung, M. K. Kuimova, G. Yahioglu, Fluorescence Lifetime Imaging of Molecular Rotors in Living Cells, J. Vis. Exp. (60), e2925 (2012)
2. K. Suhling, N. I. Cade, J. A. Levitt, M. K. Kuimova, P.-H. Chung, G. Yahioglu, G. Fruhwirth, T. Ng and D. Richards, Chapter 7.2 Fluorescence Lifetime Imaging applied to Microviscosity Mapping and Fluorescence Modification Studies in Cells, Biomedical Imaging: The Chemistry of Labels, Probes and Contrast Agents, The Royal Society of Chemistry, 371-390 (2012)
3. J. A. Levitt, P.-H. Chung, M. K. Kuimova, G. Yahioglu, Y. Wang, J. Qu and K. Suhling, Fluorescence anisotropy of molecular rotors, Chem. Phys. Chem., 12, 662-672 (2011)
4. J. A. Levitt, P.-H. Chung, D. R. Alibhai and K. Suhling, Simultaneous measurements of fluorescence lifetimes, anisotropy, and FRAP recovery curves, SPIE proceeding paper 7902 (2011)
5. P.-H. Chung, J. A. Levitt, M. K. Kuimova, G. Yahioglu, and K. Suhling, Mapping intracellular viscosity by advanced fluorescence imaging of molecular rotors in living cells, SPIE proceeding paper 7903 (2011)
6. J. A. Levitt, M. K. Kuimova, G. Yahioglu, P.-H. Chung, K. Suhling, and D. Phillips, Fluorescence lifetime imaging of molecular rotors to map microviscosity in cells, Chinese Optics Letters, 8, 923 (2010)
7. J. A. Levitt, M. K. Kuimova, G. Yahioglu, P.-H. Chung, K. Suhling and David Phillips, Membrane-bound molecular rotors measure viscosity in live cells via fluorescence lifetime imaging, J. Phys. Chem. C, 113, 11634 (2009)

Presentations

1. P.-H. Chung, J. A. Levitt, M. K. Kuimova, G. Yahioglu and K. Suhling, Imaging intracellular viscosity of live cells by fluorescent molecular rotors, the 12th Conference on Methods and Applications of Fluorescence: Spectroscopy, Imaging and Probes (MAF-12),September 11-14, 2011, (Poster presentation)
2. P.-H. Chung, J. A. Levitt, M. K. Kuimova, G. Yahioglu and K. Suhling, Mapping intracellular viscosity by time-resolved imaging of fluorescence molecular rotors in living cells, Advanced photonics techniques in Biology conference, April 11, 2011, London, UK (Poster presentation)
3. P.-H. Chung, J. A. Levitt, M.. K. Kuimova, G. Yahioglu and K. Suhling, Mapping intracellular viscosity by advanced fluorescence imaging of molecular rotors in living cells, SPIE photonics West conference, January 22-27, 2011, San Francisco, USA (Oral presentation)
4. J. A. Levitt, P.-H. Chung, D. R. Alibhai, K. Suhling, Simultaneous measurements of fluorescence lifetime, anisotropy and FRAP recovery curves, SPIE photonics West conference, January 22-27, 2011, San Francisco, USA (co-author)
5. P.-H. Chung, J. A. Levitt, M. K. Kuimova, G. Yahioglu and K. Suhling, Mapping intracellular viscosity distribution by advanced fluorescence imaging of molecular rotors in living cell, Advanced imaging methods workshop, January 19-22, 2011, Berkeley, USA (Poster presentation, award)
6. P.-H. Chung, J. A. Levitt, M. K. Kuimova, G. Yahioglu and K. Suhling, Mapping viscosity in live cells by fluorescence lifetime imaging techniques, Photon 10, August 23-26, 2010, Southampton, UK (Poster presentation)
7. P.-H. Chung, J. A. Levitt, M. K. Kuimova, G. Yahioglu and K. Suhling, Multi-dimensional Fluorescence Spectroscopy and Imaging**,** Annual meeting of the physical society of Taiwan, February 2-4, 2010, Taiwan (Poster presentation, award)

Acknowledgements

I would like to thank all of the people listed below. Without all of your help and support, I would not be able to achieve this.

Thanks to Dr. Klaus Suhling, Dr. Simon Ameer-Beg, Dr. James A. Levitt and Dr. Marina K. Kuimova for your help and advice on the project, especially Dr. Klaus Suhling and Dr. James A. Levitt.

Thanks to Dr. Megan McMichael, Dr. Chiara Gattinoni, Nishanthan Srikantha, Dr. Mohd Norhakim Yahya and Dr. Ariadni Vergou for proof reading this thesis.

Thanks to Dr. Gokhan Yahioglu for providing me with the fluorescent molecules. Thanks to Dr. Baljinder Mankoo and Dr. Matthias Krause for providing me with HeLa cells.

Dr. Wayne Dickson, Frank Tung and Prof. Chia-Liang Cheng, your enthusiasm inspires me.

Thank you for your help in the lab, Bill Luckhurst, Ernest Samuel, John Wilkinson, Steve Whelan, Dr. Lior Eligal, Dr. Brad Littleton, Dr. Nicholas Cade and Dr. Susan Cox.

I am grateful to thank all my friends' encouragement throughout the years.

Ariadni, Chiara, I-Shan, Hui-Chun, YY, Sabrina, Carolin, Zoya, Jean-Sebastien, Daniel, Alessio, Anna, Arnaud, Manuela, Phillip, James, Selina, Nish, Shohei, Oomimm, Linden, Gianmarco, Spyridon, Julia, Paul and Giovanni thank you for having a good time during my PhD life.

Thanks to the Graduate School Studentship and Overseas Research Scholarship for the financial support.

Lastly and most important, I would like to thank Jhih-Sian, my sister, my brother and my parents for all the support.

I love you all.

Glossary of Acronyms

3T3	Embryonic Swiss Mouse Fibroblast cells
Adj. R-Square	Adjusted R-Square
AFM	Atomic Force Microscopy
AIDS	Acquired Immune Deficiency Syndrome
ATCC	American Type Culture Collection
BODIPY-C_{12}	Meso-Substituted Boron-Dipyrromethene
CCVJ	9-(2-Carboxy-2-Cyanovinyl)Julolidine
CHO	Chinese Hamster Ovary
CHO-K1	a subclone from the CHO cells
CV1	Normal African Green Monkey Fibroblast cells
COS-7	Cercopithecus Aethiops Fibroblast-like Kidney cells
DCVJ	4-(Dicyanovinyl)Julolidine
DFT	Density Functional Theory
DLPC	Dilauroylphosphatidylcholine
DMABN	4,4-Dimethylaminobenzonitrile
DMEM	Dulbecco's Modified Eagle's Medium
DPPC	Dipalmitoylphosphatidylcholine
EBCCD	Electron-Bombarded Charge-Coupled Device
ER	Endoplasmic Reticulum
ER-RFP	Endoplasmic Reticulum-Red Fluorescent Protein
EYFP	Enhanced Yellow Fluorescent Protein
(Tr-)FAIM	(Time-resolved) Fluorescence Anisotropy Imaging
FBS	Fetal Bovine Serum
FCS	Fluorescence Correlation Spectroscopy
FITC	Fluorescein isothiocyanate
FLIM	Fluorescence Lifetime Imaging
FRAP	Fluorescence Recovery After Photobleaching
FRET	Förster Resonance Energy Transfer
FWHM	Full Width at Half Maximum
GFP	Green Fluorescent Protein
H&E staining	Hematoxylin and Eosin staining
HeLa	Human Cervix Carcinoma cells
IRF	Instrument Response Function
LBR	Lamin-B Receptor
MDCK	Madin-Darby Canine Kidney Epithelial cells
NA	Numerical Aperture

NFLK	Norden Laboratories Feline Kidney cells
NSOM	Near-field Scanning Optical Microscopy
p-DASPMI	p-(dimethylamino) stilbazolium
PALM	Photoactivatable Localization Microscopy
PMT	Photomultiplier Tube
PM546	Pyrromethene 546
PtK1	Female Rat Kangaroo Kidney Epithelial cells
RBC(s)	Red Blood Cell(s)
Rh123	Rhodamine 123
ROI	Region of Interest
PSF	Point Spread Function
QD(s)	Quantum Dot(s)
QY	Quantum Yield
SEM	Scanning Electron Microscope
SD	Standard Deviation
SK-OV-3	Human Ovary Adenocarcinoma
SPAD	Single-Photon Avalanche Diode
SRß	Signal-Recognition-Particle Receptor
SIM	Structured-illumination Microscopy
STED	Stimulated Emission Depletion
STORM	Stochastic Optical Reconstruction Microscopy
TCSPC	Time Correlated Single Photon Counting
TEM	Transmission Electron Microscopy
TIRFM	Total Internal Reflection Fluorescence Microscopy
TM-BODIPY	3,3',4,4'-difluoro-1,3,5,7-tetramethyl-4a-aza-s-indacene

Contents

List of Figures

List of Tables

Chapter 1

Introduction

1.1 Fluorescence

The history of fluorescence can be traced back to a long time ago. Sir John Frederick William Herschel reported an observation of blue light from quinine in transparent and colourless tonic water under the sunlight.[1] Stokes termed this phenomenon as fluorescence.[2] The Jablonski diagram illustrates the mechanism of photoluminescence, which are fluorescence and phosphorescence, shown in Figure 1. 1.[3-5] The symbols S_0, S_1, T_1 refer to the ground state, first excited singlet state, and first excited triplet state, respectively. The singlet state is composed of electron pairs with opposite spin; the states with the unpaired spins according to the Pauli exclusion principle are called the triplet states.

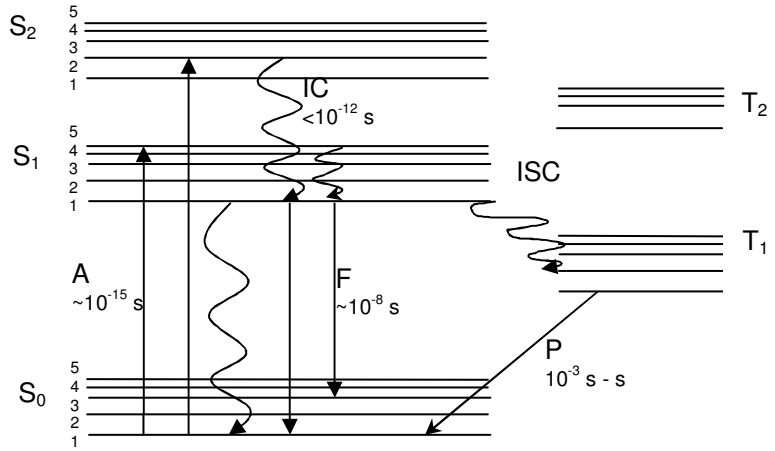

Figure 1. 1 Jablonski diagram showing a photon is absorbed (A: Absorption) and emitted via a radiative pathway (F: Fluorescence, and P: Phosphorescence) and non-radiative pathway (IC: Internal Conversion, and ISC: Intersystem Crossing). S denotes the singlet state and T is the triplet state.

When a light source illuminates fluorescent molecules, the ground-state molecules absorb energy and the molecules are excited to a higher energy state. The excited electrons release energy and return to the ground state through a series of events. First, the excited electrons undergo a transition from a higher vibrational to the lowest vibrational state of S_1 via vibrational relaxation or internal conversion which is a transition from S_2 to S_1. Both non-radiative processes take 10^{-12} seconds. Once the electron occupies the lowest vibrational level, it has few pathways to return to the ground state. A direct transition from S_1 to S_0 takes place via non-radiative decay or radiative pathway. The latter process releases energy via emitting light which is called fluorescence. The fluorescence wavelength is longer than the absorption wavelength due to the energy loss via vibrational relaxation or internal conversion. The wavelength difference between the absorption and emission band is known as the Stokes shift.

The electron in the lowest vibrational level also undergoes an intersystem crossing process to the triplet state. It takes a longer amount of time to return from T_1 to S_0, because this process is forbidden. The light emitted under this mechanism is called phosphorescence.

Each type of fluorescent molecule has its own unique spectroscopic properties, but sometime it is non-trivial to distinguish two species just by performing the analysis of spectra. Some spectra can have different lifetimes. Therefore, the fluorescence lifetime of the molecules is the average time in the excited state and is an important information. The fluorescence lifetime can be derived from the rate constants of non-radiative (k_{nr}) and radiative (k_r) pathways, is given by

$$\tau_f = \frac{1}{k_r + k_{nr}} \qquad (1.1)$$

The fluorescence intensity of a fluorophore is related to the efficiency of the fluorescence process called the fluorescence quantum yield. The fluorescence quantum yield of a fluorophore is the ratio of the number of photons emitted to the number of photons absorbed, and it defined as

$$\Phi = \frac{k_r}{k_r + k_{nr}} = \frac{\tau_0}{\tau_f} \qquad (1.2)$$

where τ_0 is the intrinsic or natural lifetime of a fluorophore. The value of $\Phi \leq 1$. τ_0 is the lifetime it has in absence of a non-radiative pathway, and its definition is given by

$$\tau_0 = \frac{1}{k_r} \qquad (1.3)$$

Prior to obtaining the extent of the fluorescence decay of a fluorophore, the knowledge of how molecules occupy a set of states is necessary. The population of electrons in vibration level of the ground state follows the Boltzmann distribution.[6]

$$\frac{N_2}{N_1} = e^{-(E_2 - E_1)/k_b T} \qquad (1.4)$$

where N_1 and N_2 present the number of molecules with energy E_1 and E_2, respectively, k_B is the Boltzmann constant and T is the absolute temperature.

The fluorescence decay is related to the number of molecules populating the excited state and to the rate of decay. The change of population of fluorophores in the excited state follows

$$\frac{dN(t)}{dt} = -(k_r + k_{nr})N(t) \qquad (1.5)$$

where $N(t)$ is the number of electrons in the excited state at time t after excitation. Thus the number of excited fluorophores can be written as eq. 1.6.

$$N(t) = N_0 e^{-t/\tau_f} \qquad (1.6)$$

In a time-resolved measurement, the fluorescence intensity is recorded rather than the number of excited fluorophores. Generally, their relationship is proportional. The fluorescence intensity can therefore be expressed as eq. 1.7.

$$I(t) = I_0 e^{-t/\tau_f} \qquad (1.7)$$

The photoluminescence mechanism and fluorescence properties are irrespective of how the molecules reach the excited states.[7] In other words, the molecule has no memory of how it gets into the excited state. The ground-state molecule absorbs the energy from one photon or multiple photons and undergoes a transition to the excited states. Therefore, the long wavelength light can still excite the electrons to the excited states. There are some requirements on multiphoton absorption. High-intensity excitation light is necessary to have measurable results. The probability of the two-photon absorption is quadratic of the excited light intensity according to Maria Göppert-

Mayer's work. The schematic for one-photon and multiphoton excitation is shown in Figure 1. 2.

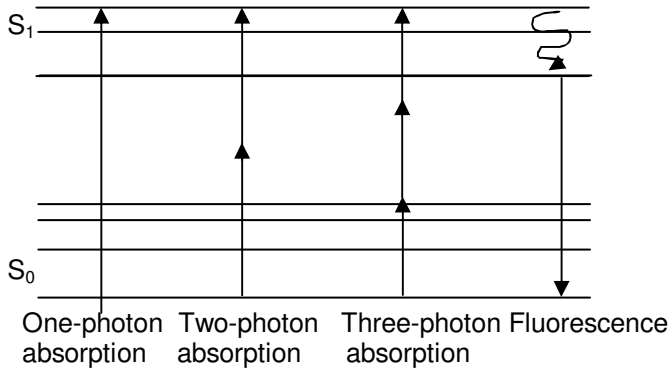

Figure 1. 2 Fluorescence following one-photon, two-photon and three-photon excitation.

The probability of molecules which can be excited via two-photon excitation is proportional to the power of the excitation light. Emission intensity is proportional to the number of molecules in the excited state. Thus, the relation between fluorescence and efficiency of two-photon excitation can be written as

$$I_e \propto \alpha \cdot P_{exc}{}^2 \tag{1. 8}$$

where I_e is fluorescence intensity, α is the absorption coefficient, and P_{exc} is the excitation power.

Fluorescence is an important characteristic, and it has been widely used in everyday life, such as fluorescent lamp, traffic signing, and anti-counterfeiting technologies on banknotes and credit card.[8] It has become also an important tool to study the biological environment when fluorescence is combined with microscopy.

1.2 Microscopy

Microscopy is a technique to image a specimen within a small scale that only can be visualized using a microscope. Microscopy can be classified into optical microscopy, electron microscopy, and scanning probe microscopy according to visualizing means.

The scanning probe microscope scans the surface of a sample using a probe tip. Atomic force microscopy (AFM) and near-field scanning optical microscopy (NSOM) are scanning probe microscopes. The electron microscopy image samples are illuminated by a beam of electrons, such as transmission electron microscopy (TEM) and scanning electron microscopy (SEM). In optical microscopy, images of samples are taken using visible light. It includes fluorescence microscopy and interference microscopy etc.

Electron microscopy offers a better imaging resolution, but the samples are imaged in vacuum. In order to have a high quality image, sample preparation is important. The electrical conductivity of the sample is crucial in SEM measurements. A coating thin layer of metal materials is needed for poor electrical conductivity samples. The specimen for TEM measurements should be thin enough to allow transmitting of electrons through the sample to form an image. Scanning probe microscopy only can image of surface of cells. However, optical microscopy can be used to image live cells and monitor the dynamic change of living cells. The study of cells via optical microscopy is therefore better than other microscopy. In this section, we focus on optical microscopy.

Optical microscopy has been developed since the 16th century. The Dutch spectacle makers Hans Janssen and his son Zacharias invented a compound microscope that magnified a small particle through two lenses in a tube.[9] Robert Hooke published a book called Micrographia which illustrated small insects and

cork cells using this microscope in 1665.[10] In the 19th century, Ernst Abbe described the diffraction theory of a point spread function (PSF) which is a response of an imaging system to a point source in a three-dimensional focus optical system. It limits the optical resolution.

The important feature of the optical systems is resolution, and there are different optical resolutions for each microscopy. The resolution is defined as the shortest distance between two point-like objects that can be resolved. It is related to the Airy disk and PSF that are limited by the diffraction of light. The diffraction pattern of a point object at a microscope image plane is called an Airy pattern. The bright region in the centre of Airy pattern is Airy disk which describe the best focused spot of light through a circular aperture. A pinhole diameter which is before the detection is set to allow the first order of the Airy pattern through an aperture to the detector is called 1 Airy unit. An illustration of Airy pattern and the limit of resolution are shown in Figure 1. 3. A representative PSF for a wide-field and a confocal microscope is shown in Figure 1. 4. The intensity around the bright centre reduces in confocal microscopy comparison to wide-field microscopy. The lateral and axial PSF of confocal microscopy is shorter by approximately 30% than that of wide-field microscopy.[11]

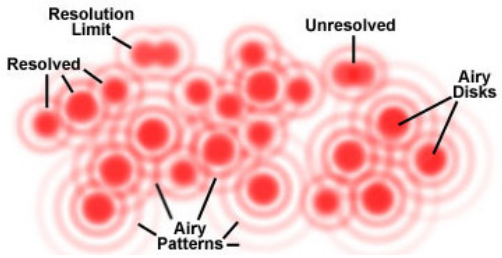

Figure 1. 3 An illustration of Airy disk, Airy pattern, and the limit of resolution.[12]

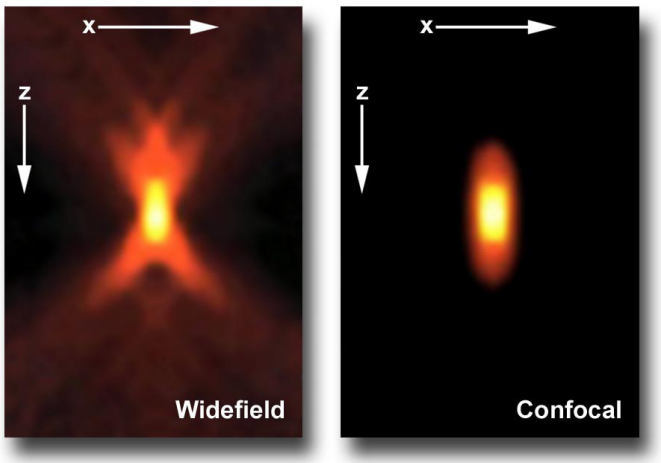

Figure 1. 4 An axial PSF for (left) wide-field and (right) confocal microscopy.[11]

The lateral (R_{xy}) resolution for wide field microscopy can be given by[11]

$$R_{xy} = \frac{0.6 \cdot \lambda}{NA} \tag{1. 9}$$

where λ is the wavelength of the illuminating light, and NA is the numerical aperture of the objective lens.

The lateral (R_{xy}) and axial (R_z) resolution for confocal microscopy can be estimated using eq. 1.10 and eq. 1.11, respectively.[11]

$$R_{xy} = \frac{0.4 \cdot \lambda}{NA} \tag{1. 10}$$

$$R_z = \frac{1.4 \cdot n \cdot \lambda}{NA^2} \tag{1. 11}$$

where n is the refractive index of medium between the objective lens and the sample, and other symbols are the same as eq. 1.9. Typically, the lateral and axial imaging resolution of conventional light microscopy is 200-300 nm and 500-700 nm, respectively.[13]

1.3 Fluorescence Microscopy

1.3.1 Fluorescence Microscopy

Fluorescence microscopy is a powerful tool in biology, medicine and materials sciences, [14] although the resolution of electron microscope is greater than that of optical microscopy. However, live cells cannot be measured using the electron microscope. The dynamic change of species can be monitored using fluorescence microscopy.[14-16] A sensor for pH,[17-19] ions,[20-23] oxygen,[24, 25] or temperature[26, 27] has been developed based on the intrinsic fluorescence property of a fluorophore. The discrimination between normal cells and cancer cells, [28, 29] the ability of drug delivery and the pathologies such as blood,[30] dental[31] and eye[32] are noninvasive medicine applications. In addition, fluorescence lifetime techniques also apply in other fields, e.g. analysis of artwork,[33] fluid mechanism,[34] forensic science,[35] combustion and anti-counterfeiting technologies.[8] Hematoxylin and Eosin (H&E) staining is a standard stain for cytoplasm and nuclei in histology. From the shape of organelles of a cell, suspected cancer cells can be identified and diagnosis can be made.

A short history of the development of fluorescence microscopy: due to the finding that the higher resolution results from the shorter wavelength light for the optical microscopy according to eq. 1.9, a UV Fluorescence microscope was developed by August Köhler. However he noticed longer wavelength light emitting from some objects which were illuminated with UV light. In 1911, Oskar Heimstädt constructed the first successful fluorescence microscope. Max Haitinger and other scientists stained samples with exogenous fluorescent

molecules. In 1929, Philipp Ellinger and August Hirt invented an intravital microscope which is known as a prototype of an epi-fluorescence microscope. A dichromatic mirror was invented and replaced some of the some components of the intravital microscope after 40 years.[36]

In 1959, a confocal scanning microscope was invented and has a better optical resolution,[37] due to the sample being scanned using a spot of focused light and detecting the fluorescence through a pinhole. The pinhole can remove the fluorescence from out-of-focus planes, and thus we can get high contrast (and a slightly higher resolution according to eq. 1.10) with depth selectivity. However confocal microscopy was not widely used for biological application until the 1980s.[38]

Confocal microscopy is a powerful fluorescence microscopy technique in biological systems as it provides a high axial resolution in depth and the signals from the different depth. Out-of-focus light does not reach the detector which allows imaging an optical section of samples. A basic scheme of confocal microscope is shown in Figure 1. 5. The laser beam is shone through the objective lens and illuminates the sample point by point. The fluorescence or scattering light are collected through back of the same objective lens, and recorded by a photomultiplier tube (PMT) detector. The signals are reconstructed with a computer, and a two-dimensional image of a specimen can be obtained by moving a sample or using laser scanning technique. It also can process a three-dimensional topology of objects by reconstructing two-dimensional images of a sample in the different z-axis positions.

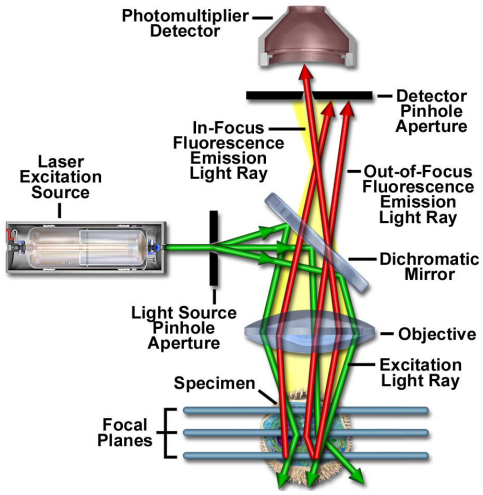

Figure 1. 5 The basic principle of a confocal microscope.[11]

1.3.2 Super-resolution Microscopy

Modern microscopy has developed toward super-resolution imaging. For example, total internal reflection fluorescence microscopy (TIRFM) employs an evanescent wave to excite a limited thickness of 100 nm of samples adjacent to the interface between two materials having different refractive indices.[39, 40] It provides a better resolution in the z-axis. 4Pi microscopy also provides a resolution of ~ 100 nm in the axial direction, and it not limited to interfaces. The concept is to coherently illuminate samples and collect fluorescence by two opposing high NA objective lenses.[13, 41] Structured illumination microscopy (SIM) employs a structured illumination pattern to observe a higher spatial frequency to achieve a better lateral resolution, e.g. the lateral resolution for non-linear SIM has been reported to be less than 50 nm.[42] Stimulated emission depletion (STED) microscopy involves two pulsed lasers. The first laser is used to excite fluorescent molecules in focal volume, and the second laser with a doughnut shape is used to depopulate the excited state to ground state via stimulated emission. It results in a small focused light spot to excite fluorophores and provide a lateral resolution of ~20 nm.[43] A better lateral resolution of up to 5.8 nm can be achieved.[44] Photoactivatable localization microscopy (PALM) achieves 20-50 nm resolution.[40, 45] Stochastic optical reconstruction microscopy (STORM) provides the lateral and axial resolution of ~30 nm and ~50 nm, respectively.[46] PALM and STORM use photoswitchable fluorescent molecules

that can be switched on and off via light at a wavelength different from the imaging light and imaging light, respectively. The centroid position of each fluorescent pair can be analyzed via fitting the PSF to a two-dimensional Gaussian function. A better resolution can be achieved with these processes,[47] and has recently been applied to living cells.[48] A brief comparison of microscopy is shown in Table 1. 1.

Table 1. 1 Summary of resolution for different types of microscopy.

		Resolutions
Optical microscopy	Wide field	Lateral resolution: 200-300 nm
	Confocal	Lateral resolution: 200-300 nm Axial resolution: 500-700 nm[13]
	TIRF	Lateral resolution: 200-300 nm Axial resolution: 100 nm[39, 40]
	STED	Lateral resolution: ~20 nm[43]
	PALM	Lateral resolution: 20-50 nm[40, 45]
	STORM	Lateral resolution: ~30 nm Axial resolution: ~50 nm[46]
Electron microscopy	TEM	0.05 nm
	SEM	< 1 nm
Scanning Probe microscopy	AFM	Lateral resolution: ~1 nm Vertical resolution: ~0.1 nm[49]
	NSOM	Lateral resolution: 20-50 nm[13]

There are some other fluorescence techniques based on fluorescence microscopy, e.g. fluorescence recovery after photobleaching (FRAP), fluorescence correlation spectroscopy (FCS), fluorescence lifetime imaging (FLIM), Förster resonance energy transfer (FRET) and fluorescence anisotropy. These techniques can provide spatial, spectral, time-resolved or polarization information of the fluorophores, and can be combined with super-resolution microscopy.[50]

1.3.3 Fluorescence Recovery after Photobleaching (FRAP)

The translational diffusion property of fluorescent molecules can be measured using FRAP. The intensity of fluorescent molecules in a region is monitored before and after a short burst of intense illumination bleaching a region irreversibly. The bleached molecules are unable to emit light. The fluorescent molecules around the bleaching area replace the bleached molecules via transitional diffusion. The time when the intensity recovers back to that in the beginning is used to determine the diffusion coefficient. A schematic of FRAP measurement with monitoring the intensity during the time is shown in Figure 1. 6. There are four stages, the first is pre-bleaching (1), following bleaching (2), recovery process (3) and then completed by the recovery process (4). The corresponding intensity F_1, F_0 and F_∞ are before bleaching, at bleaching moment, and at reaching equilibrium stage, respectively. From a FRAP curve, the immobile fraction can be seen if $F_\infty \neq F_1$ occurs.

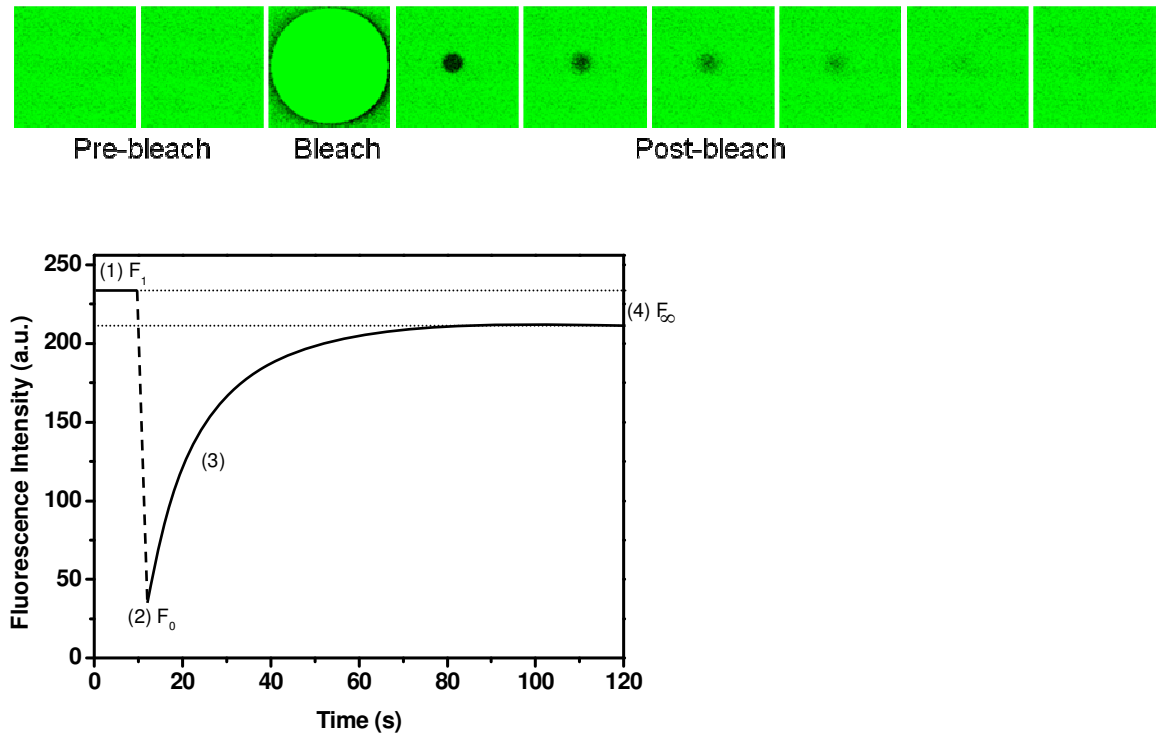

Figure 1. 6 An illustration of a typical FRAP experiment and the fluorescence intensity versus time. (1) denotes the pre-bleach intensity, (2) for bleaching, (3) for recovery process, and (4) reach a stabilized intensity.

The translational diffusion coefficient D_{trans} , can be calculated using the following equation for excitation and monitoring with a Gaussian profile.[51]

$$D_{trans} = \frac{0.88 \cdot w^2}{4\tau_{1/2}} \quad (1.\ 12)$$

where w is the radius of the bleached area and $\tau_{1/2}$ is the recovery half-time which is the time required for the intensity reaching half of the stabilized intensity. The diffusion time, τ_D , can be analyzed from the FRAP curve by fitting an exponential function.[52]

$$I(t) = A \cdot (1 - e^{-t/\tau_D}) + C \quad (1.\ 13)$$

where I is the fluorescence intensity, C is the first intensity measured after bleaching, and A is the stabilized intensity minus the value of C . In other words, C is F_0 and A is $F_\infty - F_0$ in Figure 1. 6. The translational diffusion coefficient can be written as[51]

$$D_{trans} = \frac{w^2}{4\tau_D} \quad (1.\ 14)$$

1.3.4 Fluorescence Correlation Spectroscopy (FCS)

Fluorescence correlation spectroscopy measures fluctuations in fluorescence within a small focal volume. The intensity fluctuations result from the diffusion of fluorescent molecules in and out of the focal volume, chemical reaction kinetics varying the mobility or conformational change of macromolecules causing the different intensities.[53, 54] It has been used to study the concentrations,

interactions and internal dynamics of molecules at nanomolar concentrations in living cells.[53, 55, 56]

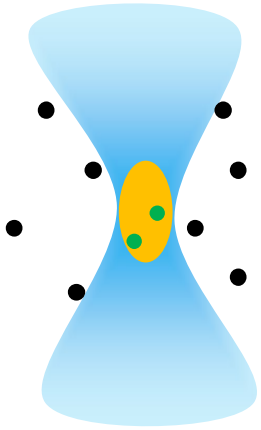

Figure 1. 7 Schematic of FCS measurement. The focus light (blue) excites the fluorescent molecules (green) in an observation focal volume (yellow). The black points denote the non-excited fluorescent molecules.

The translational diffusion of molecules can be analyzed from the normalized autocorrelation function, $G(\tau)$, which is related to the fluorescence intensity I at a time t to that τ seconds later. The autocorrelation function is given by[53]

$$G(\tau) = \frac{< I(t) \cdot I(t+\tau) >}{< I >^2} = 1 + \frac{< \delta I(t) \cdot \delta I(t+\tau) >}{< I >^2} \qquad (1.\ 15)$$

where $< I >$ is the mean value, and $\delta I(t)$ and $\delta I(t+\tau)$ are fluorescence intensity fluctuations at a time t and $t+\tau$ respectively.

Many processes take place at different time scales, such as triplet state transitions, different types of diffusion motion, and thus the knowledge of time scales of processes is needed to carefully interpret the autocorrelation curve.[57]

1.3.5 Fluorescence Lifetime Imaging (FLIM)

FLIM is a technique used to form an image based on the fluorescence lifetime of fluorophores. Each pixel of an image contains a fluorescence decay of fluorescent molecules. The fluorescence lifetime can be analyzed by fitting the decay to an exponential function. In addition, the integration of decay denotes the fluorescence intensity.

An example of a fluorescence lifetime image is processed via SPCImage shown in Figure 1. 8. The left top panel denotes the fluorescence intensity image, and shows how the fluorophore is distributed. The brighter regions present more fluorescence. The middle top image is FLIM. The shorter fluorescence lifetime of the fluorescent molecule is in blue and the longer lifetime is in red. A colour scale is related to the fluorescence lifetime, shown in the right top panel. The bottom panel shows the fluorescence decay and the fitting result in the cross of two blue lines.

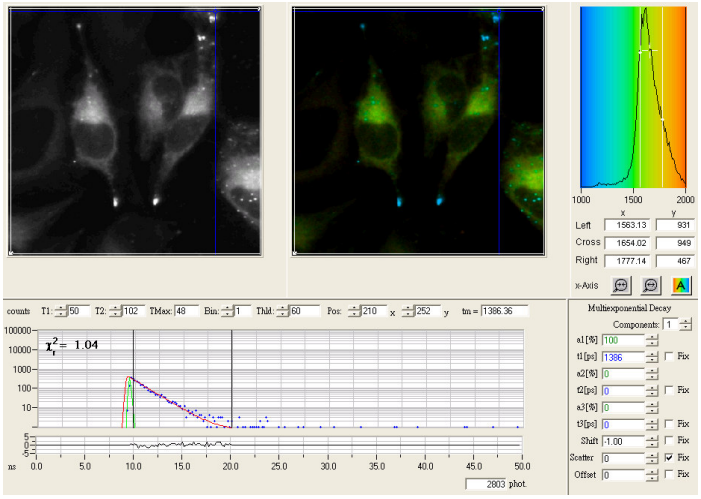

Figure 1. 8 FLIM of BODIPY-C_{12} in HeLa cells measured at 37℃. The excitation wavelength is 467 nm with a repetition rate of 20 MHz. The fluorescence spectrum is detected from 506 to 534 nm.

1.3.6 Förster Resonance Energy Transfer (FRET)

FRET is a phenomenon of energy transfer from one molecule to another molecule. It only occurs when the distance between two molecules is less than 10 nm, and the emission spectrum of a donor overlaps the absorption spectrum of an acceptor shown in Figure 1. 9. The donor, the excited molecule, transfers energy to the acceptor via non-radiative pathway. There are some important features, which is the efficiency of FRET and the Förster radius. The Förster radius is the distance when the probability of energy transfer reaches 50%. The FRET efficiency, E_{FRET}, is related to the separation of the pair of molecules r and the fluorescence lifetime of the donor, and it is given by[58]

$$E_{FRET} = \frac{1}{1+(\frac{r}{R_0})^6} = 1 - \frac{\tau_a}{\tau_i} \qquad (1.\ 16)$$

where R_0 is the Förster radius, and τ_i and τ_a is the fluorescence lifetime of the donor with and without a FRET acceptor. The effect is named after Theodor Förster who described and published it in 1946.[59]

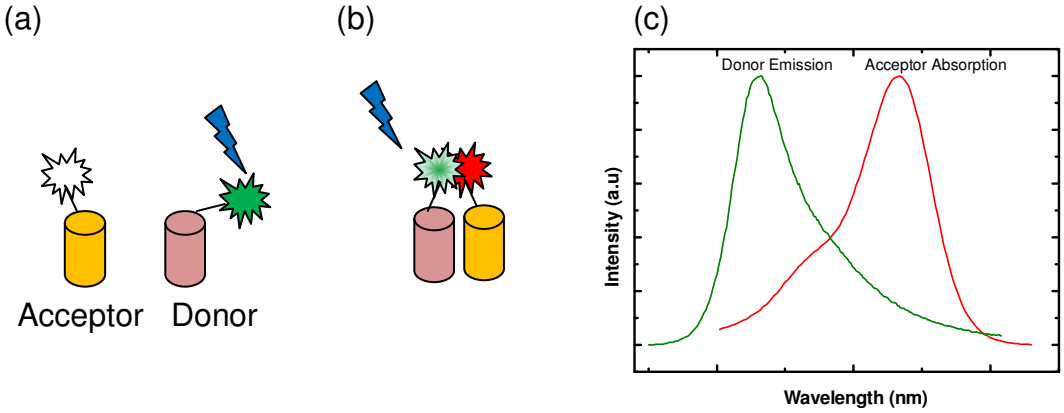

Figure 1. 9 A schematic of FRET. The excited donor emits green light, and (a) no FRET occurs. (b) When the distance between the donor and the acceptor is close, FRET happens. (c) An overlapping of donor emission spectrum and the acceptor absorption.

1.3.7 Fluorescence Anisotropy

1.3.7.1 Fluorescence anisotropy

The concept of fluorescence anisotropy measurement is to use polarized light to excite a fluorophore, and measure the difference between two orthogonal polarizing fluorescence decays. The emitted fluorescence is anisotropic, because rotational diffusion is the dominant mechanism of fluorescence depolarization,[60] that means a different intensity in the different polarization directions. The constituent of fluorescence intensity are parallel and perpendicular polarizations based on the electric vector of the incident beam, and its symbolizations are denoted as $I_{\parallel}$ and $I_{\perp}$, respectively. The fluorescence lifetime of a fluorophore is not influenced by the rotational diffusion of the fluorophore. The schematic diagram of fluorescence anisotropy measurements in L-format and collinear setups is shown in Figure 1.10.

Fluorescence anisotropy includes steady-state anisotropy and time-resolved anisotropy. From fluorescence anisotropy measurement, the size, the mobility rigidity, the shape of molecules and the environment can be measured.[1, 60] The range of the rotational correlation time that can be resolved in relation to the fluorescence lifetime, is generally between 0.1 and 10 times the fluorescence lifetime.[61, 62]

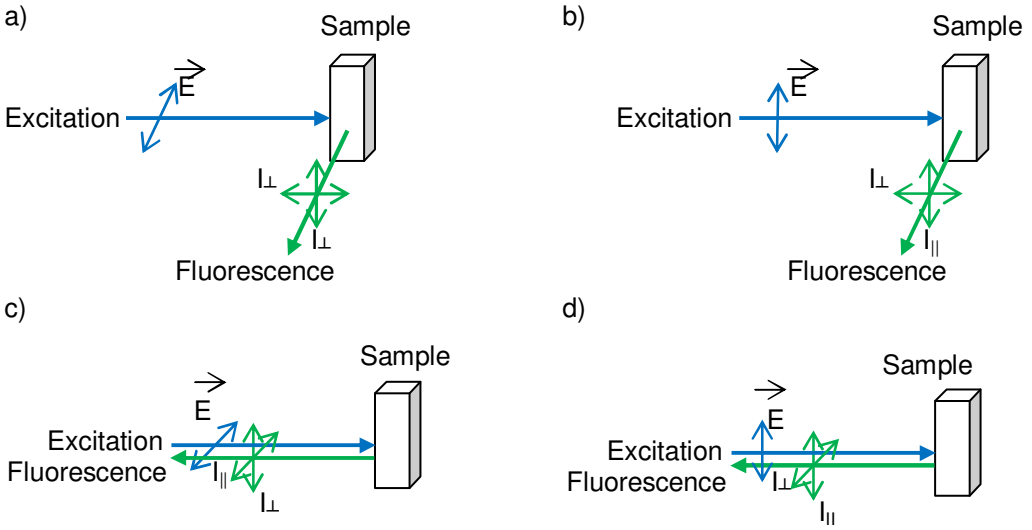

Figure 1.10 The sketch for different polarized excitations of fluorescence polarization measurement in (a, b) L-format setup and in (c, d) collinear setup.

In general, the definition of the fluorescence anisotropy r is given by

$$r = \frac{I_{\parallel} - GI_{\perp}}{I_{\parallel} + 2GI_{\perp}} \tag{1. 17}$$

such that time-resolved fluorescence anisotropy is given by

$$r(t) = \frac{I_{\parallel}(t) - GI_{\perp}(t)}{I_{\parallel}(t) + 2GI_{\perp}(t)} \tag{1. 18}$$

where r is anisotropy, G is the correction factor for different transmission and detection efficiencies in the parallel and the perpendicular polarizations. The denominator of the anisotropy expression is the total fluorescence intensity. A rotational mobility scheme of a molecule tagged with green fluorescent protein (GFP) is shown in Figure 1.11.[16] The red curves in the fluorescence decay and the time-resolved fluorescence anisotropy show the behaviour of the molecule

with a slow rotational diffusion. The molecule with fast rotational diffusion is shown in blue.

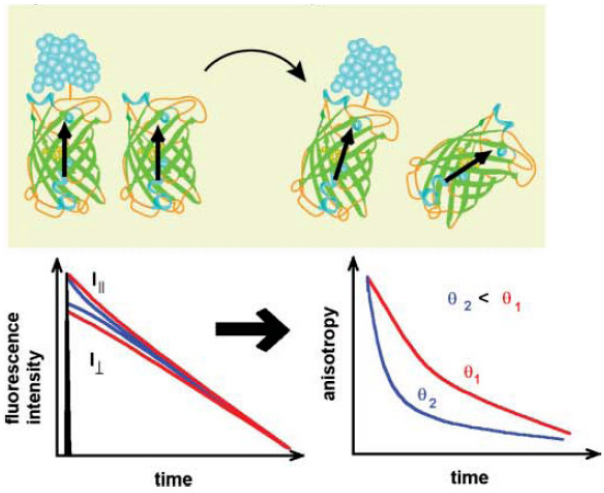

Figure 1.11 The schematic diagram of time-resolved fluorescence anisotropy of GFP-molecule.[16] The red and blue lines describe the behaviour of slow and fast rotation in fluorescence intensity and anisotropy decays.

The time-resolved fluorescence anisotropy decay for a freely rotating spherical molecule which is excited by a pulsed source can be presented as

$$r(t) = r_0 e^{-t/\theta} \tag{1. 19}$$

where r_0 is the initial anisotropy at time $t = 0$, and θ is the rotational correlation time. For a hindered rotating sphere, the time-resolved anisotropy is

$$r(t) = (r_0 - r_\infty) e^{-t/\theta} + r_\infty \tag{1. 20}$$

Here the limiting anisotropy r_∞ is defined as the anisotropy at $t = \infty$ with a nonzero value indicating the barrier to rotation.

1.3.7.2 Photoselection

The excitation probability for a fluorophore depends on the angle between the polarization of light and the absorption dipole moment of the molecule. The range of r_0 is associated with the probability. The absorption dipole moment of molecules is parallel to the polarization of light, so the excitation process occurs. There is no excitation happening if the absorption dipole of the molecule is perpendicular to the polarization of the light. The preference of molecules for excitation is called photoselection (see Figure 1.12), and its probability of excitation, p, is written as[63]

$$p_i = \cos^{2i}\alpha \cdot \sin\alpha \qquad (1.\ 21)$$

Here, the angle between the excitation light and the absorption dipole moment is α and the probability is associated with the excitation process via i-photon excitation.

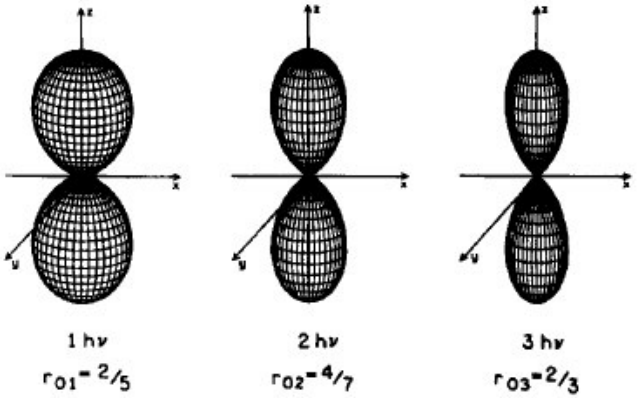

Figure 1.12 Orientation distribution of the excited state molecules for one-, two- and three-photon excitation. The values of the initial anisotropy are the maximum values.[63]

The steady-state fluorescence anisotropy for fluorophores with a parallel absorption and emission dipoles and random orientation in the ground state is given by[1]

$$r = (\frac{3}{2} < \cos^2 \alpha > -\frac{1}{2}) \tag{1. 22}$$

where α is the oriented dipole angle between the excited light and absorption dipole moment of a fluorophore. The value of r can be 1 for a single molecule according to eq. 1.22. In practice, the anisotropy for an ensemble of fluorophores in a homogeneous solution is less than 1.

The initial anisotropy of a fluorophore can be expressed by[1, 63-65]

$$r_0(\alpha, \beta) = (\frac{3}{2} < \cos^2 \alpha > -\frac{1}{2}) \cdot (\frac{3}{2} \cos^2 \beta - \frac{1}{2}) \tag{1. 23}$$

where

$$< \cos^2 \alpha >= \frac{\int_0^{\pi/2} \cos^2 \alpha \cdot p_i(\alpha) d\alpha}{\int_0^{\pi/2} p_i(\alpha) d\alpha} \tag{1. 24}$$

The angle between the absorption transition dipole moment and the emission transition moments is given β.

When the polarized fluorescence measurements are implemented via a confocal microscope, the depolarization occurs due to the NA of the objective lens.[66-71]

The initial anisotropy of a fluorescent molecule without the instrumental depolarization is deduced from eq. 1.23 and 1.24.[63, 64, 72]

$$r_0 = \frac{2i}{2i+3}\left(\frac{3\cos^2\beta}{2} - \frac{1}{2}\right) \qquad (1.25)$$

The maximum initial anisotropy for one-photon excitation is thus 0.4, and 0.57 for two-photon excitation process.

The Perrin equation is used to describe the depolarization due to the rotational diffusion of spherical molecules.[1]

$$\frac{r_0}{r} = 1 + \frac{\tau_f}{\theta} = 1 + 6\tau_f D_{rot} \qquad (1.26)$$

where D_{rot} is the rotational diffusion coefficient and r is the steady-state anisotropy. When $\theta >> \tau_f$ occurs, the value of the steady-state anisotropy is very close to that of the initial anisotropy. However, the value of r is close to zero at the case of $\theta << \tau_f$.

1.3.7.3 G-factor

The G factor for eq. 1.17 and eq. 1.18 is dependent on the geometry of the experiment. In the L-format setup, the G factor can be decided by the following

method. When the incident light is horizontally polarized, the emission fluorescence intensity in the horizontally and vertically polarized components is detected, which are both perpendicular to the excited light as shown in Figure 1.10. The intensity of the vertical polarization divided by the intensity of the horizontal direction results in the value of G. If the anisotropy measurement is obtained using a microscope, the geometry of the excited light and fluorescence is collinear. The G factor is represented as[72]

$$G = \sqrt{\frac{(I_{VV} - B)}{(I_{VH} - B)} \frac{(I_{HV} - B)}{(I_{HH} - B)}} \qquad (1.\ 27)$$

where B is the background intensity.

1.4 Probes

There are a few categories of probes developed for biological applications, and they are fluorescent proteins, quantum dots (QDs), fluorescent dyes, nanodiamonds and nanoparticles, e.g. gold nanoshells.[73]

1.4.1 Fluorescent Protein

For the discovery and development of green fluorescent protein (GFP), Osamu Shimomura, Martin Chalfie and Roger Y. Tsien were awarded the Nobel Prize in Chemistry in 2008. GFP consists of 238 amino acids residues (27 kDa), and its barrel structure protects from fluorescence quenching from solvent molecules as shown in Figure 1.13. GFP has been used in biological processes, such as a FRET probe for monitoring protein interaction[74, 75] and as a gene expression marker.[76] Moreover, fluorescent proteins have been used as sensors for refractive index[77, 78] and membrane potential.[79] GFP is less phototoxic than some small fluorescent dyes, such as fluorescein isothiocyanate (FITC) in live cells.[80] In addition, GFP can be expressed in

specific proteins or organisms via genetic engineering. GFP has been widely used in biological disciplines due to these advantages.[77, 79, 81-84]

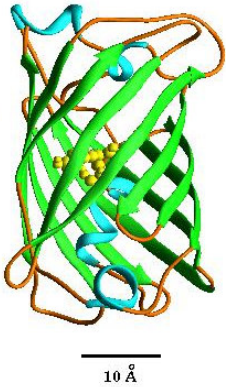

Figure 1.13 The structure of GFP. ß-sheet structure of protein is shown in green, α-helices in blue and the fluorophore is approximately in the centre of a cylinder.[85]

1.4.2 Quantum Dots

QDs are semiconductor materials with typical nanometres size.[86] The advantages are that the emission wavelength can be tuned by changing the size and shape of QDs. The photostability of QDs has been improved so they can be used in cell imaging.[87, 88] However, the drawbacks are blinking for single particle tracking experiments and toxicity to cells.[89] A modification on the surface of QDs may decrease the toxicity. The modification of QDs has also been used in bioprobes, biosensors and assays via FRET technique.[86]

1.4.3 Fluorescent Dye

Generally, the structure of fluorescent dyes consists of aromatic rings. More fluorescent molecules have been developed by modifying the molecular structure causing different absorption and emission spectra. The dyes can be excited from UV to infrared red with emission in this wavelength region, covering more than visible wavelength. The size of fluorescent dyes is small, for example fluorescein has a radius of 0.5 nm.[90, 91] The fluorescent properties of

typical dyes are summarized in Figure 1.14.[92] The brightness of dyes depends on the ability of absorption and emission, defined as the multiplication of the extinction coefficient and fluorescence quantum yield. Dyes can be excited in the region of the wavelength shown in the coloured-scale x-axis of Figure 1.14. The molecular structure with colour denotes the corresponding emission wavelength.

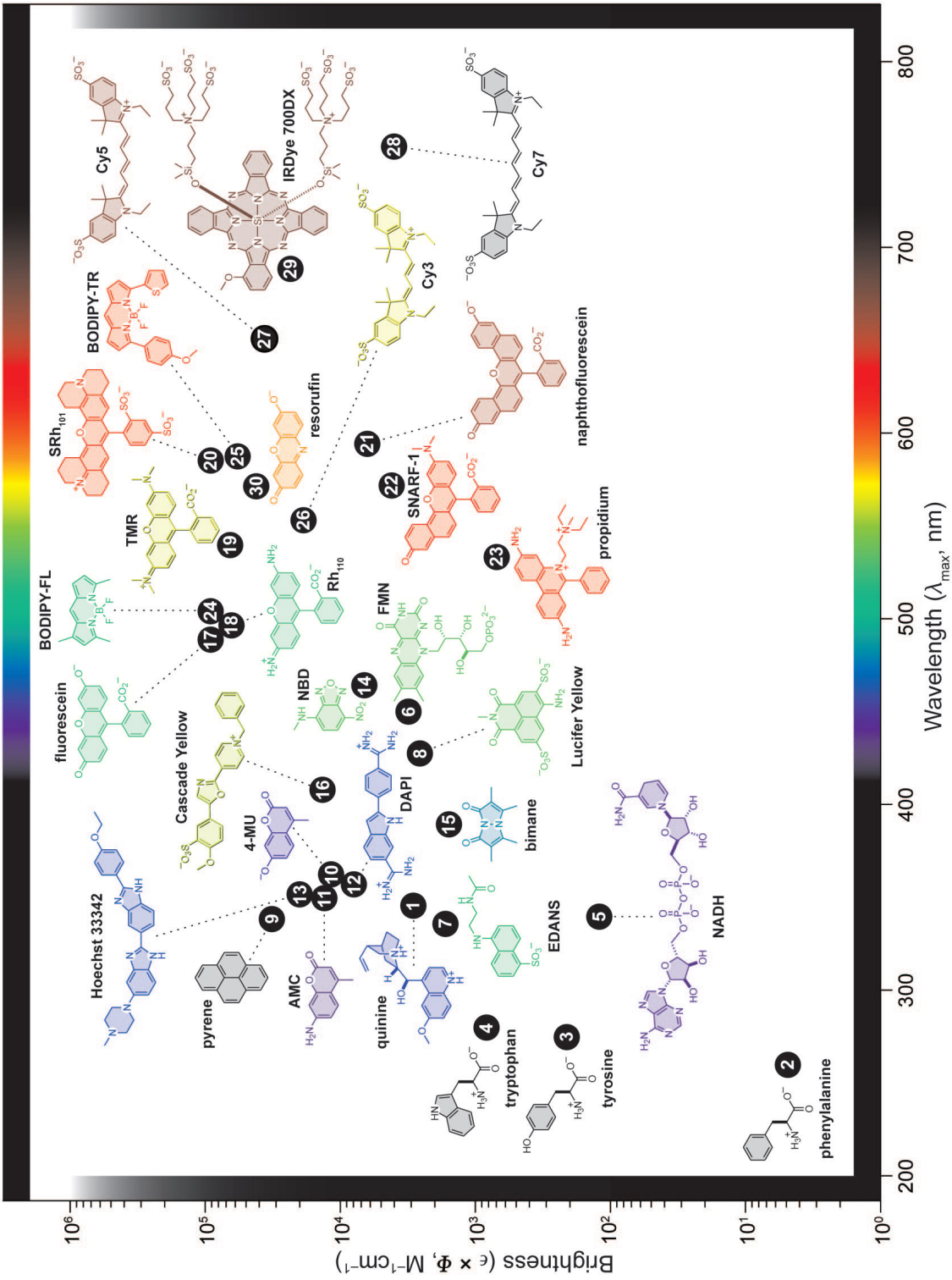

Figure 1.14 The brightness of major fluorescent dyes versus the main absorption wavelength, and the corresponding emission wavelength illustrated in the colour of the molecular structure.[92]

1.4.3.1 Fluorescent Molecular Rotors

A Fluorescent molecular rotor is a type of fluorescent dyes. It is very unique in that — its quantum yield and fluorescence lifetime is a function of viscosity. This is due to the ability of the fluorescent molecular rotor to twist in the excited state. The nonradiative rate of fluorescence varies with the intramolecular twisting angle resulting in different quantum yields.[93, 94] Fluorescent molecular rotors have been used to monitor viscosity of environments, e.g. in polymers or living cells. Moreover, fluorescent molecular rotors have been modified to create photolockable ratiometric viscosity sensitivity rotors.[95] The viscosity-sensitive behaviour of the fluorescent molecular rotors is activated and deactivated by illuminated UV light to change the conformation of the molecules. This fluorophore may be a candidate that can be applied in high-resolution microscopy.

A molecular rotor contains a part of it rotating against another part of the molecule.[96] A fluorescent molecular rotor is made up three subunits, an electron donor, an electron acceptor and a single bond connected to two subunits.[97] The typical representations are shown in Figure 1.15, e.g. 4-(Dicyanovinyl)Julolidine (DCVJ), 4,4-dimethylaminobenzonitrile (DMABN), p-(dimethylamino) stilbazolium (p-DASPMI) and Thioflavin T, a boron dipyrromethene (BODIPY) derivative.[97-101] In Figure 1.15, the blue region has e^- rich and the electron acceptor is shown in red. The rotation occurs in the position of arrows.

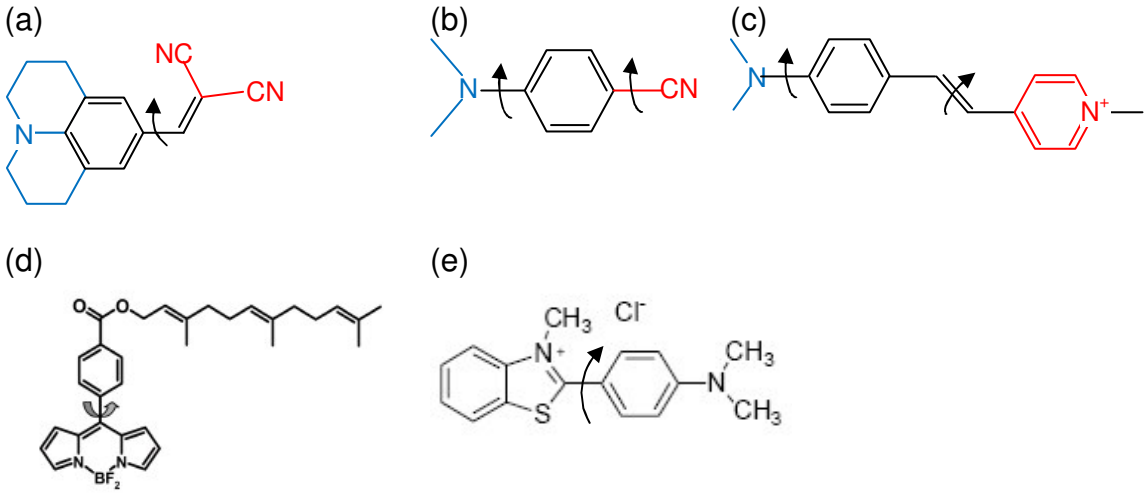

Figure 1.15 The molecular structure for typical fluorescent molecular rotors, for example, (a) DCVJ, (b) DMABN, (c) p-DASPMI, (d) BODIPY derivative,[100] and an adapted image of (e) Thioflavin T.[102] The electron donor is shown in blue, the acceptor in red and the arrow denotes the twisting position.

It has been reported that solvent viscosity is an important factor to affect the quantum yield and lifetime of a fluorescent molecular rotor.[94, 103] Viscosity is the resistance in the flow of a fluid. It can be described using two ways. The first description is called absolute viscosity or dynamic viscosity, and the unit is Pascal second (Pa·s) or centipoises (cP). It is determined as the ratio of the shearing stress to the velocity gradient of a fluid, and the formula is

$$\eta = \frac{F \cdot y}{\Delta v \cdot A} \qquad (1.28)$$

where η represents viscosity, F is shearing force, A is the area of region under the shearing force, Δv represents the variation of velocity of fluid and y is the distance between the fluid layers.

The second definition of viscosity is named kinematic viscosity, η_{kin}, and its common unit is mm^2/s or centistokes (cSt). It is defined as the ratio of the dynamic viscosity to the density of fluid as shown

$$\eta_{kin} = \frac{\eta}{d} \qquad (1.\ 29)$$

where d is the density of a fluid.

Viscosity can also be classified into microviscosity and macroviscosity which depends on the scale between a probe and its environment. Microviscosity is the viscosity that is measured in the interior of the bulk solvent[104] at the micrometer length scale. On the other hand, the bulk viscosity is the measurement of a large-scale probe.

The ability to twist and the extent of twisting for fluorescent molecular rotors are affected by the ambient media, e.g. the charged dipole of a fluorescent molecule is reoriented by the solvent molecules, and the steric hindrance influences the nonradiative process. The mechanism promotes the fluorescent molecular rotors as viscosity probes.

1.4.3.2 Polarity Sensors

The fluorescent molecules with intramolecular twisting motion, can sense not only a variation of viscosity, but also the polarity of environment. The typical molecules are cyanines,[105] rhodamine 800,[106] etc, all of which display fluorescence lifetime increases after binding to protein. The lifetime and emission spectral shift are due to the variation of dipole moment of dyes. This fluorescence behaviour promotes the development of lifetime polarity probes.[107] Polarity is a characteristic of a molecule, and it is described as the electronic dipole moment due to the distribution of electronic charge.

A brief comparison of fluorescent materials is shown in Table 1. 2. Each fluorescent molecule has the advantage and disadvantage depending on the

usage. For example, blinking effect reduces the probability of FRET processes,[108] however, PALM or STORM use blinking phenomena to form a high-resolution image.

Table 1. 2 Summary of general fluorescent probes.

	Dyes	Quantum dots	Fluorescent proteins	Fluorescent molecular rotors
Size	small	big	big	small
Blinking	×	✓	×	×
Fluorescence stability		×	✓	

1.5 Viscosity of Cell Environments

The viscosity of a cell is an interesting and important property. Metabolism, protein-protein interaction and dynamic processes in biological systems are influenced by viscosity. The increasing viscosity during photo-induced cell death has been reported.[109] The membrane viscosity is associated with many diseases, e.g. Alzheimer's disease.[110-113] The viscosity of blood vessels changes the behaviour of red blood cells (RBCs). The abnormal aggregation of RBCs is associated with many diseases, e.g. Acquired Immune Deficiency Syndrome (AIDS), myeloma, diabetes mellitus and deep venous thrombosis.[114]

1.5.1 Ways to Measure Viscosity

There are many methods to measure the viscosity of the environment, the mechanical ways and fluorescence techniques. The mechanical method includes rheometry to measure the morphology change by applying a physical force. Optical tweezers have been used to yield the apparent viscosity of a cell membrane by measuring the recovery after deformation.[115, 116] However it is a whole cellular reaction. The obtained viscosity is an average behaviour, and the intracellular viscosity distribution could not be revealed. In addition, the displacement of micrometer-size beads confined by optical tweezers is used to

monitor the Brownian motion of a particle, and to calculate the viscosity of a medium.[117] Fluorescence-based methods have been used to measure viscosity, such as fluorescence anisotropy, FRAP, FCS and particle tracking. The viscosity can be converted from the translational diffusion coefficient of fluorophore via FRAP measurement. The viscosity obtained by this method provides an average for the bleaching area environment. The size of bleaching spot is the limitation of spatial resolution in FRAP measurement. FCS and particle tracking also show the translational diffusion of molecules in a local environment. The combination of fluorescence cross-correlation spectroscopy (FCCS) and imaging total internal reflection is a promising technique to measure the dynamics over an area, e.g. cell membranes.[118] In addition, the rotational correlation time of a fluorescent molecule can be measured from the fluorescence anisotropy measurement and yield the viscosity over an area within the optical resolution limit.[90]

Since it was found that the quantum yield of fluorescent molecular rotors varies with viscosity, a viscosity sensor has been developed based on this concept. There are two strategies to measure the viscosity of the cell environments using fluorescent molecular rotors, and the starting points are emission intensity and the fluorescence lifetime.

In general, the fluorescence intensity is proportional to the concentration of fluorophores. The emission intensity of a fluorescent molecular rotor is related to the viscosity of the environment. Hence, it is difficult to discriminate between the concentration effect and viscosity effect when the fluorescent molecular rotors are applied in unknown systems. Therefore, the ratiometric principle has been developed to correct the concentration effect,[119] but this could not deal with heterogeneity, i.e. multi-exponential decays. Also, the calibration has to be done on the same camera due to a variation of detection sensitivities at different wavelengths. It may be problematic to measure the viscosity of cells in the following case. If one of emission bands is in the range of cells

autofluorescence, then the ratiometric method is not a good method. It is because the autofluorescence signal influences the intensity ratio of two emission peaks. Recently, Peng and his co-workers reported a fluorescent molecular rotor to measure intracellular viscosity base on ratiometric and FLIM concepts. The probe is excited via two-photon process in order to avoid an interference emission intensity of dye by autofluorescence of cells.[120]

1.5.2 Viscosity of Cytoplasm

The viscosity of cell environments has been studied. The viscosity of cytoplasm is similar to that of free water, and varies with the different cells.[121-124] The microscopic or macroscopic viscosity can be measured depending on the size of probes in the environment. It has been suggested that the viscosity measured by diffusion methods is influenced by the concentration and the size of the probe.[124] The microscopic viscosity of cytoplasm is approximately 2 cP for HeLa and 0.88 cP for Embryonic Swiss Mouse Fibroblast (3T3) cells using small sized probes.[124] The macroscopic viscosities of cytoplasm for HeLa and 3T3 cells are 44 and 24 cP, respectively.[124]

1.5.3 Viscosity of Synthetic Membrane

Cell membranes consist of lipid, proteins and membrane rafts with different mobilities. To obtain the viscosity of cell membranes, the artificial liposome has been employed to mimic the viscosity using fluorescent molecular rotors and compare the results from FRAP measurement.[125] The viscosity of dipalmitoylphosphatidylcholine (DPPC) liposomes was found to be 94 cP at 25℃ by Kung and Reed.[126] However a range of microviscosity has been reported between 30 and 1000 cP.[126] Nipper and his co-workers reported a study of the liposome model and its response to propanol using the ratiometric molecular rotor.[127] The membrane viscosity of dilauroylphosphatidylcholine (DLPC) liposomes is 61 cP, and decreases when propanol inserts into the membrane. It results in the separation of the lipids and increasing a local free

volume. The increase of free volume around the fluorescent molecular rotors would lead a lower viscosity.

It has been demonstrated that the viscosity of intracellular vesicles is 160 cP for Human ovary adenocarcinoma (SK-OV-3) using BODIPY-C_{12} via FLIM, 60 cP via time-resolved fluorescence anisotropy measurement.[100, 128] It seems that the punctate viscosities for SK-OV-3 and Chinese hamster ovary (CHO) cells are in the same order of magnitude.[109, 129] A brief comparison of intracellular viscosity and viscosity of related cell systems are given in Table 1. 3.

Table 1. 3 An overview of cell viscosity and synthesised membrane viscosity.

	Viscosity	Temperature (℃)	Methodology	Ref.
Cytoplasm	10-13 cP for Madin-Darby canine kidney Epithelial cells (MDCK) and 3T3	23	Time-resolved and Steady-state fluorescence anisotropy	130
	1.2-1.4 cP for 3T3	24	Phase modulation microfluorimetry	121
	2.1-2.5 cP for sea urchin eggs	22	Frequency-domain fluorometry	131
	0.94 cP for Normal African Green Monkey Fibroblast cells (CV1) 0.96 cP for Female Rat Kangaroo Kidney Epithelial cells (PtK1)	37	Fluorescence Ratiometric method	122
	1.0-1.5 cP for CHO, 3T3, Human mononuclear cells and Sarcoma-180 tumour cells	-	Time-resolved fluorescence anisotropy	123
	3.2 cP for CHO	Room temperature	FRAP	132

	6 cP for B cells	20	Time-resolved fluorescence anisotropy	[90]
	7-18 cP for DB1X rat embryonic thoracic aorta smooth muscle cells	37	Fluorescence Ratiometric method	[133]
	Microscopic viscosity: 0.9 cP for HeLa 2 cP for 3T3 Macroscopic viscosity: 44 cP for HeLa 24 cP for 3T3	37	FCS	[124]
Synthetic Membrane	94 cP for DPPC vesicles 6.9 cP for SDS micelles	25	lifetime	[126]
	120-70 cP for DPPC vesicles	10-60	lifetime	[126]
	2.2 cP for soybean phospholipid liposomes	-	Time-resolved fluorescence anisotropy	[123]
	61 cP for DLPC liposomes	30	Fluorescence Intensity	[127]
Endocytotic vesicles	~160 cP for SK-OV-3	25	FLIM	[100, 128]
	~60 cP for SK-OV-3	25	Time-resolved fluorescence anisotropy	[100, 128]
	50 cP for CHO	22	Fluorescence ratiometric method	[109]
	30-70 cP for HeLa	37	Steady-state anisotropy	[129]

1.6 Thesis Outline

In this thesis, fluorescence techniques have been employed to study the viscosity of the intracellular environment. The overview of fluorescence, the fluorescent probe and the study of intracellular viscosity have been described. Next, a description of instruments and the theories are described in Chapter 2. In the following Chapters 3 and 4, the viscosities of environments are measured using a meso-substituted BODIPY-C_{12} as a fluorescent molecular rotor via the

fluorescence lifetime and the rotational correlation time. The locations of BODIPY-C_{12} in cells were also identified by counterstaining experiments. It may provide useful information for studying the organelle of interest. A further study of BODIPY-C_{12} shows a dip-and–rise curve in the time-resolved fluorescence anisotropy decay. The dipole moment of fluorescent molecules can be obtained from the photophysical characteristics. In Chapter 5, we use an advanced model to describe the transition dipole moment of fluorophores. It provides another way to explore the transition dipole moment. Finally, in Chapter 6 conclusions were drawn based on the results and followed by discussion of further studies.

Chapter 2

Instrumentation and Theoretical Framework

2.1 Introduction

The photophysical properties of fluorophores can be obtained from spectroscopic measurements. Absorption and emission spectrometers are used to carry out the steady-state spectroscopy of fluorophores. Time-resolved fluorescence decays are measured via scanning confocal microscopy coupled with time-correlated single photon counting (TCSPC). The fluorescence lifetime can reveal the environment around a probe. The rotational correlation time can be measured via time-resolved fluorescence anisotropy measurements. The brief descriptions of related instrumentation and the theories are presented in this chapter.

2.2 Instrumentation

UV/Vis absorption (Hitachi, U-4100) and luminescence (Perkin-Elmer, LS-50B) spectrometers are used to determine the quantum yield of a fluorophore. A refractometer (ABBE 60 Series, Bellingham + Stanley Limited) is used to measure the refractive index of solutions. The time-resolved fluorescence measurements are carried out by the inverted confocal scanning microscope (Leica, TCS SP2) combined with a TCSPC-module (Becker & Hickl, SPC-830), two types of detectors (Becker & Hickl, PMC-100 photomultipliers or HPM-100-40 hybrid detectors) and a pulsed diode laser (Hamamatsu, PLP-10 470 nm).

2.2.1 Absorption and Emission Spectroscopy

The sample solution is placed in a cuvette. The absorption of light by molecules is described by the Beer-Lambert law.

$$OD = \log_{10}(\frac{I_0}{I}) = \varepsilon c l \qquad (2.\ 1)$$

where OD is optical density, I_0 and I mean the light intensity of before and after passing through the sample with the concentration of c, ε is the extinction coefficient of the solute in the solvent which is a measure of the probability that a photon is absorbed, and l is the path length of the light through the sample. The information of the excited state of a fluorophore adjacent to the solvent molecules can be studied by absorption spectroscopy.

The emission spectrum of a fluorophore is associated with the solvent interaction and the ground state. A fluorophore reaches an equilibrium state in the excited state prior to transit to the ground state. According to Kasha's rule, the emission spectrum is typically independent of the excitation wavelength. The emission spectrum can reveal how many excited states a fluorophore has.

2.2.2 Confocal Microscope

In our lab, we use a Leica TCS SP2 confocal scanning microscope, and the schematic diagram is shown in Figure 2. 1. The continuous wave Argon Ion laser is used to excite samples and the excitation wavelengths are 458 nm, 476 nm, 488 nm and 514 nm. It also has two external laser inputs, the IR or UV ports, and an external port for detection which allows us to do the time-resolved fluorescence experiments by detecting the fluorescence with time-resolved detectors. Before the laser beam is focused on a sample through an objective lens, it is reflected by a dichroic mirror and scanning mirrors to perform a plane

scan of a sample. The optical image of samples is recorded using a detector under the sample. The fluorescence signal passes through the same objective lens, optical elements, a monochromator separating the wavelength of signal, a slit and is detected via an analogue detector (internal photomultiplier). In our setup, a pulsed diode laser is shone through the UV port, and the light from a Ti:Sapphire laser is shone through the IR port into the scanhead of the microscope. The external detectors for time-resolved measurements are PMT, single-photon avalanche diode (SPAD) or hybrid PMT detectors. Brief descriptions of light source and detectors are presented in the subsequent sections.

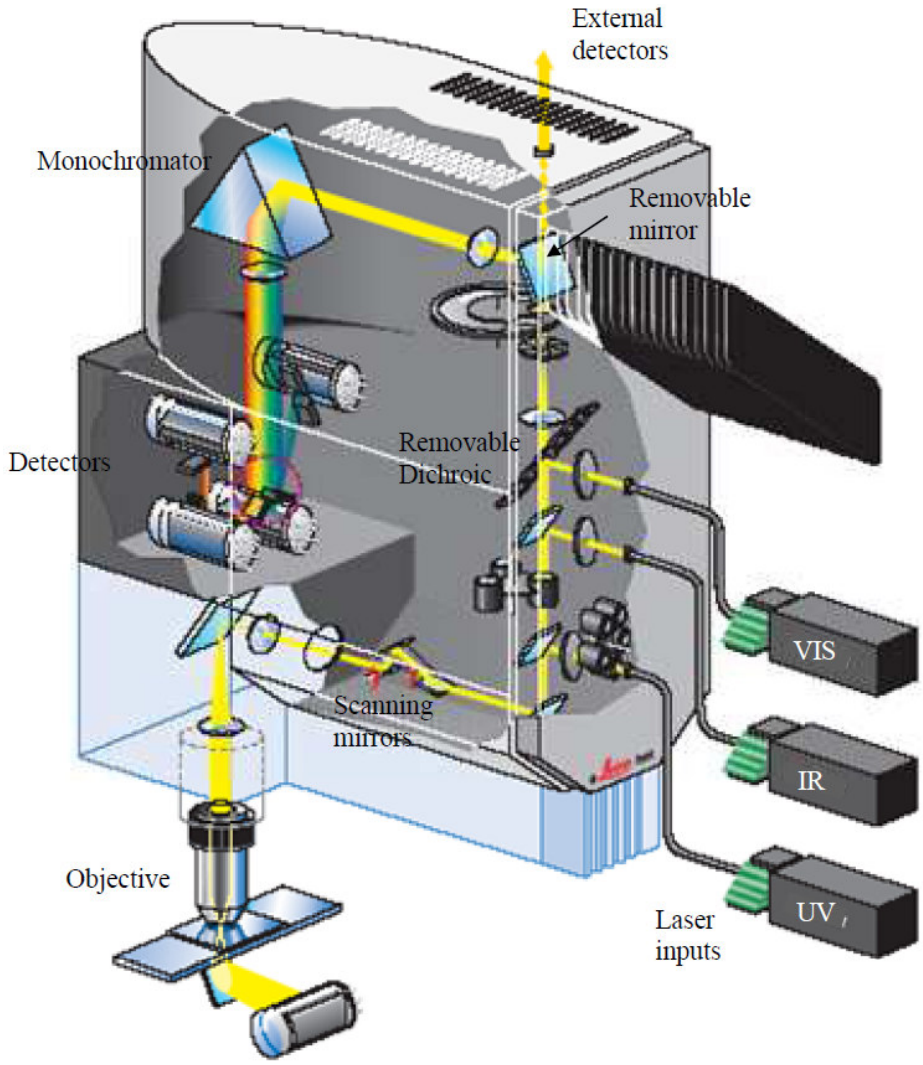

Figure 2. 1 Schematic of a Leica TCS SP2 confocal scanning microscope.[134]

2.2.3 TCSPC

2.2.3.1 TCSPC principle

A fluorescence lifetime measurement can be measured in the time domain. In this work, the fluorescence lifetime measurements are carried out in the time domain. There are two ways to collect the fluorescence signal in the time domain, time gating and TCSPC, and a pulsed light source is used in both methods. Here we use the TCSPC technique to conduct the fluorescence lifetime measurements. This measurement is to detect the arrival time of a single photon arriving on the detector within the time duration of the time to amplitude converter (TAC) window, and then a plot of the number of photons versus the arrival time can be used to determine the fluorescence lifetime of a fluorophore shown as in Figure 2. 2. However, the limitation of the fluorescence lifetimes that can be measured is dependent on the instrument response function (IRF), the repetition rate of a pulsed laser and TAC window. A detail of IRF and TAC is described subsequently.

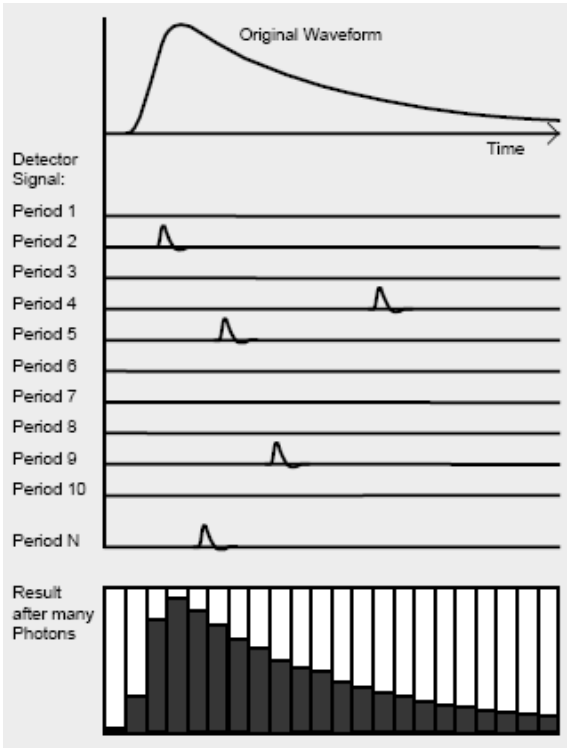

Figure 2. 2 Principle of the TCSPC technique.[135]

The probability of photon arriving on a detector in a fixed interval time follows Poisson distribution, is given by[136, 137]

$$P_n = \frac{\mu^n}{n!} e^{-\mu} \tag{2. 2}$$

where P_n is the probability of detecting n photons per unit time, and μ is the average number of the emitted photons per unit time. The photons hit the photocathode, and then produce m photoelectrons. The probability, P_m, of m photoelectrons can be successful excited can be described by binomial distribution, is given by

$$P_m = \binom{n}{m} q^m (1-q)^{n-m} \tag{2. 3}$$

where q is the quantum efficiency of the photocathode. Hence, the probability of n photons generating m photoelectrons can be reduced to

$$\begin{aligned} P_{eject} &= \sum_{n=m}^{\infty} P_n P_m = \frac{e^{-\mu} q^m}{m!} \sum_{n=m}^{\infty} \frac{\mu^n}{(n-m)!} (1-q)^{n-m} \\ &= \frac{e^{-\mu} q^m}{m!} \sum_{j=o}^{\infty} \frac{\mu^{m+j}}{j!} (1-q)^j = \frac{(q\mu)^m e^{-q\mu}}{m!} \end{aligned} \tag{2. 4}$$

This is also a Poisson distribution, and for small $q\mu$, the detection probability is proportional to the intensity $q\mu$.

2.2.3.3 TCSPC Instrumentation

The schematic of classic TCSPC detection is illustrated in Figure 2. 3.[138] A single photon arrives on the detector, and it produces a pulse. Because the amplitude gained in the detector is random which means the timing of the pulses can be biased, the function of a Constant Fraction Discriminator (CFD) is to threshold the photon signal and eliminate pulse height dependent timing. The other CFD is to obtain the timing reference pulse from the laser. Then both pulses signals pass to the TAC. It measures the time of the photon arriving at the detector. The pulse signal form the excitation source is to switch on a current to charge a capacitor, and the pulse from the detector arriving at TAC to switch off the current. The charging time results in the proportional charge of a capacitor. The charge of a capacitor converts to the voltage and finally passes through Biased Amplifier (AMP) to amplify the signal. The signal reaches Analog to Digital Converter (ADC) converting to digital time information of the photons arriving.

The maximum signal can be produced via TCSPC is related to the dead time of electronics and pile-up of signals.[139] It is briefly described below.

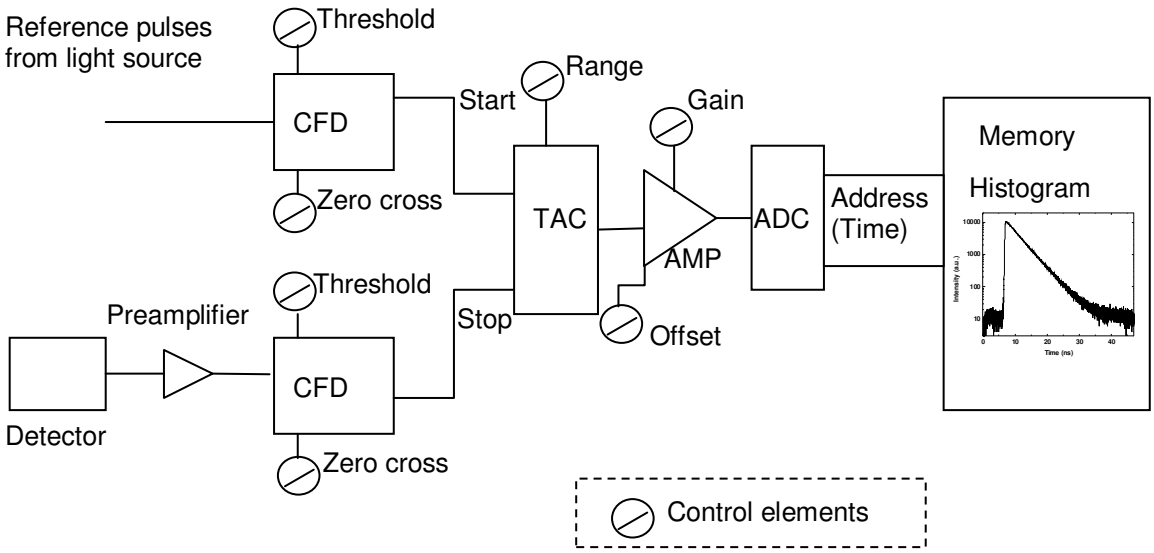

Figure 2. 3 The configuration of TCSPC device.

2.2.3.3 Dead Time

Dead time is the time for a detector and electronics to process a photon event, and no further photon can be recorded during the time.[138] It decreases the probability that a photon can be detected via TCSPC, and therefore it takes a longer acquisition time to collect enough counts.

2.2.3.4 Pile-up

TCSPC is based on a detection of one photon per excitation cycle. More than one photon arriving in a detector in a single period, only one photon is detected and others cannot be recorded. It causes a distortion of the fluorescence decay. The solution to avoid the pile-up effect is decreasing the detection rate, and a suggested count rate is less than 1% of the pulse repetition rate so that eq. 2.4 is linear.[135] Another method to reduce the pile-up effect is to detect photons at the same time via a multichannel detector.[135]

2.2.3.5 Lifetime

The fluorescence decay recorded using a detector is not the actual fluorescence decay of a fluorophore, because the IRF is influencing the actual fluorescence decay. A detailed description of an IRF will be described in the next section. A convolution of the actual fluorescence decay F, and the IRF I, results in the experimental fluorescence decay E.[140]

$$E = F \otimes I \tag{2. 5}$$

The actual fluorescence decay is described by a monoexponential or multiexponential decay function. SPCImage (Version 3.2.3.0, Becker & Hickl) and TRI2 (Version 2.3.9.1, Gray Institute for Radiation Oncology & Biology)[141] software, we use them to determine the fluorescence lifetime of a fluorophore by comparison of the experimental fluorescence decay and a convolution of an

exponential function and IRF. The lifetime is decided from the exponential function with the best fit. In SPCImage software, the IRF can be found either from the rising edge of any fluorescence decay or by measuring an extremely fast lifetime sample.

The goodness of fit is decided by the value of χ_r^2, which is given by

$$\chi_r^2 = \frac{1}{N-p}[\sum_{i=1}^{N}\frac{(d_i - f_i)^2}{d_i}] \quad (2.\ 6)$$

where N is the number of the data points, p is the number of the variable fit parameters, and d_i and f_i are the data and the fit value at the i-th time point. The best fit of data is that the value of $\chi_r^2 = 1$, and the residuals are randomly distributed around zero.

To get accurate fluorescence lifetimes, some issues need to be addressed. The time-resolved measurements may be distorted by the wavelength sensitivity of the detector. It is better to use the fast fluorescence decay sample which has the same range of emission wavelength as the dye we used in this thesis.[142] The emission spectrum of DCVJ (Invitrogen) is shown in Figure 2. 4. The fluorescence lifetime of DCVJ in methanol is less than 10 ps.[129, 143] Due to the extremely short lifetime, shorter than the IRF, the recorded fluorescence signal is the IRF. For this reason, DCVJ dissolved in methanol was used to measure the IRF. The FWHM was 227 ps for the hybrid PMT detector and 278 ps for the PMT detector using the diode laser.

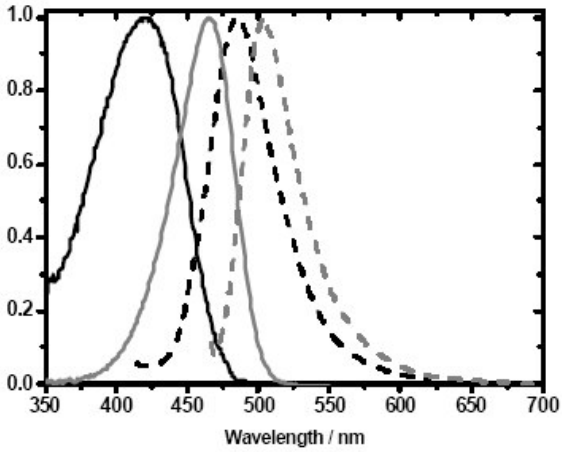

Figure 2. 4 Normalized absorption (grey solid line) and emission (grey dashed line) spectra of DCVJ (the concentration is ~ 8 μM). The black solid line and black dashed line are absorption and emission spectra of 9-(2-carboxy-2-cyanovinyl)julolidine (CCVJ).[129]

2.2.4 Detectors for Time-Resolved Fluorescence Measurements

The detectors for performing the single photon counting measurements are PMT (Becker & Hickl PMC-100, based on a HAMAMATSU H5773P-01 photomultiplier), SPAD (Id Quantique ID-100), and hybrid PMT detectors (Becker & Hickl HPM-100-40, based on a HAMAMATSU R10467U-40 photomultiplier). Each detector has disadvantages and advantages.

The limitation of fluorescence lifetime can be discriminated down to 10% of the full width at half maximum (FWHM) of the IRF.[136, 138] The IRF for PMT detectors is influenced by the transit-time spread of the detector. In addition, the ion molecules in the vacuum chamber of a PMT detector induce the afterpulsing phenomenon. Therefore, the signal induced noise exists in fluorescence decay via TCSPC technique. A SPAD detector has a narrow FWHM of the IRF and low noise background. The time resolution of some SPAD detectors and the detection efficiency are related on the focus position of fluorescence signals on the active area of a SPAD detector.[144] Due to the small active area of SPAD detector, it is difficult to align a SPAD detector compared to a PMT detector. A more recent detector, a hybrid PMT detector, has the advantage of PMT and

SPAD detectors.[145] The width of the IRF in SPAD and hybrid PMT detectors is given by charge carrier diffusion.

Here, a comparison of the IRF using a diode laser for 3 detectors is shown in Figure 2. 5. A pulsed laser with a duration time of 90 ps was used to excite DCVJ in methanol. In order to compare the FWHM of the IRF, the IRF for 3 detectors was normalized. The FWHM of the IRF for the PMT detector was 248 ps, the hybrid PMT detector was 218 ps, and the SPAD detector was 154 ps. The broadest FWHM is found for the PMT detector, and moreover it has an extra pulse after the main peak. It was found that the hybrid PMT and SPAD detectors have no afterpulsing. However, the SPAD detector has a charge carrier diffusion tail.

The FWHM of the IRF, Δt_{instr}, is dependent on a pulse width of a laser, Δt_{op}, and the electronic process time on a detector.[140]

$$\Delta t_{instr}{}^2 = \Delta t_{op}{}^2 + \Delta t_{jitter}{}^2 + \Delta t_{trans}{}^2 \qquad (2.\ 7)$$

where Δt_{jitter} is the electronic jitter, and Δt_{trans} is the signal transit time of detector.

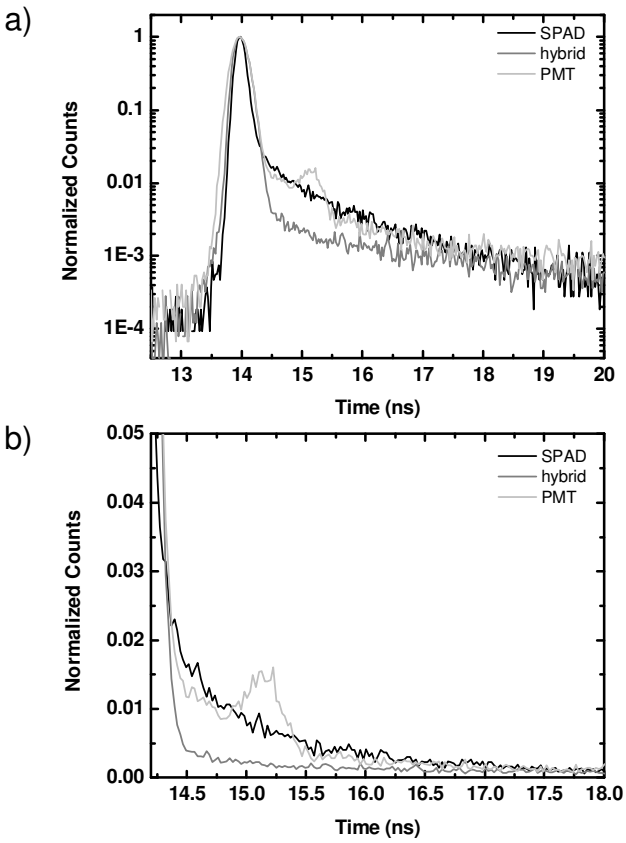

Figure 2. 5 The IRF of the hybrid (grey), the SPAD (black) and the PMT (light grey) detectors. (a) The IRF profile and (b) the tail of the IRF in the time range of 14.2-18 ns. A band-pass filter at 514 nm was placed before the detector to allow fluorescence of DCVJ in methanol excited using a laser at the wavelength of 467 nm with a repetition rate of 10 MHz and a pulse width of 90 ps.

We illustrate a brief comparison of fluorescence decay of Rh123 in methanol/glycerol mixture with 25% V/V glycerol detected using the PMT and the hybrid PMT detector that are used in this research simultaneously, shown in Figure 2. 6. The position of a non-polarizing beamsplitter cube (Edmund, NT47-121) was aligned until the same fluorescence decays recorded via two PMT detectors occur simultaneously. In other words, the fluorescence signal is split into two beams with equal amount of photons. The next step is to employ a hybrid PMT detector instead of a PMT detector, and measure the fluorescence of Rh123.

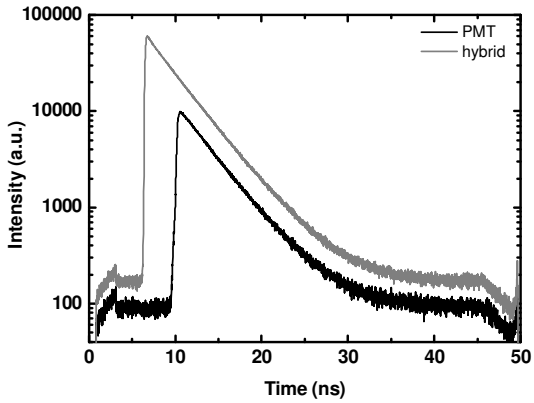

Figure 2. 6 The fluorescence decay of Rh123 measured simultaneously by a hybrid PMT (grey) and a PMT (black) detector. The excitation wavelength is 467 nm with a repetition rate of 10 MHz, and the emission is 506-594 nm.

The quantum efficiency, QE , of a detector is the ratio of the numbers photons emitted from the photocathode versus the number of photons hit the photocathode, and it can be calculated using this equation.[146]

$$QE = \frac{1240 \cdot S}{\lambda} \tag{2. 8}$$

where S is the cathode radiant sensitivity at the wavelength of λ, and the corresponding units are amperes per watt (A/W) and nm, respectively. The spectral cathode radiant sensitivity of the PMT detector is illustrated in Figure 2. 7.

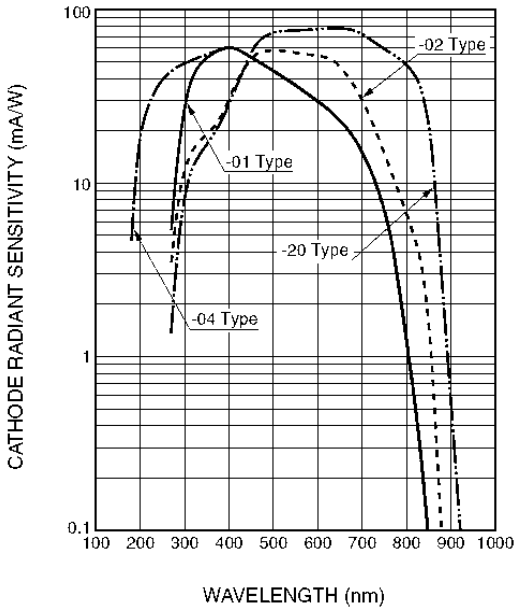

Figure 2. 7 The cathode radiant sensitivity of PMT detector (H5773, Hamamatsu), and the characteristic of our detector is the 01-type curve.[147]

From the decays (Figure 2. 6), there are more photons distributed in the fluorescence decay using the hybrid PMT detector rather than the PMT detector. By integrating the intensity below the decay curves (see Figure 2. 6), it was found that the total number of photons for the hybrid PMT detector is 5.29 times larger than that for the PMT detector. A quantum efficiency of 48.6-54% for the hybrid PMT detector at 500 nm has been measured by the manufacturer.[148] The quantum efficiency of the PMT detector is calculated using the sensitivity of the cathode of 01-type in Figure 2. 7 of ~ 41mA/W at 500 nm is fed into eq. 2.8. It was found to be approximately 10% at 500 nm.[147] The quantum efficiency calculated from the results in Figure 2. 6 is 54%/5.29=10.2%. Therefore, the quantum efficiency measured is very close to that reported from the supplier. Hence, the hybrid PMT detector is better than the PMT detector for TCSPC measurements. Also, it has been reported that the afterpulsing of detector produces signal induced noise, and therefore it results in a decrease of the signal to noise ratio.[145]

2.3 Theory

In order to interpret the fluorescent properties of a fluorophore, an overview of theories is presented.

2.3.1 Förster-Hoffmann

The quantum yield of a fluorescent molecular rotor following the Förster-Hoffmann equation is[103]

$$\Phi = z\eta^{\alpha} \tag{2. 9}$$

such that the fluorescence lifetime is given by [149, 150]

$$\tau_f = \frac{z\eta^{\alpha}}{k_r} \tag{2. 10}$$

where z and α are constants, and η is the viscosity of the environment. The value of α is 2/3 for crystal violet in methanol/glycerol solutions.[103] The same fluorophore in different solvents yields different α values, 0.5-1.1 for DCVJ — thus α is solvent dependent for the same fluorophore.[126, 129, 151-154]

2.3.2 Strickler-Berg

Theoretically, the natural fluorescence lifetime can be calculated from the Strickler-Berg equation.[155] Based on eq. 2.11, the radiative rate constant is related to the absorption, the emission spectra, and the refractive index of the solvent, n. It is described by

$$\frac{1}{\tau_0} = k_r = 2.88 \cdot 10^{-9} \cdot n^2 \cdot < v_f^{-3} >_{AV}^{-1} \cdot \int \frac{\varepsilon(v)}{v} dv \qquad (2.\ 11)$$

such that

$$< v_f^{-3} >_{AV}^{-1} = \frac{\int I(v) dv}{\int I(v) v^{-3} dv} \qquad (2.\ 12)$$

Here, I presents the emission intensity in the unit of frequency v, and ε is the extinction coefficient from the absorption spectrum.

The Strickler-Berg equation works under the assumptions that there is the same molecular geometry in the ground and excited state and there is no difference in the refractive index of the solvent at the absorption and emission wavelength for a fluorophore.[1, 14]

It has been reported that there is a discrepancy in the value of the natural lifetime calculated from the Strickler-Berg equation and the quantum yield definition for many fluorophores.[156-161] In these cases, the assumptions made in the model are not strictly matched by the situation in real molecular systems.

2.3.3 The Magnitude of the Electronic Transition Moment

Apart from the Strickler-Berg formula, the relationship between the radiative rate constant and the refractive index of the solvent has been derived by Toptygin and co-workers who provided a theoretical model (eq. 2.13)[162]

$$\frac{k_r}{<v^3>_{fcf}} = \frac{\gamma {n_0}^5 \cos^2\theta_x}{[{n_0}^5 + ({n_1}^2 - {n_0}^2)L_x]^2} + \frac{\gamma {n_0}^5 \cos^2\theta_y}{[{n_0}^5 + ({n_1}^2 - {n_0}^2)L_y]^2} + \frac{\gamma {n_0}^5 \cos^2\theta_z}{[{n_0}^5 + ({n_1}^2 - {n_0}^2)L_z]^2} \quad (2.13)$$

where k_r can be calculated from the quantum yield and the fluorescence lifetime of a fluorescent molecule, n_0 and n_1 represent the refractive indices of the solution and the particle, respectively. The depolarization factors L_x, L_y and L_z, that are determined by the ellipsoid axes ratio of the molecule. θ_x, θ_y and θ_z are the angles of the apparent dipole moment in the ellipsoid axes x, y and z, respectively. The term $<v^3>_{fcf}$ is the same as eq. 2.12.

$$<v^3>_{fcf} = \frac{\int_0^\infty v^3[v^{-3}I_v(v)]dv}{\int_0^\infty [v^{-3}I_v(v)]dv} \quad (2.14)$$

Here γ is related to the magnitude of apparent dipole moment M of a fluorophore, defined as follows:

$$\gamma = \frac{64\pi^4}{3h}|M|^2 \quad (2.15)$$

Here h is Planck's constant.

The model restricts the values of L_x, L_y and L_z such that they are always greater than zero, and the sum of three values equals unity. In addition, the value of $\cos^2\theta_x + \cos^2\theta_y + \cos^2\theta_z$ equals unity. The largest depolarization factor L indicates the shortest ellipsoid axis.

Assuming the polarization of M is parallel to one of the three ellipsoid axes, and then eq. 2.13 can be simplified to

$$\frac{k_r}{<v^3>_{fcf}} = \frac{\gamma {n_0}^5}{[{n_0}^2 + ({n_1}^2 - {n_0}^2)L_M]^2} \tag{2. 16}$$

where L_M is the substitute depolarization factor, given by

$$L_M = \cos^2\theta_x L_x + \cos^2\theta_y L_y + \cos^2\theta_z L_z \tag{2. 17}$$

The intrinsic electronic transition dipole moment, μ, has to be parallel to one of the ellipsoid axes is the assumption for this equation. If a fluorescent molecule is in an empty ellipsoid cavity in a solution, n_1=1 and $M = \mu$. This is the case for all the fluorescent molecules in this chapter. A rearrangement equation from eq. 2.15 and 2.16 is

$$\sqrt{\frac{{n_0}^5 <v^3>_{fcf}}{k_r}} = \frac{{n_0}^2 + P2}{P1} \tag{2. 18}$$

such that

$$P1 = \frac{8\pi^2|\mu|}{(1-L_\mu)\sqrt{3h}} \tag{2. 19}$$

$$P2 = \frac{L_\mu}{1-L_\mu} \tag{2. 20}$$

The value of L_μ is between 0 and 1, and It can be used to indicate the shape of the fluorescent molecule. It shows that the magnitude of L_μ is 1/3 for a spherical molecule. The L_μ value is more than 1/3 indicating that the transition dipole moment direction is along the shortest dimension of the ellipsoid molecule and vice versa. The shape of molecules can be described only as a sphere or an ellipsoid. However, it is difficult to discriminate a prolate and oblate ellipsoid based on this measurement. If the ratio of the longest to the shortest axis of a ellipsoid is less than 2, the simplified model (eq. 2.16) can be used.[162]

2.3.4 Solvatochromic Approaches to Dipole Moment

The solvatochromic methods provide a relationship between the Stokes shift and the dipole moment of a fluorophore in solvents upon excitation. The dipole moment of an excited fluorescent molecule offers the information of the electronic and geometrical structure of the molecule in the excited state.[163] There are several methods provided by Lippert-Mataga, Bakhshiev and Kawski-Chamma-Viallet.[163-167] The Stokes shift Δv is related to a combination of the refractive index n and dielectric constant D of the solvent, which is obtained by Lippert and Mataga et al. The corresponding formula is:

$$\Delta v = v_a - v_f = \frac{2(\mu_e - \mu_g)^2}{4\pi\varepsilon_0 a_0{}^3 hc} F1 + Const \qquad (2.\ 21)$$

such that

$$F1 = (\frac{D-1}{2D+1} - \frac{n^2-1}{2n^2+1}) \qquad (2.\ 22)$$

where ε_0 is the permittivity of the vacuum, h is Planck's constant, a_0 is the radius of the cavity, and μ_g and μ_e is the dipole moment of fluorescent molecules in the ground state and the excited state, respectively.

Bakhshiev's equation is

$$\Delta v = v_a - v_f = \frac{2(\mu_e - \mu_g)^2}{a_0{}^3 hc} F2 + Const \tag{2. 23}$$

where

$$F2 = \frac{2n^2+1}{n^2+2}\left(\frac{D-1}{D+2} - \frac{n^2-1}{n^2+2}\right) \tag{2. 24}$$

Kawski-Chamma-Viallet's model is described by:

$$\frac{\Delta v'}{2} = \frac{v_a + v_f}{2} = -\frac{2(\mu_e{}^2 - \mu_g{}^2)}{a_0{}^3 hc} F3 + Const \tag{2. 25}$$

where

$$F3 = \left[\frac{2n^2+1}{2(n^2+2)}\left(\frac{D-1}{D+2} - \frac{n^2-1}{n^2+2}\right) + \frac{3(n^4-1)}{2(n^2+2)^2}\right] \tag{2. 26}$$

The dielectric constant of binary solvents has been studied and various different models have been proposed to describe its behaviour. [168-170] The sophisticated model is able to describe in a more accurate way the dielectric constant of a mixture of solvents, but at the cost of using more parameters. In order to have an idea about the Stokes shift varying with the polarity, a simple model is used to calculate the dielectric constant of binary D_m, is given by[170]

$$D_m = \phi_1 D_1 + \phi_2 D_2 \tag{2. 27}$$

where ϕ_1, ϕ_2 are the weight fractions of the solvents 1 and 2, respectively, and D_1 and D_2 are the corresponding dielectric constant.

2.3.5 Stokes-Einstein-Debye

The Stokes-Einstein-Debye equation is used to describe the rotational property of a spherical molecule, and it is given by

$$\theta = \frac{\eta V}{k_B T} \tag{2. 28}$$

where θ is the rotational correlation time, V is the molecular volume, k_B is the Boltzmann constant, and T is the temperature in Kelvin.

Chapter 3

Viscosity Mapping using BODIPY-C_{12} via FLIM

3.1 Introduction

BODIPY-C_{12}, a fluorescent molecular rotor, was synthesised by Dr. Gokhan Yahioglu from PhotoBiotics Ltd and the Department of Chemistry, Imperial College London. It is used to measure the intracellular viscosity of HeLa cells via FLIM. Some of this work has been published.[171] The molecular structure of BODIPY-C_{12} is shown in Figure 3. 1. It consists of a single bond connecting a BODIPY unit and a long carbon chain on top of a phenyl ring. The single bond allows two planes to twist. In this chapter, an extensive study of BODIPY-C_{12} in solutions and in cells measured by FLIM and spectroscopy is presented. The location of BODIPY-C_{12} in cells will be discussed.

.

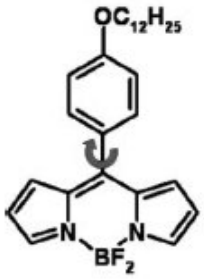

Figure 3. 1 The molecular structure of BODIPY-C_{12}.[128]

3.2 Fluorescence Properties in Methanol/Glycerol Mixtures

3.2.1 Experimental Section

A stock solution of 1.2 mg of BODIPY-C_{12} (MW=452 g/mole) in 1 ml of methanol was made which resulted in 2.65 mM concentration. Methanol/glycerol solutions with different volume fractions of glycerol were prepared in order to vary the viscosity of solutions. The volume fraction of glycerol is varied from 0% to 90% at 5% intervals. The concentration of BODIPY-C_{12} in each mixture is made up to approximately 13 µM.

The photophysical properties of BODIPY-C_{12} and its influence on solvent polarity can be characterised by UV-Vis absorption and emission spectroscopy. The solvent polarity is related to the refractive index and dielectric constant of the solvent. The solvent refractive index and dielectric constant are used to depict the solvent polarity functions (eq. 2.21, 2.23, and 2.25).[172] A four clear-side quartz cuvette (Hellma) with 2 ml of BODIPY-C_{12} solution was used to measure absorption spectrum on a spectrophotometer (Hitachi, U-4100), and emission spectra on a luminescence spectrometer (Perkin Elmer, LS-50B).

Time-resolved fluorescence measurements were taken using an inverted confocal scanning microscope. For the fluorescence lifetime measurement, 200 µl of each dye solution was placed in each well of a 96-well glass-bottom microplate (Whatman). The pulsed diode laser with a wavelength of 467 nm, pulse duration of 90 ps, and a repetition rate of 20 MHz was used to excite the samples. The fluorescence signal passed through a chromatic reflector, a pinhole, and a 520 nm band pass filter (Semrock, FF01-520/28-25) for BODIPY-C_{12} solutions and was then detected by a cooled PMT or hybrid PMT detector. The experimental setup is shown in Figure 3. 2.

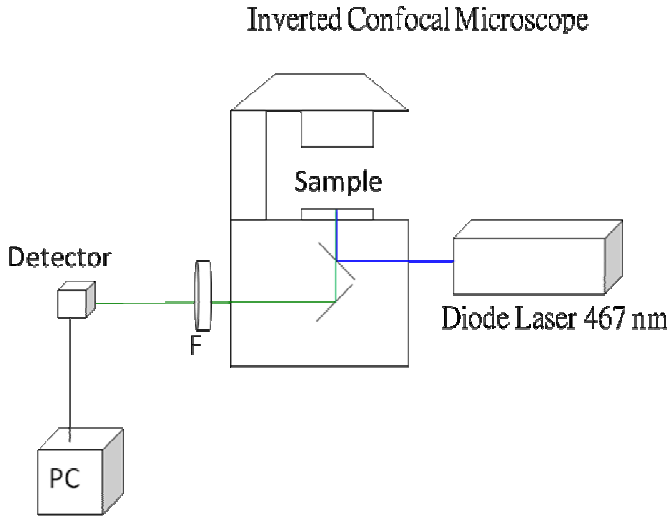

Figure 3. 2 Experimental setup for time-resolved fluorescence lifetime measurements. F denotes bandpass filter.

3.2.2 Solvent Properties: Viscosity, Refractive Index, and Dielectric Constant

The viscosity of methanol/glycerol mixtures with some volume fractions of glycerol was measured using an advanced rheometric expansion system rheometer at 22.0 ± 0.1 ℃, and the results were published.[128] The viscosity of binary liquids has been studied.[173, 174] The intermediate viscosities of methanol/glycerol mixtures are estimated using a model. Here, the Arrhenius equation is used, and the corresponding formula is[174]

$$\log \eta_{mix} = x_1 \cdot \log \eta_1 + x_2 \cdot \log \eta_2 \qquad (3.\ 1)$$

where η_{mix}, η_1 and η_2 are the viscosities of mixtures, pure solvent 1 and solvent 2, respectively. x_1 and x_2 represent the volume fractions of solvent 1 and 2, respectively. Figure 3. 3(a) shows a variation in viscosity of methanol/glycerol solutions from the volume fraction of glycerol. The data are from the experimental measurements[100, 128] and estimations using the Arrhenius model (eq. 3.1). The viscosity of 100% glycerol at 22℃ was calculated to be 1182 cP according to a table of viscosity versus temperature for glycerol solutions.[175] It

seems that the difference in viscosity between two data sets is clear on the plot with a logarithmical viscosity scale (see Figure 3. 3(b)). The viscosity of mixtures estimated by using eq. 3.1 seems to be consistent with the experimental one. In this experiment, we use the viscosities estimated using eq. 3.1.

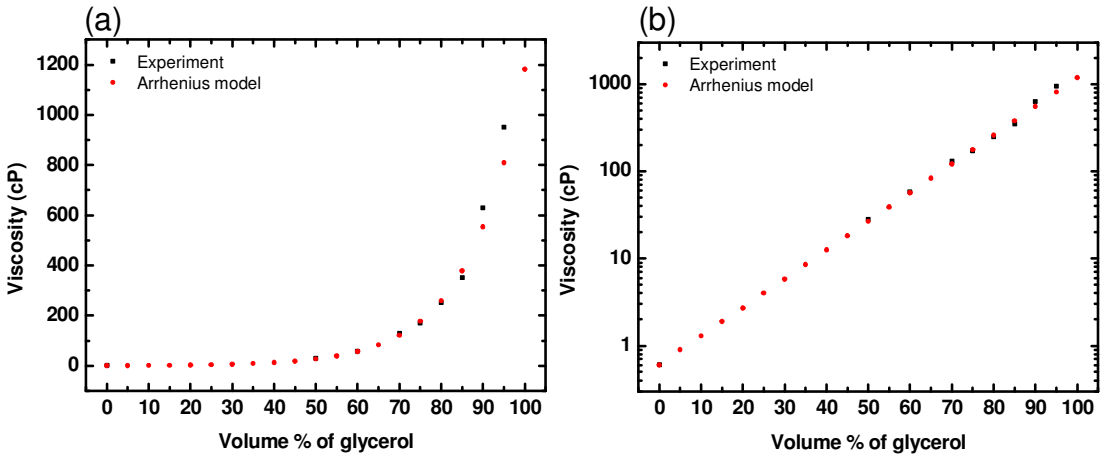

Figure 3. 3 (a) Linear viscosity scale versus the volume fraction of glycerol for methanol/glycerol solutions using the Arrhenius model (●) and experimental results (■) at 22℃. (b) Logarithmic viscosity scale versus the volume fraction of glycerol.

The refractive index was measured via a refractometer at 589 nm,[134] and the dielectric constant was calculated using eq. 2.27, shown in Table 3. 1. The dielectric constant is 31 for methanol and 39.4 for glycerol at 28℃.[168]

Table 3. 1 The refractive index and dielectric constants of methanol and glycerol mixtures.

Volume % of glycerol	Refractive index	Dielectric constant (28℃)
0	1.3322	31.01
5	1.3403	31.66
10	1.3546	32.27
15	1.3599	32.86
20	1.3690	33.40
25	1.3769	33.93
30	1.3866	34.42
35	1.3939	34.89
40	1.4037	35.34
45	1.4125	35.77
50	1.4210	36.18
55	1.4260	36.57
60	1.4320	36.94
65	1.4384	37.29
70	1.4451	37.64
75	1.4527	37.96
80	1.4558	38.28
85	1.4620	38.58
90	1.4669	38.87

3.2.3 Absorption and Emission spectra of BODIPY-C_{12}

The information of dipole moment and the influence of the solvent effect on the fluorophore is useful to understand the photophysical processes.[163, 172] Based on solvatochromic methods, the Stokes shift is related to the dipole moment for fluorophores.[166, 167, 172, 176] Here, we measured the absorption and emission spectra of BODIPY-C_{12} in methanol/glycerol mixtures. The position of the absorption and emission peaks of BODIPY-C_{12} varied slightly with the different polarity of solutions as shown in Figure 3. 4 for 10% and 90% volume fraction of glycerol.

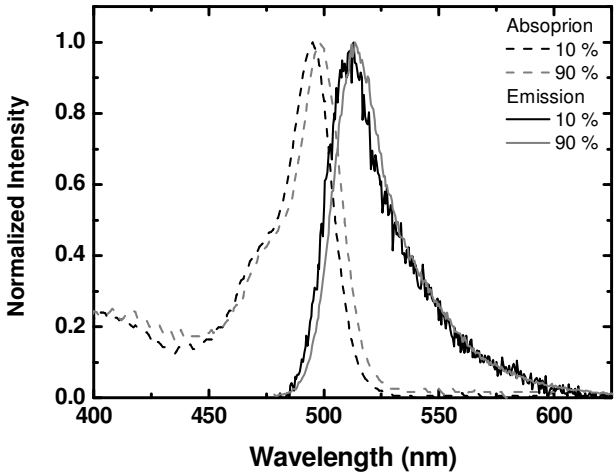

Figure 3. 4 The absorption (dashed line) and emission spectra (solid line) of BODIPY-C_{12} in glycerol and methanol mixtures with 10 and 90% of glycerol by volume. The excitation wavelength is 470 nm for emission spectra.

From the absorption and emission spectra, the peaks of absorption and emission bands can be analysed. The absorption and emission peaks are red shifted with higher refractive index (see Figure 3. 5(a)). According to the Lippert-Mataga's equation (eq. 2.21) and Bakhsiev's theory (eq. 2.23), the Stokes shift of BODIPY-C_{12} in all mixtures is almost the same independently of the polarity parameters, as shown in Figure 3. 5(b, c). A small Stokes shift of BODIPY-C_{12} (~620 cm^{-1}) is in agreement with the literature values of other meso-substituted BODIPY (500-900 cm^{-1}).[93] The differences between the excited-state and the ground dipole moment stay constant among these mixtures due to the negligible slope in the plot. Using another solvatochromic model (eq. 2.25), the peak wavenumber shift is negatively proportional to the polarity function shown in Figure 3. 5(d). It was found that the magnitude of μ_e is greater than that of μ_g from the gradient of the plot. The value of $\mu_e^2 - \mu_g^2$ is 4.87 Debye^2 (D^2) when a cavity radius of 0.3 nm is applied to eq. 2.25.

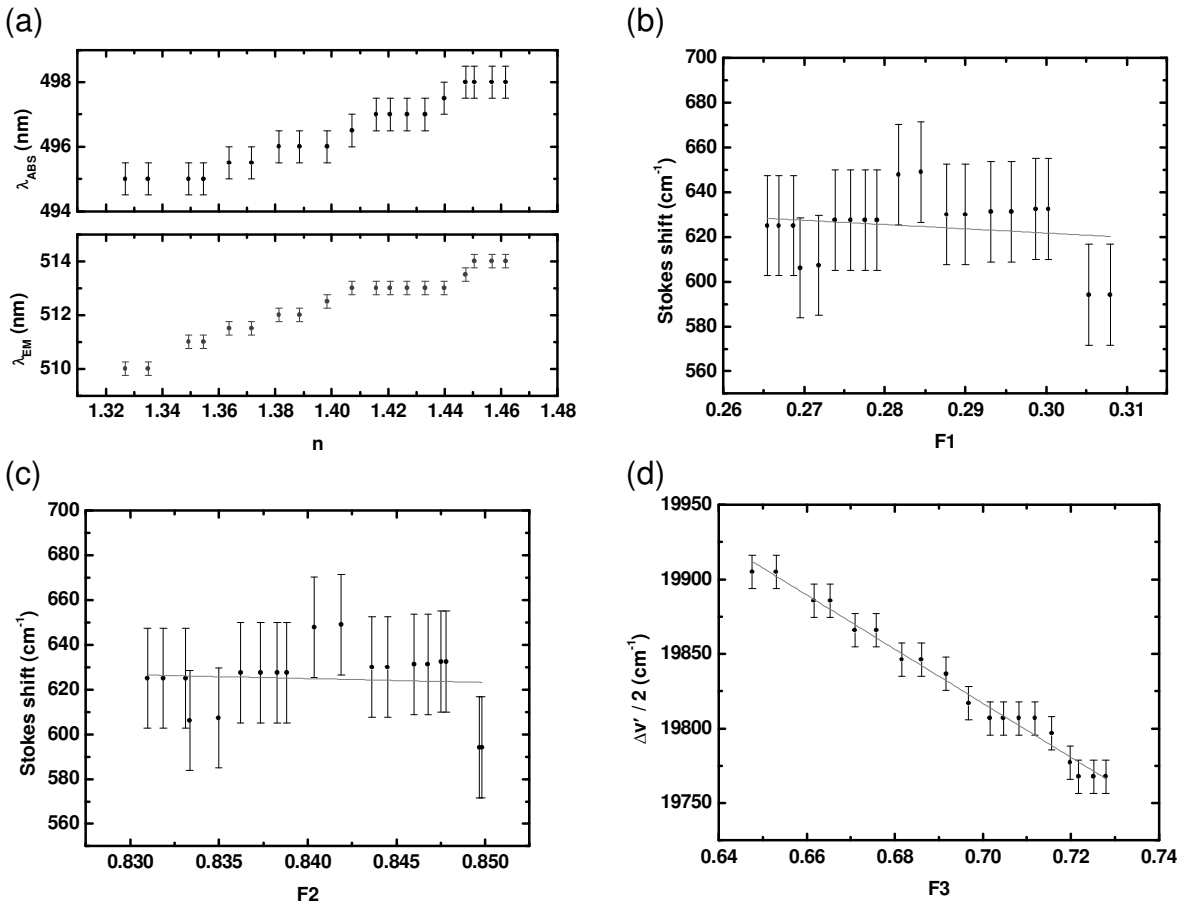

Figure 3. 5 (a) The absorption and emission peaks of BODIPY-C_{12} versus refractive index in methanol and glycerol mixtures. (b-c) The relationship between Stokes shift of BODIPY-C_{12} and the polarity parameters of methanol and glycerol mixtures. (d) Plot of $(v_a + v_f)/2$ versus F3 for BODIPY-C_{12} in the same solutions as (a). The grey straight lines are the best fit to the data. (Adjusted R-Square (Adj. R-Square) = -0.027 (b), -0.053 (c) and 0.983 (d))

3.2.4 Fluorescence Quantum Yield of BODIPY-C_{12}

The fluorescence quantum yield of BODIPY-C_{12} in methanol/glycerol solutions in two different ways were measured in two different ways, both based on the relative method. The first way uses the same viscosity solution with four different dye concentrations for each viscosity sample. The second way measures the same dye concentration in different viscosity solutions. The relative method to determine the fluorescence quantum yield Φ is calculated according to eq. 3.2.[177]

$$\Phi_X = \Phi_{ST}\left(\frac{A_{ST}}{A_X}\right)\left(\frac{I_X}{I_{ST}}\right)\left(\frac{n_X^{\,2}}{n_{ST}^{\,2}}\right) \qquad (3.\ 2)$$

where A is the absorbance of the fluorophore, I is the total emission intensity, and subscript X and ST denote unknown and standard sample, respectively. For this experiment, a *μM* concentration of the fluorophore is used to avoid re-absorption effect which is fluorescence from the excited molecules exciting the ground state molecules. This is possible because the Stokes shift of BODIPY-C_{12} is small, and there is an overlap between absorption and emission spectra as shown in Figure 3. 4. The re-absorption effect results in a red-shifted emission spectrum, and depends on the overlap between the molecular absorption and fluorescence spectrum, the solution concentration and the thickness of sample.[178]

For the first experiment, a set of BODIPY-C_{12} solutions with ten different viscosities containing four different dye concentrations was measured. Fluorescein in 0.1M NaOH is used as a standard reference, because the absorption and emission spectra of fluorescein are similar to that of BODIPY-C_{12}. In addition, the fluorescence quantum yield of fluorescein in 0.1M NaOH is 0.92.[179] The relationship between fluorescence intensity and absorbance for BODIPY-C_{12} and fluorescein is given in the appendix (see Figure A.1), and the gradient of plots indicate the magnitude of I_X / A_X and I_{ST} / A_{ST} for BODIPY-C_{12} and fluorescein, respectively. The value of $(A_{ST} / A_X) \cdot (I_X / I_{ST})$ (eq. 3.2) was calculated from the gradient of Figure A.1 for BODIPY-C_{12} derived by that for fluorescein. The fluorescence quantum yield of BODIPY-C_{12} in mixtures can therefore be calculated. The standard deviation of quantum yield of BODIPY-C_{12} is calculated using the standard deviation of the gradient of the plot (Figure A.1) and calculating the standard deviation of the refractive index of solutions through eq. 3.2. The quantum yield of BODIPY-C_{12} versus viscosity is shown in Figure 3. 6.

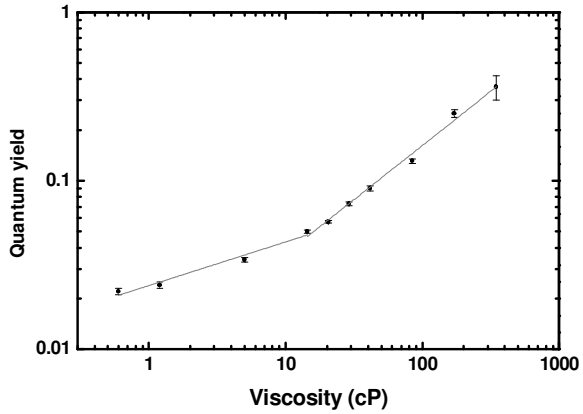

Figure 3. 6 The fluorescence quantum yield of BODIPY-C_{12} versus viscosity in methanol/glycerol mixtures. The grey straight lines are the best fit to the data.

Figure 3. 6 shows that the quantum yield of BODIPY-C_{12} increases with viscosity. The slope of the plot in Figure 3. 6 is the value of α according to eq. 2.9. It was found that there are two α values in the viscosity range from 0.6 cP to 1000 cP. The transition point between two gradients is at around 14 cP. The gradient is 0.26 ± 0.03 (Adj. R-Square = 0.962) for viscosity lower than 14 cP and 0.64 ± 0.02 (Adj. R-Square = 0.991) for a viscosity higher than 14 cP, respectively. This phenomenon of fluorescence quantum yield varying with the viscosity with different α according to eq. 2.9 has also been observed in previous work on fluorescent molecular rotors and has been reported in the literature.[153, 180, 181] The proposed reason for this is the free volume effect. The free volume exists around the fluorophores, and thus the environment of solution molecules is not expected to have an effect on the fluorophores. Because of this, the change in the quantum yield of BODIPY-C_{12} in low viscosity solutions is minimal.

The other method is a comparison between BODIPY-C_{12} in methanol and methanol/glycerol solution with same dye concentration using eq. 3.2. The absorption and emission spectra were used from the measurements in section 3.2.3. The calculation assumes the same extinction coefficient of BODIPY-C_{12} in mixtures and uses 0.022 for the quantum yield of BODIPY-C_{12} in methanol (from the first quantum yield experiment). The fluorescence quantum yields of

BODIPY-C_{12} in methanol/glycerol mixtures for both measurements and from previously published values are shown in Figure 3. 7. The gradients of plot (see black points in Figure 3. 7) are 0.25 ± 0.02 and 0.61 ± 0.03. The red points are from Figure 3. 6. The two measurements in this work are consistent. We also compare the fluorescence quantum yields from this work and the literature values which are denoted in blue. The fluorescence quantum yields in the literature are higher than the work we present here. In addition, the gradient of the plot from the literature is 0.72 ± 0.05 and an intercept is -1.94 ± 0.10. It could be that the reference for the fluorescence quantum yield measurements was wrong in the literature, because there is a constant offset between the data sets, but the same trend. In any case, all data sets show the characteristic behaviour of a fluorescent molecular rotor.

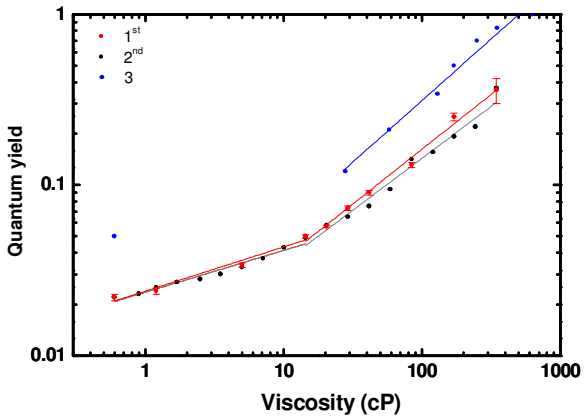

Figure 3. 7 A comparison of fluorescence quantum yield of BODIPY-C_{12} in methanol/glycerol mixtures using the relative method. The fluorescence quantum yield of all mixtures is calculated compare to that of fluorescein (●) and BODIPY-C_{12} in methanol (●).The data (●) is from the literature.[100]

3.2.5 Fluorescence Lifetime of BODIPY-C_{12}

The emission intensity and fluorescence quantum yield of BODIPY-C_{12} increase with the viscosity of the environment. According to the Förster-Hoffmann equation, a double-logarithmic plot of emission intensity versus viscosity is a straight line for a constant dye concentration. However, it is not easy to control the concentration of BODIPY-C_{12} within cell environments or other complicated systems, such as a sol-gel system. Distinguishing the viscosity effect from the

concentration effect by integrated intensity is difficult. On the other hand, measuring the fluorescence lifetime of fluorescent molecular rotors is not influenced by the concentration of fluorophores, and the fluorescence lifetime can be measured directly and more accurately than the fluorescence quantum yield. Hence the latter has an advantage over intensity measurements.

The fluorescence decays of BODIPY-C_{12} in methanol/glycerol solutions were measured, shown in Figure 3. 8. We used software to analyse the fluorescence lifetime by fitting a monoexponential decay function. As seen in Figure 3. 9, lifetime increases as viscosity increases. The fluorescence lifetime of BODIPY-C_{12} in methanol is 0.28 ns using the PMT detector. The time scale of lifetime and IRF are similar. Therefore, the fluorescence decay of BODIPY-C_{12} in methanol was measured again using the hybrid PMT detector. The fluorescence lifetime of dye is approximately 0.29 ns, which is consistent with that obtained by the PMT detector. It has been reported that lifetime of BODIPY-C_{12} in ethanol is 0.38 ns using a microchannel plate detector and 100 MHz diode laser.[182] We also demonstrate that the lifetime of BODIPY-C_{12} in pure glycerol can be up to 4.60 ns.

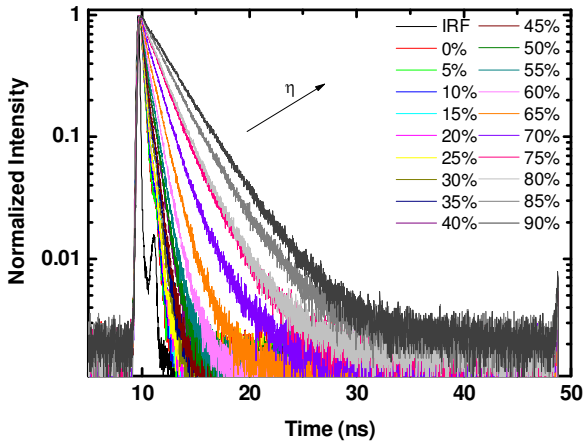

Figure 3. 8 Fluorescence decays of BODIPY-C_{12} in methanol/glycerol mixtures were detected by a PMT detector. A diode laser with a wavelength of 467 nm and a repetition rate of 20 MHz is used to excite the BODIPY-C_{12} solution, and an emission window of 506-534 nm is used to measure the fluorescence decays.

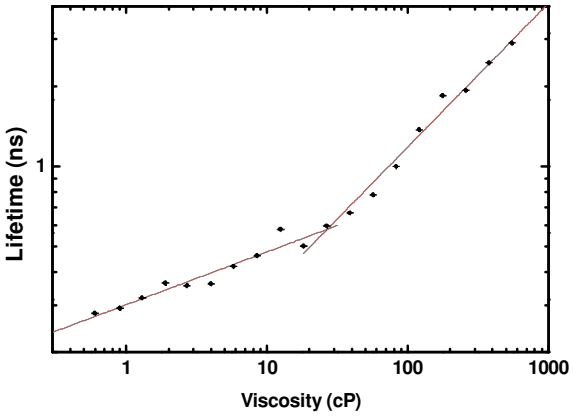

Figure 3. 9 The fluorescence lifetime of BODIPY-C_{12} in methanol/glycerol mixtures of various viscosities on a logarithmic lifetime and viscosity scale. The grey lines are the best fit to the data.

According to eq. 2.10, the relationship between lifetime and viscosity is linear on a log-log scale. The gradient in the higher viscosity region is 0.55 ± 0.03 (Adj. R-Square = 0.985), in agreement with the literature value.[128] The lower viscosity slope is 0.20 ± 0.02 (Adj. R-Square = 0.906). Both values and the transition point between the two gradients are consistent with that from the fluorescence quantum yield measurements (section 3.2.4). The slightly higher value of the gradient in the fluorescence quantum yield plot Figure 3. 6 maybe due to the small effect of the refractive index, which inevitably changes as the glycerol

content of the solutions is increased. An increase in refractive index increases the radiative rate constant (k_r) as discussed below. This increases the fluorescence quantum yield, but decreases the fluorescence lifetime according to eq. 1.1 and eq. 1.2. Thus, fluorescence lifetime information can be converted to viscosity information by measuring the fluorescence lifetime of BODIPY-C_{12} in an unknown system. This is used as a calibration for indicating the intracellular viscosity.

The radiative and non-radiative rate constant of BODIPY-C_{12} was calculated by knowing the fluorescence quantum yield and the fluorescence lifetime according to eq. 1.1 and eq. 1.2. This system of two equations with two unknowns can be solved unambiguously by measuring the fluorescence quantum yield and the fluorescence lifetime. The results are shown in Figure 3.10. The non-radiative rate constant of BODIPY-C_{12} dominates the quantum yield and lifetime, and varies with the viscosity of the solutions. In contrast, the radiative rate constant has a minor effect on quantum yield or fluorescence lifetime. The radiative rate constant plotted versus the square of the refractive index of the solution is shown in Figure 3.11. According to eq. 2.11, a straight line is used to fit the plot (Figure 3.11), with an intercept of zero. The change of the rate constant is ~20% between a refractive index of 1.33 and 1.47 (viscosity from 0.6 to 630 cP).

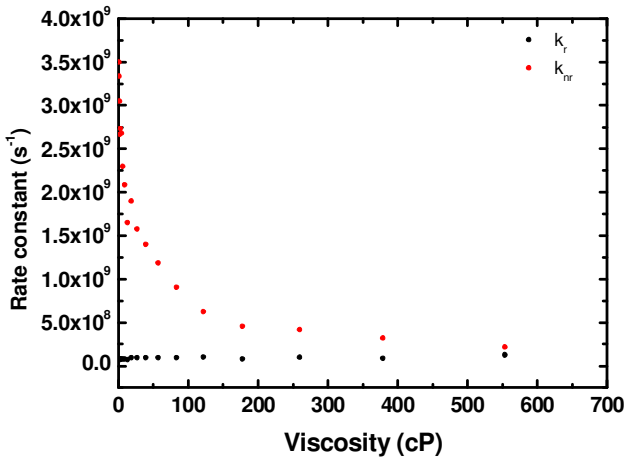

Figure 3.10 The radiative rate (●) and non-radiative rate (●) constant of BODIPY-C_{12} in methanol/glycerol solutions.

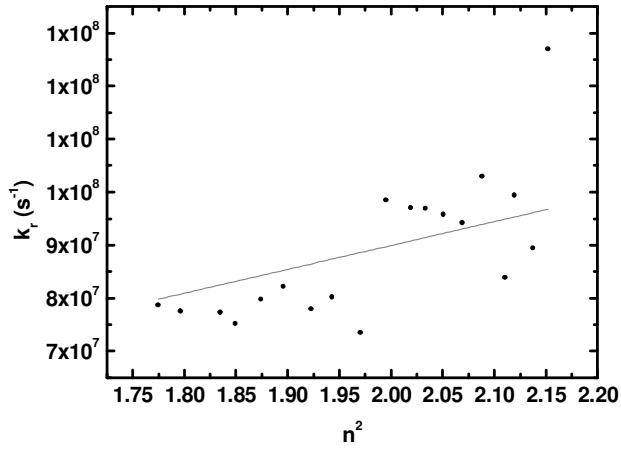

Figure 3.11 Radiative rate constant versus the square of the refractive index for BODIPY-C_{12} in methanol/glycerol mixtures. The grey linear line with a gradient of $(4.50 \pm 0.11) \times 10^7$ s^{-1} through the origin (Adj. R-Square = 0.987).

The non-radiative rate constant for a fluorescent molecular rotor can be related to the free volume concept based on the work by Loutfy and his co-worker.[60, 180, 181]

$$k_{nr} = k_{nr}^0 \cdot \exp(-\alpha \frac{V_0}{V_f}) \tag{3. 3}$$

where k_{nr} is the non-radiative rate constant, k_{nr}^0 is the free-rotor reorientation rate, α is a constant which is the same α as eq. 2.9, V_0 is the Van der Waals volume of the fluorophore, and V_f is the free volume of the solvent.

The viscosity of the solvent, η, is a function of the free volume of the solvent.[183]

$$\eta = \eta_0 \cdot \exp(\frac{V_0}{V_f}) \tag{3. 4}$$

where η_0 is a constant.

Thus the non-radiative rate constant of a fluorescent molecular rotor is a function of viscosity, and it is given by

$$k_{nr} = k_{nr}^0 \cdot (\frac{\eta}{\eta_0})^{-\alpha} \quad (3.5)$$

A plot of the logarithm of the non-radiative rate constant versus the viscosity of BODIPY-C_{12} in methanol/glycerol mixtures is shown in Figure 3.12. According to eq. 3.5, the data was fit with a straight line, and there are two straight lines in viscosity between 0.6 and 600 cP. For low viscosities, a straight line with a gradient of -0.21 ± 0.02 and an intercept of 8.89 ± 0.05 is obtained. For the expression in high viscosities, a straight line with a gradient of -0.54 ± 0.04 and an intercept of 8.29 ± 0.05 is obtained. The gradients are in agreement with those from fluorescence quantum yield and lifetime measurements. Moreover, it shows the free volume plays an important role in fluorescence mechanism of fluorescent molecular rotors.

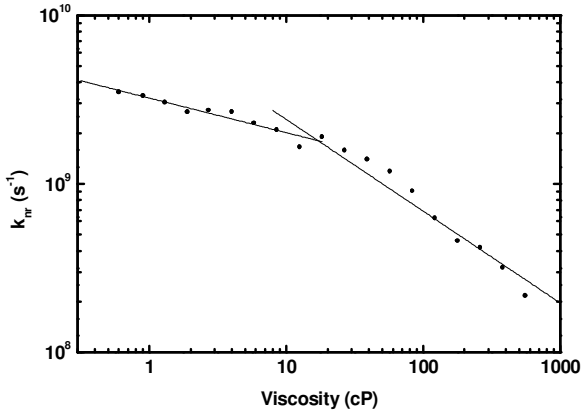

Figure 3.12 A plot of non-radiative rate constant versus viscosity of BODIPY-C_{12} in methanol/glycerol mixtures.

The fluorescence lifetime of BODIPY-C_{12} is relatively longer than other fluorescent molecular rotors. The fluorescence lifetime of BODIPY-C_{12} is from 280 ps to 4.60 ns for viscosity of methanol/glycerol mixtures from 0.6 cP to 1470 cP. In contrast, the fluorescence lifetime of DCVJ or CCVJ is extremely short, even at high viscosity solution (~75 ps at 300 cP).[129] The fluorescence quantum yield of DCVJ is very low, which is 0.1 in glycerol at 954 cP.[181] In addition, it is complicated to deal with multiple lifetimes of a fluorophore, such as Thioflavin T.[99] It has also been demonstrated that, for some fluorescent molecular rotors, the relationship between fluorescence lifetime and viscosity varies with the detection wavelength.[99] BODIPY-C_{12} shows a single exponential decay, has a reasonable long fluorescence lifetime and higher fluorescence quantum yield than DCVJ. Hence, BODIPY-C_{12} is a good candidate as viscosity sensor via FLIM.

3.3 BODIPY-C_{12} in Live Cells

It has been shown that fluorescence lifetime of BODIPY-C_{12} is related to solvent viscosity (Figure 3. 9). We use the calibrations of fluorescence lifetime versus viscosity in Figure 3. 9 to study the viscosity of cells.

3.3.1 Experimental Section

Human cervix carcinoma (HeLa) Cells (ATCC) were cultured on a 75 cm^2 culture flask (Greiner) in DMEM with 10% FBS, 1% 1x non essential amino acid, 1 mM sodium-pyruvate and 0.1 % penicillin/streptomycin at 37℃ in a 95% air/5% CO_2 incubator. The cells were harvested by 2 ml of 1X trypsin and diluted with culture medium. A few of ml of cell solution was seeded in a 6-well glass bottom plate (WaferGen smartslide-6^{TM} micro-incubator) one night before imaging.

For staining, a volume of 20 µl of BODIPY-C_{12} (2.65 mM) was added into a well of a micro-incubator and slightly shaken, then placed into an incubator for 30 minutes. The next step was to remove the solution and wash cells with clear DMEM five times. Finally, a well of the micro-incubator was filled by DMEM at 37℃ with 5% CO_2 atmosphere and was placed on the stage of the microscope to measure FLIM of BODIPY-C_{12} in HeLa cells.

BODIPY-C_{12} uptake has been reported in SK-OV-3 cells, showing a punctate and more diffuse distribution. However the precise location of BODIPY-C_{12} in cells is not entirely clear.[100, 128] In order to know the location of BODIPY-C_{12} in cells, we use counterstaining technique applied to a well studied study cell type. For counterstaining experiments, HeLa cells were grown on a 6-well micro-incubator in Opti-MEM. The cells were stained with 20 µl of 628 µM Nile red (Invitrogen) and 20 µl of 2.65 mM BODIPY-C_{12} in one of 6-well plate in an incubator for 30 minutes. Afterwards, the medium was removed and rinsed with Opti-MEM. Confocal fluorescent images of HeLa cells in Opti-MEM were then taken. This experiment illustrates the location of BODIPY-C_{12} in the cells.

In addition to the above, Endoplasmic Reticulum-Red Fluorescent Protein (ER-RFP) (CellLight^{TM} BacMam 2.0) was used to bind Endoplasmic Reticulum (ER), and few µl of ER-RFP regent were added into the cell flask and incubated for

one night. When the regent was expressed in HeLa cells, the cells were seeded on a 6-well micro-incubator. A volume of 20 µl of BODIPY-C_{12} (2.65 mM) was added into a well of the micro-incubator and incubated for 30 minutes. Finally, the cells were immersed in the well with Opti-MEM and the cells were imaged after washing five times with Opti-MEM.

3.3.2 FLIM

By measuring the fluorescence lifetime of BODIPY-C_{12} in live cells related to the calibration (Figure 3. 9), the viscosity of the environment of BODIPY-C_{12} in cells can be calculated. FLIM of HeLa cells incubated with BODIPY-C_{12} was carried out at 32 and 37°C. The fluorescence intensity images and FLIM of BODIPY-C_{12} in cells are shown in Figure 3.13(a-d). The first column of Figure 3.13 is the measurement at 37°C, and the second column is for the measurement at 32°C. The fluorescence intensity images indicate dye uptake in HeLa cells. More intense fluorescence puncta does not necessarily mean the existence of more fluorophores, since it may be due to a higher fluorescence quantum yield resulting from higher viscosity. According to eq. 2.9, the fluorescence quantum yield of fluorescent molecular rotors increases with viscosity. Hence, both the concentration of a fluorescent molecular rotor and the solvent viscosity vary the fluorescence intensity. The fluorescence lifetime can discriminate between these effects. A monoexponential decay function was used to fit the fluorescence decay in each pixel. The colour bars from blue to red denote the fluorescence lifetime from 900 ps to 2500 ps for both images (see Figure 3.13(c, d)). The representative fluorescence decays in a single pixel for Figure 3.13(c, d) are shown in Figure 3.13(e, f). HeLa cells measured at 32°C demonstrated a longer fluorescence lifetime for BODIPY-C_{12} than those measured at 37°C. Figure 3.13(g, h) shows that there is a broad and asymmetric lifetime distribution histogram of BODIPY-C_{12} in cells. A Gaussian distribution was used to fit the lifetime histogram in the whole image. The fluorescence lifetimes of BODIPY-C_{12} measured at 37°C were found to be 1.29 ns in puncta and 1.57 ns

in other regions. The corresponding viscosity in puncta is 118 cP and the viscosity outside of puncta is 169 cP. On the other hand, the lifetimes were found to be 1.50 ns in puncta and 1.90 ns in other regions for BODIPY-C_{12} in HeLa cells at 32°C. The intracellular viscosities at 32°C are 155 cP and 241 cP. This indicates that the decreasing temperature results in an increase in viscosity. This is consistent with BODPIPY-C_{12} not being located in the cell cytoplasm because the viscosity is known to be much lower there. Moreover, BODIPY-C_{12} is hydrophobic, and is not expected to reside in the cell cytoplasm.

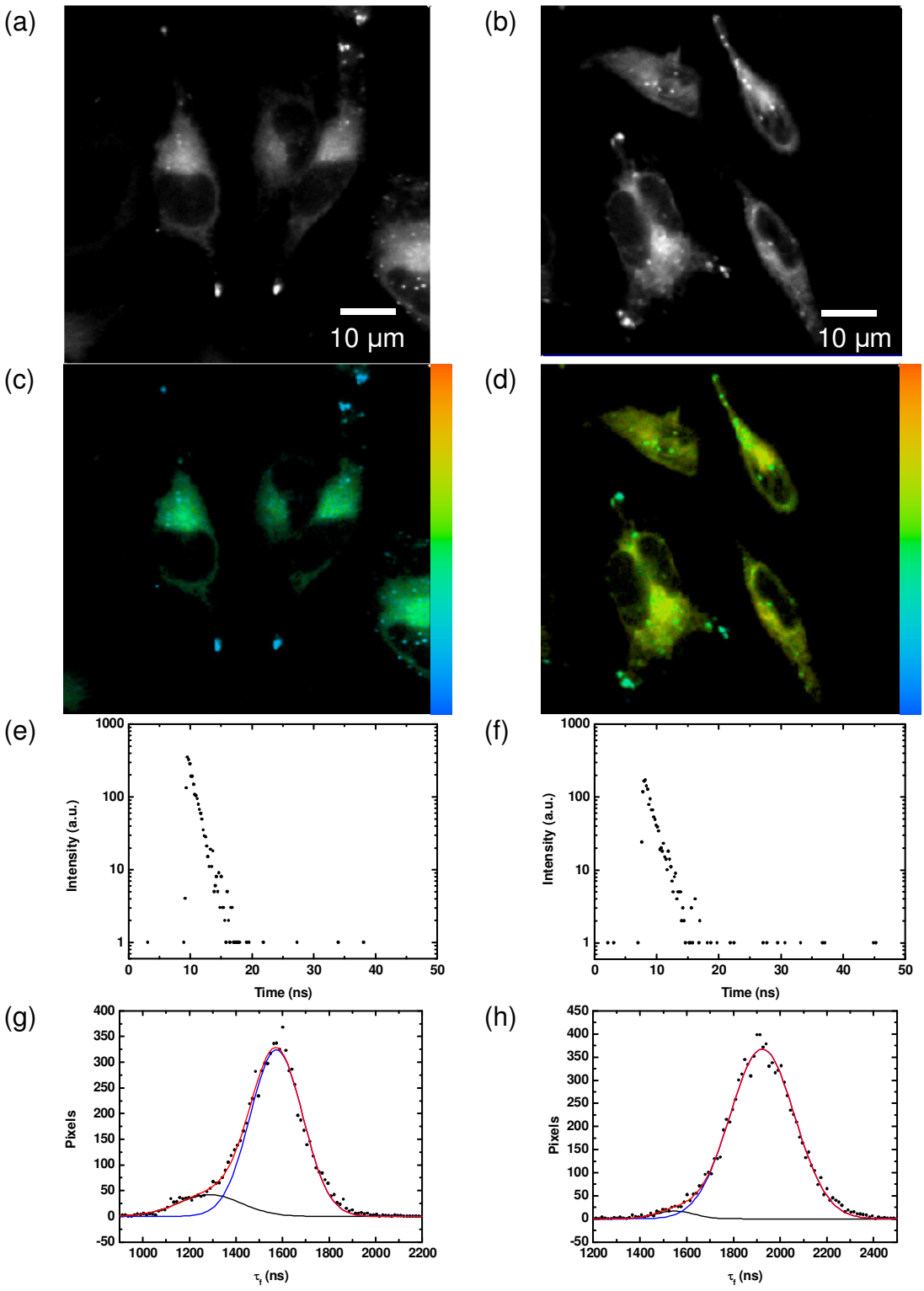

Figure 3.13 The fluorescence intensity image (a, b) and FLIM (c, d) for BODIPY-C_{12} in live HeLa cells at (a, c) 37℃ and (b, d) 32℃, respectively. (c, d) The colour bars from blue to red denote fluorescence lifetime from 900 ps to 2500 ps. (e, g) The representative fluorescence decay in a single pixel for (c, d), respectively. (g, h) The fluorescence lifetime histogram is from (c) and (d), respectively.

A comparison of viscosity changing with temperature between aqueous glycerol solutions and cell environments is shown in Figure 3.14. The viscosity of glycerol solutions decreases as temperatures increases, as shown in black and blue colour of Figure 3.14. The viscosity in cells is denoted as red and light blue, and it seems that the trend of viscosity varying with temperature for cell environments is consistent with that for solutions. It shows that the viscosity behaviour in cells is dependent on temperature, and that our method to perform FLIM of a BODIPY-C_{12} fluorescent molecular rotor in living cells is sensitive enough to detect these subtle changes.

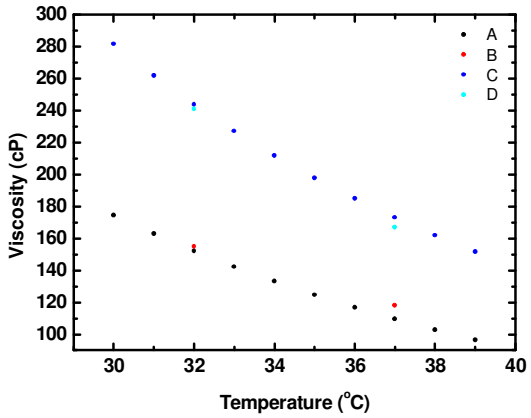

Figure 3.14 Viscosity versus temperature. Glycerol solutions containing (A) 93% of glycerol by weight and (C) 96% of glycerol by weight.[175] Intracellular viscosity measured using BODIPY-C_{12} (B) in puncta and (D) in the regions outside puncta.

It has been demonstrated that the viscosity of intracellular vesicles is 160 cP for Human ovary adenocarcinoma (SK-OV-3) using BODIPY-C_{12} via FLIM.[100, 128] It can be seen that the viscosities for HeLa, SK-OV-3 and Chinese hamster ovary (CHO) cells are the same order of magnitude.[109, 129] BODIPY-C_{12} is suggested to be membrane soluble because of its hydrophobicity.[100, 128] It has been shown that the intracellular viscosities of HeLa cells are also in agreement with that of synthetic membrane of 70-127 cP.[126]

3.3.3 The Location of BODIPY-C_{12} in Cells

No uptake of BODIPY-C_{12} for lysosomes in SK-OV-3 cells has been reported.[128] However, the location of BODIPY-C_{12} in cells has not been obtained. In this section, we demonstrate the interaction of BODIPY-C_{12} and two organelles. In the first part of experiments, Nile red and BODIPY-C_{12} were incubated with cells. Confocal fluorescence images were used to examine the localization of dyes.

It has been reported that the viscosity of cells is associated with some diseases. The locations of BODIPY-C_{12} in cells allow us to know the viscosity of the organelles it is located in, and extend our knowledge of the respective organelles. This is relevant for example, for drug design to improve drug delivery.

A confocal fluorescence image of HeLa cells incubated with BODIPY-C_{12} is shown in Figure 3.15(a, b). The contrast between puncta and some networks very different intensities, as shown in Figure 3.15(b). In order to find out the location of BODIPY-C_{12} in cells, we imaged HeLa cells incubated with ER-RFP, Rh123 and Nile red, as shown in Figure 3.15(c-e), respectively. ER-RFP is used to stain the ER organelle, Nile red is targeting the lipid droplets and Rh123 is used to stain mitochondria. The puncta of HeLa cells incubated with Nile red are lipid droplets, but the networks of cells is not clear, as shown in Figure 3.15(e). The features of BODIPY-C_{12} in HeLa cells are similar to that of lipid droplets and ER, but not to mitochondria.

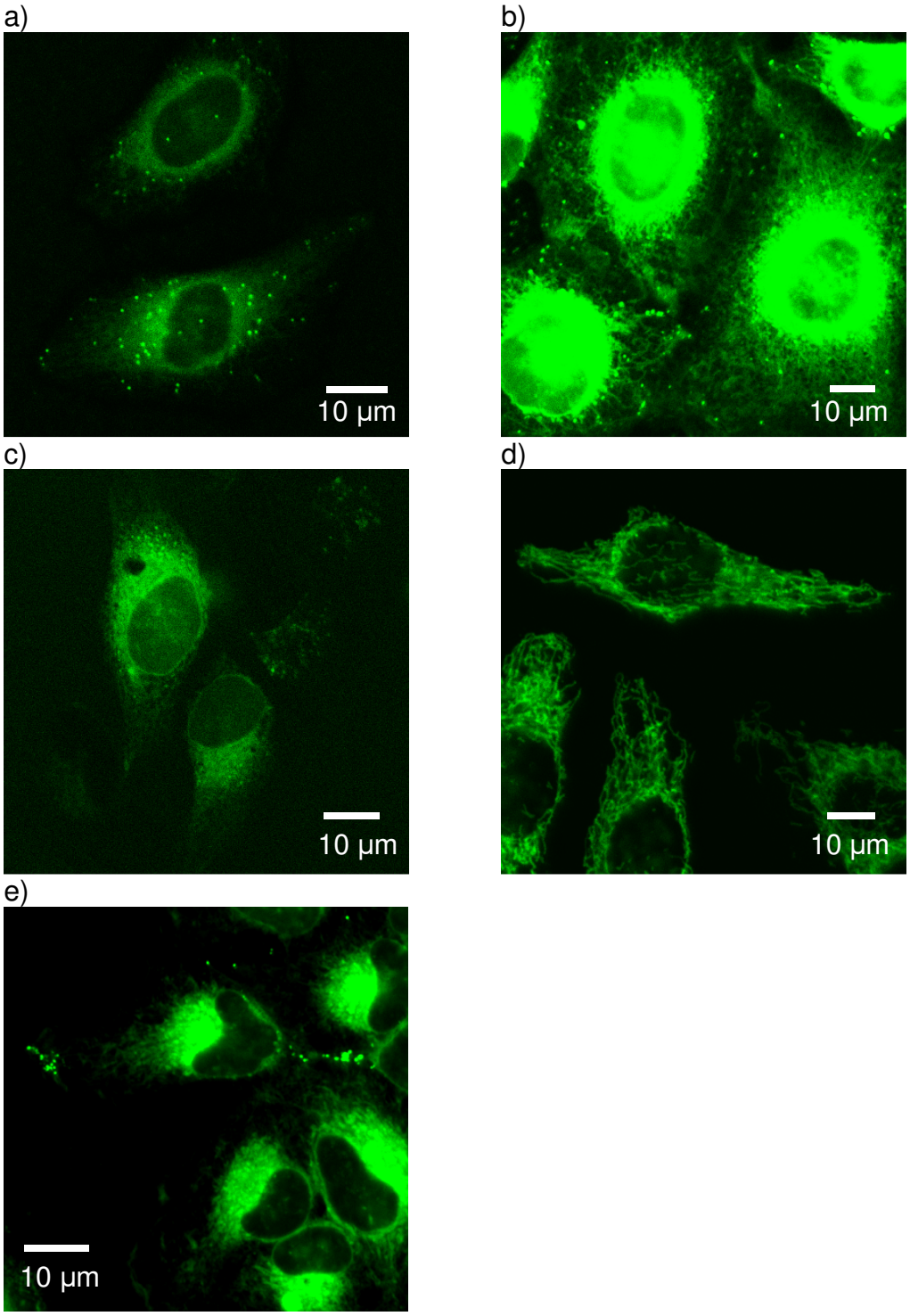

Figure 3.15 Fluorescence images of BODIPY-C_{12} in HeLa cells at 37℃ at (a) lower gain and (b) higher gain of the detector. Fluorescence images of HeLa cells stained with (c) ER-RFP, (d) Rh123, and (e) Nile red, respectively.

We did counterstaining experiments to demonstrate the location of BODIPY-C_{12} in HeLa cells. First, HeLa cells were incubated with Nile red and BODIPY-C_{12}, shown in Figure 3.16. The emission spectra of 3 regions of interest (ROIs) show

the fluorescent superimposition of BODIPY-C_{12} and Nile red. The emission peak around 515 nm is fluorescence of BODIPY-C_{12} and the emission wavelength of Nile red in HeLa cells is between 500 and 750 nm. It has two main peaks at 570 and 630 nm denoting the different polarity environments. Nile red is associated with the position of lipid droplets of cells, especially neutral lipids. The emission wavelength of Nile red is dependent on the polarity of the environment.[184, 185] Therefore, the polarity of the environments can be found from the emission wavelength of Nile red. It has been reported that the emission peak of Nile red is shifting from 570 nm to 636 nm for the surrounding solutions from non-polar to polar.[98] The wavelength of emission peak of 570 nm for Nile red in puncta denotes a non-polar environment, which is in agreement as lipids are non-polar molecules. It seems that the polarity of puncta is lower than that outside puncta regions.

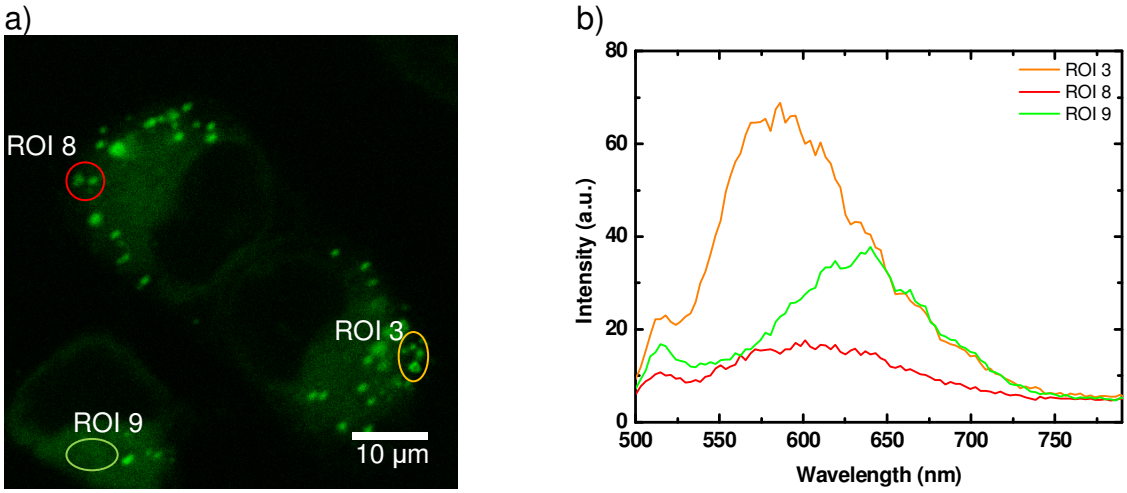

Figure 3.16 (a) Confocal fluorescence image of HeLa incubated with BODIPY-C_{12} and Nile red, and (b) the corresponding emission spectrum of three ROIs. Nile red is a polarity sensor, and red shift of emission spectrum denotes higher polarity environment. Therefore, the polarity of puncta is lower than in other regions. A continuous wave 488 nm Ar^+ laser is used to excite the sample.

The confocal fluorescence images of HeLa cells stained with Nile red and BODIPY-C_{12} are detected with two different emission windows and a pinhole of 0.9 airy units shown in Figure 3.17. The transmission images of cells shown

in Figure 3.17(a, b), the fluorescence of BODIPY-C_{12} in Figure 3.17(c, d), the fluorescence of Nile red in Figure 3.17(e, f) and the overlap images depicted in Figure 3.17(g, h). The detected emission spectra in the spectral regions of 495-520 nm and 503-531 nm were used to denote the location of BODIPY-C_{12} in HeLa cells (green colour). The emission wavelength in the spectral regions of 650-700 nm and 658-703 nm were used to denote the location of Nile red (red colour). The colour of overlap images shows Nile red and BODIPY-C_{12} in HeLa cells are in the same locations within the optical resolution.

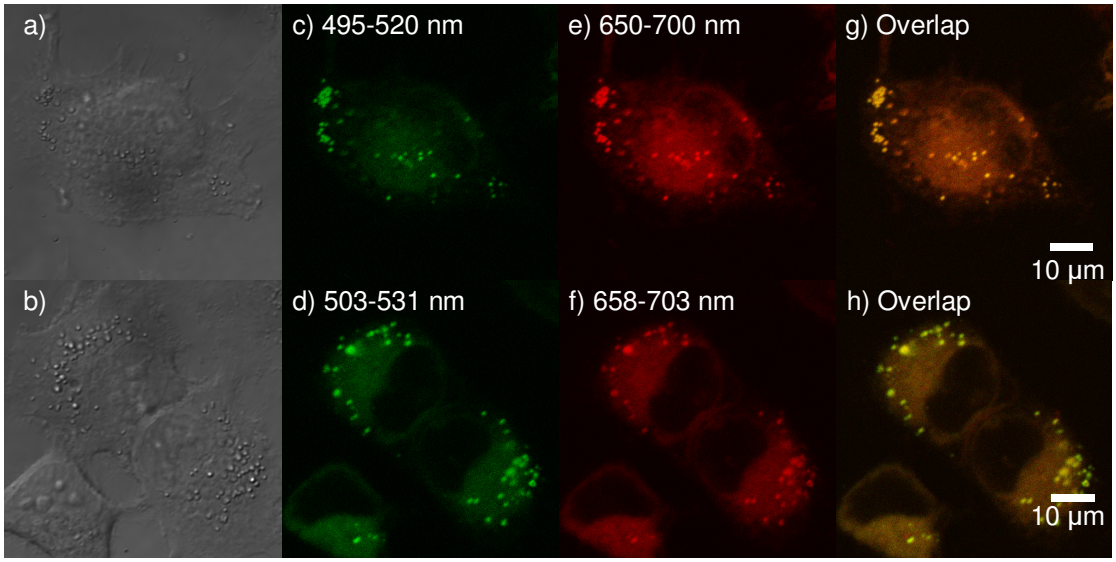

Figure 3.17 Transmission (a and b) and confocal fluorescence images (c-h) of live HeLa cells stained with BODIPY-C_{12} and Nile red. An excitation wavelength of 488 nm is used to acquire the images. The wavelength on the images denotes the detected emission wavelength, and the overlap of two channels (g, h). A pinhole size of 0.9 Airy units is used.

The intensity distribution of the trajectory A-B and C-D with two emission windows are shown in Figure 3.18. The emission wavelength of 503-531 nm denotes BODIPY-C_{12}, and 658-708 nm denotes Nile red. The fluorescence intensity between two dyes increases and decreases correspondingly. In other words, the distribution of Nile red and BODIPY-C_{12} appear in the same positions. This implies that the BODIPY-C_{12} and Nile red are in the same location within the optical resolution.

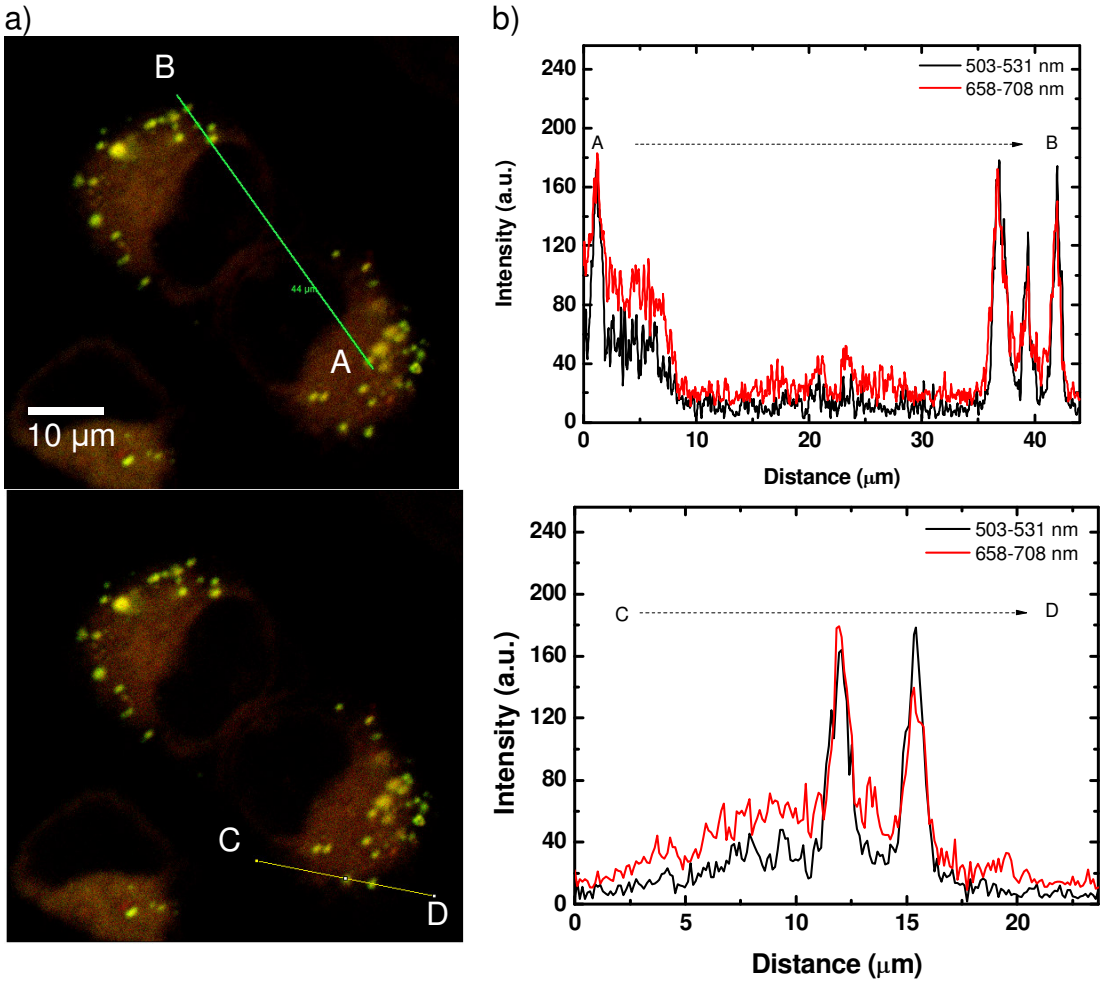

Figure 3.18 (a) Confocal fluorescence images of HeLa cells with Nile red and BODIPY-C_{12}. (b) The corresponding emission spectrum of (a). The intensity distributions of BODIPY-C_{12} (black curve) and Nile red (red curve) from A to B and from C to D in (a) are shown in (b).

In addition, we recorded a series of images to monitor the movement of BODIPY-C_{12} in HeLa cells, and the interval between two images is 1.6 second. The trajectory of a punctum in the white circle of Figure 3.19(a) is depicted in Figure 3.19(b). It seems that the movement of this punctum is along a certain pattern and also confined at some positions. It has been reported that the translational mobility of lipid droplets is fast moving or oscillating along microtubules and then stuck to the ER.[186] It provides another piece of evidence to show that the puncta are lipid droplets.

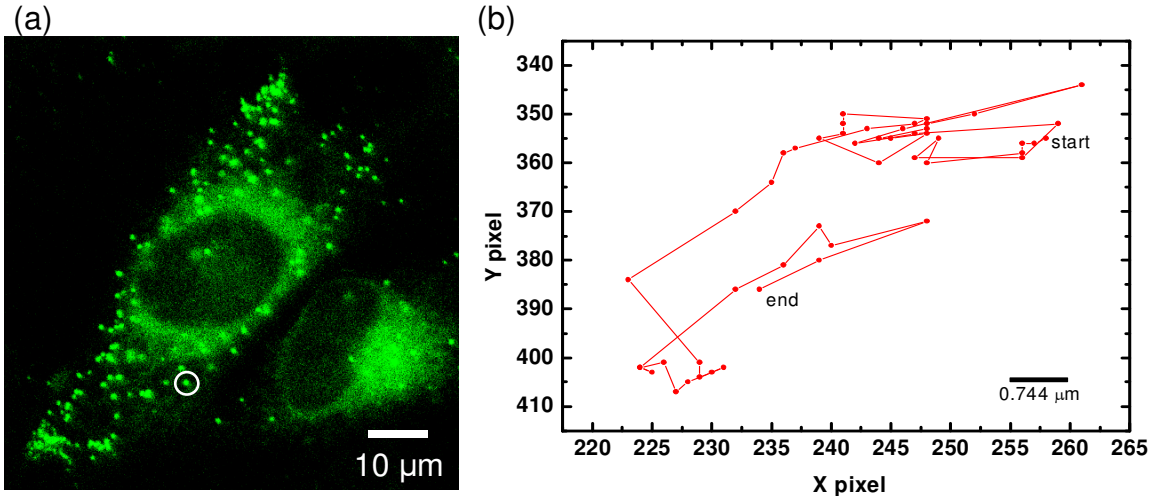

Figure 3.19 (a) Confocal fluorescence images of HeLa cells with BODIPY-C_{12}. (b) The trajectory of one punctum in the circle of (a).

The puncta are thus demonstrated to be as lipid droplets. Lipid droplets contain neutral lipids and perilipin family proteins.[187] Triacylglycerols (TAG), cholesterol esters (CE) and ergosterol esters are neutral lipids. It has been reported that the melting point for lipids esters varies with the chain lengths of fatty acid. The high viscosity environment at 37℃ could occur when lipid esters with high melting point exist, resulting in a decrease in the translational mobility of molecules on the lipid droplet surface.[188] Hence, the high viscosity is observed in lipid droplets from this experiment.

Each lipid droplet in a cell could contain different components and have different functions, such as storing lipids which are related to lipid metabolism or functioning as a protector for proteins.[187, 189] However, any correlation between the function of lipid droplets and its viscosity is still unknown.

The punctate locations of BODIPY-C_{12} were demonstrated to be lipid droplets. Apart from this, we also demonstrated that the location of networks of BODIPY-C_{12} in HeLa cells via the counterstaining experiment. The second counterstaining experiment used HeLa cells incubated with ER-RFP and BODIPY-C_{12}. The results are shown in Figure 3.20. The emission spectrum of

BODIPY-C_{12} is shown in black line of Figure 3.20(b) and the emission spectrum of ER-RFP in HeLa cells is 550-750 nm as shown in grey line of Figure 3.20(b). The emission spectrum in the region of interest (ROI) 5 is similar to that of HeLa cells stained with BODIPY-C_{12} only, and others ROIs are the combinations of BODIPY-C_{12} and RFP signals. The distribution of BODIPY-C_{12} is discovered by detecting the emission intensity of 495-525 nm, and the fluorescence wavelength of 550-600 nm is for detecting ER-RFP shown in Figure 3.20(c, d). The increase in fluorescence intensity for BODIPY-C_{12} and ER-RFP occurs in the same positions, which shows that BODIPY-C_{12} locates in the ER.

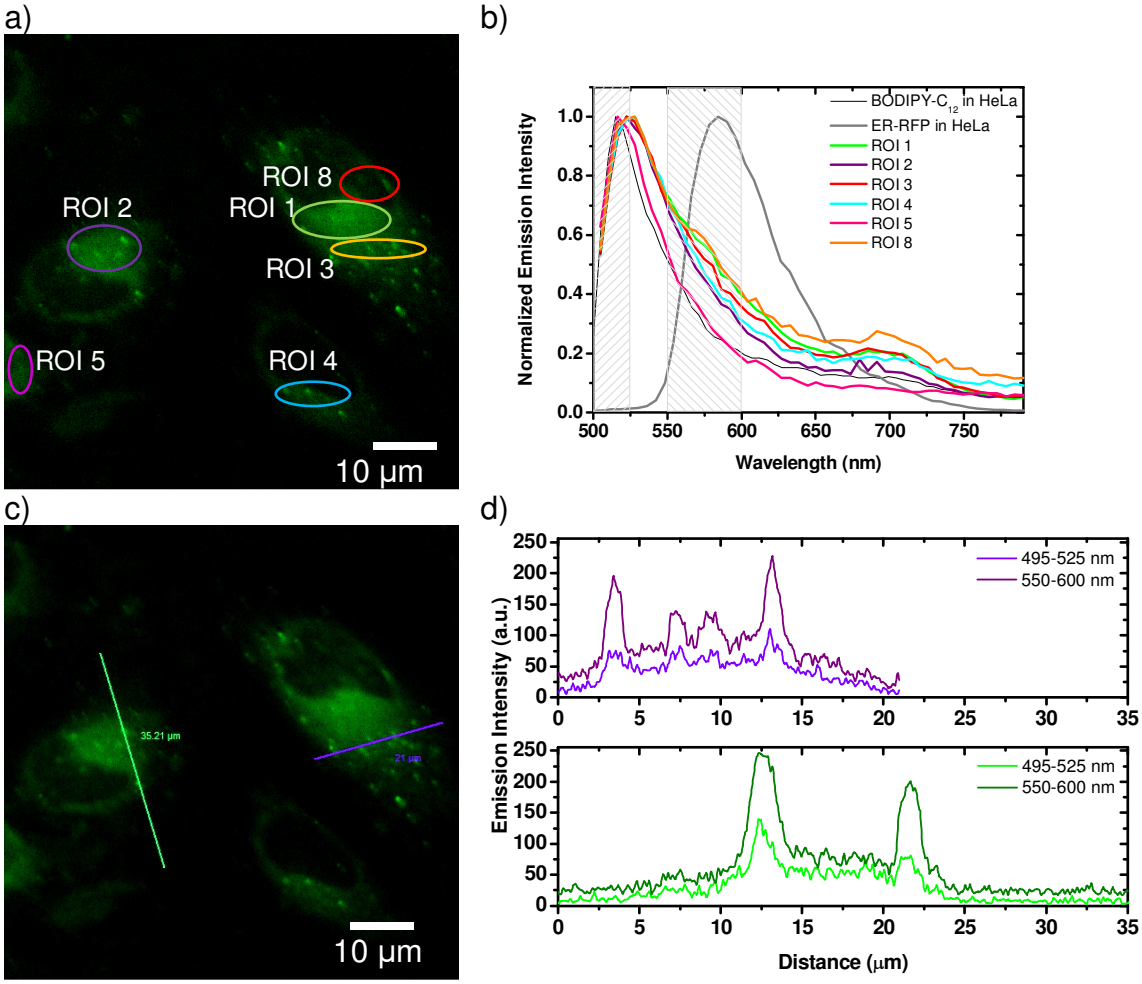

Figure 3.20 (a, c) Confocal fluorescence images of BODIPY-C_{12} and ER-RFP in HeLa cells at 37℃. (b) The emission spectra of ROIs (a). (c, d) The distribution histograms of BODIPY-C_{12} and ER-RFP in HeLa cells.

From the counterstaining experiments, it was found that the main locations of BODIPY-C_{12} in the HeLa cells are lipid droplets and endoplasmic reticulum within the optical resolution. A more thorough understanding of the BODIPY-C_{12} locations in cells could be obtained by using high resolution fluorescence microscopy, such as STORM. This would enable co-localisation studies with a higher spatial resolution or TEM.

3.4 Summary

The Stokes shift of BODIPY-C_{12} is as small as for some other BODIPY derivatives. From measurements of BODIPY-C_{12} in methanol/glycerol mixtures, it is concluded that the fluorescence quantum yield and the fluorescence lifetime of BODIPY-C_{12} vary with viscosity in agreement with the Förster-Hoffmann equation. The radiative rate constant of BODIPY-C_{12} increases by ~20% for the refractive index from 1.33 to 1.47. However, the non-radiative rate constant dominates influences on the fluorescence quantum yield. A relatively high fluorescence quantum yield and the existence of a single fluorescence lifetime on the nanosecond time scale demonstrate that BODIPY-C_{12} is an ideal viscosity sensor. It is better than DCVJ or CCVJ for lifetime measurements and in particular for FLIM.

BODIPY-C_{12} allows us to measure viscosity via FLIM in a relatively easy and straight-forward manner. The viscosity of whole cells can be measured in a few minutes via FLIM. The combination of FLIM and fluorescent molecular rotors provides a better method to measure viscosity than FCS and FRAP which only measure viscosity in a certain area.

The fluorescence lifetime image of BODIPY-C_{12} can also be used to discriminate the microviscosity within a heterogeneous environment, such as cells. It is better than intensity measurements because the concentration of

molecules does not influence the fluorescence lifetime results; in the intensity measurement case the concentration effect cannot be discriminated.

It has been demonstrated that the main locations of BODIPY-C_{12} in cells are the lipid droplets and endoplasmic reticulum, and the environments are thus more viscous than the fluid phase of cytoplasm.

Chapter 4

Viscosity Mapping by BODIPY-C_{12} via Polarization-resolved Fluorescence Techniques

4.1 Introduction

In general, the rotational diffusion of a fluorescent molecule can be measured via polarization-resolved fluorescence techniques. In this chapter, we present a novel mathematical framework based on the fact that for fluorescent molecular rotors, the steady-state anisotropy as given by the Perrin equation (eq. 1.26) is related to the viscosity via the Förster-Hoffmann equation (eq. 2.10) and Stokes-Einstein-Debye equation (eq. 2.28). Moreover, it is shown that the rotational correlation time of BODIPY-C_{12} in methanol/glycerol mixtures is a function of its fluorescence lifetime according to a modified Förster-Hoffmann equation (eq. 4.4). This is theoretically accounted for by combining the Stokes-Einstein-Debye equation (eq. 2.28) and the Förster-Hoffmann equation (eq. 2.9). The intracellular viscosity is measured via the steady-state and time-resolved fluorescence anisotropy. The steady-state anisotropy of BODIPY-C_{12} work presented here has been published.[129]

4.2 Steady-State Anisotropy of BODIPY-C_{12}

4.2.1 Experimental Section

We measured steady-state polarization-resolved images of fluorophore solutions using an inverted wide-field microscope (Nikon, TE-2000E). 250 µl of BODIPY-C_{12}, DCVJ (Invitrogen) and FITC (Sigma) in methanol/glycerol mixtures with a concentration of 3 µM were placed in individual wells of a 96-

well plate. A Hg lamp was used to excite the samples through a filter cube with an excitation filter at 475 nm, a chromatic reflector at 505 nm and a fluorescence filter at 515 nm and a 63x oil immersion objective (NA=1.4, Leica). The fluorescence signal passed through the same objective and a polarized image splitter (Optosplit II, Cairn) and the two orthogonally-polarized images were recorded simultaneously using a cooled dual mode electron-bombarded charge-coupled device (EBCCD) camera (Hamamatsu, C7190). The anisotropy images were produced through the following steps. The two orthogonally polarized images were aligned to match the corresponding pixels via the Cairn Image Splitter plug-in for ImageJ (see Figure 4. 1). Then, the two images were processed using eq. 1.17 with G=0.9 calculated based on eq. 1.27.

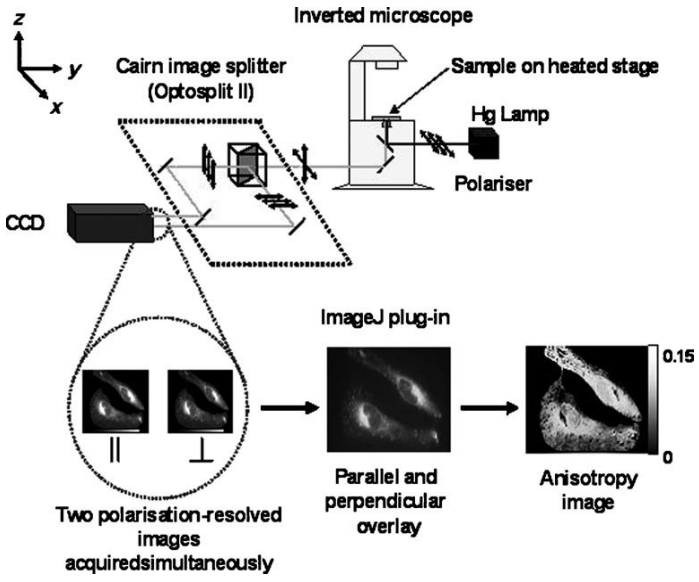

Figure 4. 1 Experimental setup and data processing steps for steady-state fluorescence anisotropy measurement.[129]

4.2.2 Steady-State Anisotropy of BODIPY-C_{12} in Methanol/Glycerol Mixtures

The anisotropy of a fluorescent molecular rotor is related to viscosity based on a modified equation of the Perrin (eq. 1.26) Stokes-Einstein-Debye equation (eq. 2.28) and Förster Hoffman equation (eq. 2.9).

$$r = \frac{r_0}{1 + B \cdot \eta^{\alpha-1}} \tag{4. 1}$$

Such that

$$B = \frac{z k_B T}{k_r V} \tag{4. 2}$$

where r is steady-state anisotropy, r_0 is the initial anisotropy, k_B is the Boltzmann constant, T is the absolute temperature, k_r is the radiative rate constant of the fluorophore, V is the hydrodynamic volume of the molecule, η is the viscosity of the solution and α and z are constants. The value of α is in the range 0.45-0.75 for fluorescent molecular rotors,[94, 99, 128] while $\alpha = 0$ is for rigid molecules where there is no influence of viscosity on quantum yield.

A simulation of eq. 4.1 is shown in Figure 4. 2. The value of r is approaching r_0 as the viscosity is increasing and is equal to r_0 at a certain viscosity which depends on the internal properties of molecules. Moreover, it indicates that there are different trends for fluorescent molecular rotors and rigid fluorescent molecules with the same radiative rate constant and molecular volume at the same temperature (black vs. blue lines and red vs. green lines). For rigid molecules with different B values (eq. 4.2), there is a limited region over which the viscosity can be measured. At low viscosities, r is close to zero and at high viscosities, r is close to r_0. The characteristic curve for rigid molecules shifts to a different viscosity region as shown in black and red lines of Figure 4. 2. The useful dynamic viscosity range is limited but can be changed by changing the fluorescence lifetime. In contrast, the dynamic range of viscosity for fluorescent molecular rotors can be much larger under the same B values as rigid fluorophores. The mathematical framework thus predicts an extended dynamic

range of viscosity that can be probed with steady-state anisotropy measurements with fluorescent molecular rotors

.

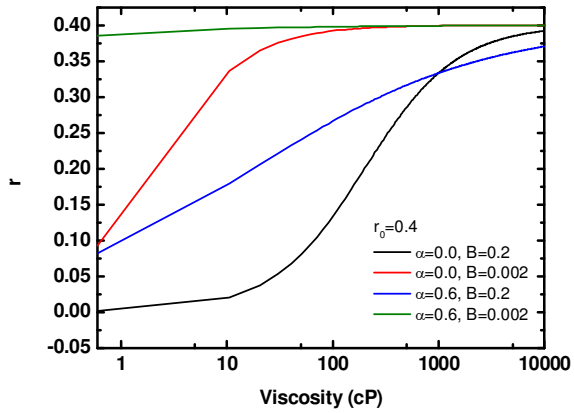

Figure 4. 2 Simulations of steady-state anisotropy versus viscosity according eq. 4.1 using Origin 8.0 software. Black and red lines represent rigid molecules with different B values (refer to eq. 4.2), and blue and green lines represent fluorescent molecular rotors with different B values.

We measured steady-state fluorescence anisotropy of 3 fluorescent molecules using the setup as shown in Figure 4. 1. There are two fluorescent molecular rotors, BODIPY-C_{12} and DCVJ, and one rigid molecule, FITC. The steady-state anisotropy of the three dyes versus viscosity is shown in Figure 4. 3. The triangle, square, and open circle points denote BODIPY-C_{12}, DCVJ and FITC, respectively. The three grey lines are simulated according to eq. 4.1, and overlap with the data points. The anisotropy value is from 0.26 to 0.33 for DCVJ in mixtures with the viscosity from 0.6 to 630 cP. The anisotropy curve for DCVJ is similar to the green curve in Figure 4. 2 indicating r_0 = 0.33 for DCVJ. In contrast, the anisotropy values are in the range 0.10-0.35 and 0.10-0.27 for FITC and BODIPY-C_{12}, respectively. It was observed that FITC and BODIPY-C_{12} in solutions with viscosity of 0.6-600 cP have a big dynamic range in anisotropy, as predicted by our model.

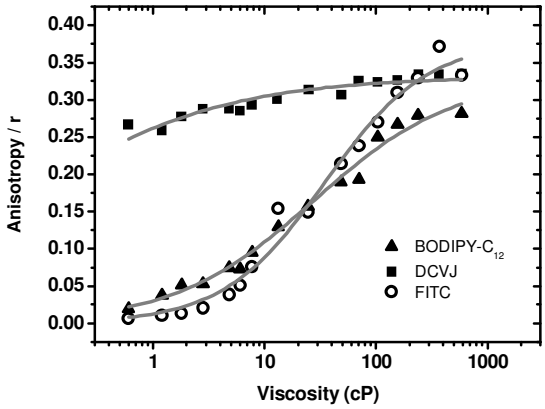

Figure 4. 3 The steady-state anisotropy versus the solvent viscosity for BODIPY-C_{12} (▲), DCVJ (■) and FITC (O).[129] The measurements were performed in an inverted microscope, a polarizing splitter and an EBCCD camera. The grey fitting curves are based on eq. 4.1 using Origin software.

A small dynamic range in anisotropy for DCVJ can be explained using eq. 1.26. The ratio of lifetime to rotational correlation time for DCVJ is much less than that for FITC and BODIPY-C_{12} at the same viscosity. For example, the lifetime of DCVJ in methanol has been measured to less than 10 ps,[129] and a rotational correlation time of 34 ps is calculated using eq. 2.28 and a radius of ~0.385 nm.[190, 191] The lifetime of BODIPY-C_{12} in methanol is 0.28 ns, and the rotational correlation time is estimated to be 17 ps using a radius of 0.3 nm which is described subsequently and by eq. 2.28. Due to the properties of the molecules, the anisotropy of DCVJ in methanol is very close to the initial anisotropy, which results in a small dynamic range in anisotropy at a viscosity range of 0.6-600 cP.

BODIPY-C_{12} and FITC have a large dynamic range. The anisotropy of BODIPY-C_{12} is relatively linear in proportion to the logarithmic viscosity over three orders of magnitude. The anisotropy of FITC remains the same in viscosity less than 1 cP and increases dramatically to reach a plateau at viscosity of approximately 600 cP. BODIPY-C_{12} is superior to FITC in viscosity < 10 cP, because it has a greater dynamic range in anisotropy and r is relatively linear proportion to the logarithmic viscosity. In the viscosity range of 10-100 cP, FITC offers a better dynamic range comparison to BODIPY-C_{12}. In general, BODIPY-C_{12} is the appropriate dye to measure viscosity of over several orders of magnitude,

especially since the anisotropy can be measured to an accuracy of >0.001 in cuvette-based system and 0.01 in a microscope.[192]

4.2.3 Steady-State Anisotropy of BODIPY-C_{12} in Cells

The anisotropy versus viscosity for BODIPY-C_{12} in methanol/glycerol mixtures has been addressed to be a calibration curve to measure viscosity. Here, we measured the steady-state fluorescence anisotropy of BODIPY-C_{12} in live HeLa cells. The anisotropy mapping of cells incubated with BODIPY-C_{12} is shown in Figure 4. 4. The colour spectrum from blue to red denotes changes in anisotropy from 0.030 to 0.175. The left hand side is fluorescence intensity image and the right hand side image is anisotropy image of BODIPY-C_{12} in punctate regions. The viscosity is calculated by using the calibration curve (see Figure 4. 3). It seems that the viscosity is up to 70 cP in the punctate regions.

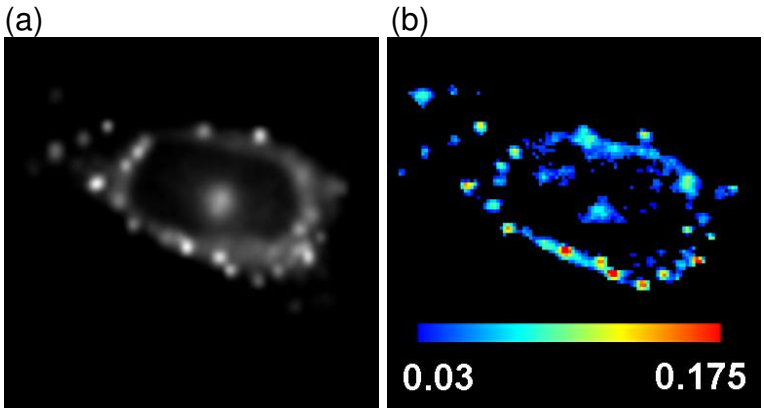

Figure 4. 4 (a) The intensity and (b) anisotropy mapping of BODIPY-C_{12} in HeLa cells. The fluorescence was excited at 475 nm, and detected at 515 nm. The corresponding viscosity is up to 70 cP for the punctate regions.

The advantage of steady-state polarization-resolved fluorescence measurements is that it is relatively rapid and easy. A cheaper light source, Hg lamp, is used to perform this experiment. The measurement can be made over a short acquisition time. The orthogonally polarized fluorescence is measured at the same time to avoid a monitoring the sample at different times for different polarizations. If the fluorescence of fluorescent molecules is bright, a high frame

rate CCD can be employed to monitor the fast dynamic change.[193] It has been shown that the viscosity of the environment of the fluorescent probe is related to anisotropy.[129, 130] However, steady-state anisotropy could not deal with hindered rotation. Thus, we use a time-resolved fluorescence anisotropy technique to measure viscosity of the environment and the rotation mobility of the indicator.

4.3 Polarization and Time-Resolved Fluorescence of BODIPY-C_{12} in Methanol/Glycerol Mixtures

4.3.1 Experimental Section

For the time-resolved polarization fluorescence measurement, the procedure is almost similar as the time-resolved fluorescence measurement mentioned in 3.2.1. The only difference is the way the fluorescence signal is measured. The fluorescence passed through a band-pass filter (Semrock), a polarizing cube beamsplitter (Edmund Optics), and the orthogonal polarized signals were collected using two hybrid PMT detectors, simultaneously. The electronic signal produced from detectors passes through a router to a PC, and fluorescence decays were constructed by a TCSPC card (Becker & Hickl, SPC-830) in a PC (see Figure 4. 5).

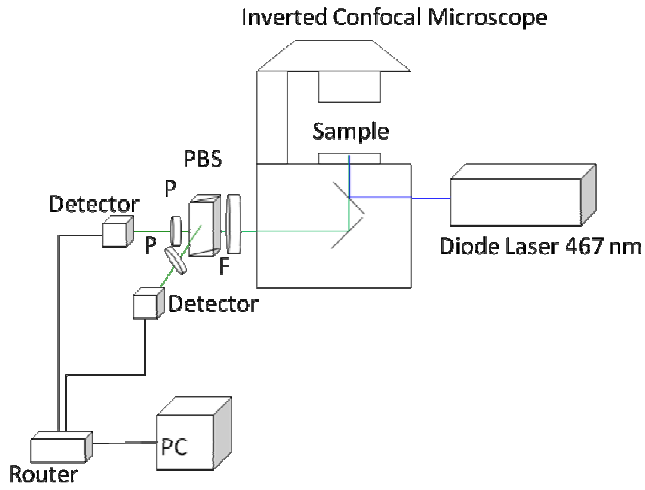

Figure 4. 5 Experimental setup for time-resolved fluorescence anisotropy imaging. PBS denotes polarization beamspilitter, F denotes filter, and P denotes polarizing filter.

4.3.2 Rotational Correlation Time of BODIPY-C_{12} in Methanol/Glycerol Mixtures

The rotational correlation time of BODIPY-C_{12} in mixture versus viscosity is shown in Figure 4. 6. The time-resolved fluorescence anisotropy results showing the rotational behaviour of BODIPY-C_{12} can be described using the Stokes-Einstein-Debye theory (eq. 2.28). A straight line is fitted through the origin with the gradient of $(3.47 \pm 0.04) \times 10^{-8}$ $m \cdot s^2 \cdot kg^{-1}$. The radius of the fluorophore was found to be 3 Å using the gradient of the fit and assuming a spherical of BODIPY-C_{12}.

The bond lengths of Pyrromethene 546 (PM546) (see Figure 5. 1(a) for the molecular structure) have been determined by X-ray diffraction[194] and density functional theory,[195] and the results show dihedral angles between two pyrrole rings. The radius of PM546 is estimated to be 4.4 Å assuming a flat PM546 and the bond length form the literatures. The radius of BODIPY-C_{12} is valid through the comparison with the similar molecule PM546. Hence, the radius of BODIPY-C_{12} from anisotropy measurement is reasonable. In addition, Figure 4. 6 is a

calibration to measure viscosity by associating it with the rotational correlation time of BODIPY-C_{12}.

From time-resolved fluorescence anisotropy decays (see Figure 4. 6(c-e)), lower values of r_0 were found in some solutions with low viscosity and a constant value of 0.20-0.23 was found in viscous solutions (viscosity >28 cP). In our setup for time-resolved fluorescence anisotropy measurements, we could not resolve the polarized fluorescence components correctly for fast rotating molecules, which results in a low observed value of r_0. A fast rotation of fluorophores that cannot be resolved correctly in the orthogonal polarization causes a lower anisotropy.

Moreover, a high NA microscope objective depolarizes the excitation and emission resulting in a z-axis polarized component. An estimation of r_0 under a high NA objective lens can be calculated using a relative method. A reference and an unknown sample are measured in a cuvette-based system and a microscope. The initial anisotropy of Rh123 is 0.37 and 0.29 for the measurement under the cuvette-based system and the confocal microscope with NA=1.2, respectively. The value of r_0 for Rh123 in cuvette system is consistent with the value reported in the literature.[196] The initial anisotropy of BODIPY-C_{12} is approximately 0.30 measured in the cuvette-based system. Hence, the initial anisotropy of 0.24 for BODIPY-C_{12} in the microscope using a NA=1.2 objective lens was estimated by relative ratio of r_0 obtained from the microscopy-based and the cuvette-based experiments. Rh123 is used to examine the depolarization effect of microscope, and the results are shown in the appendix.

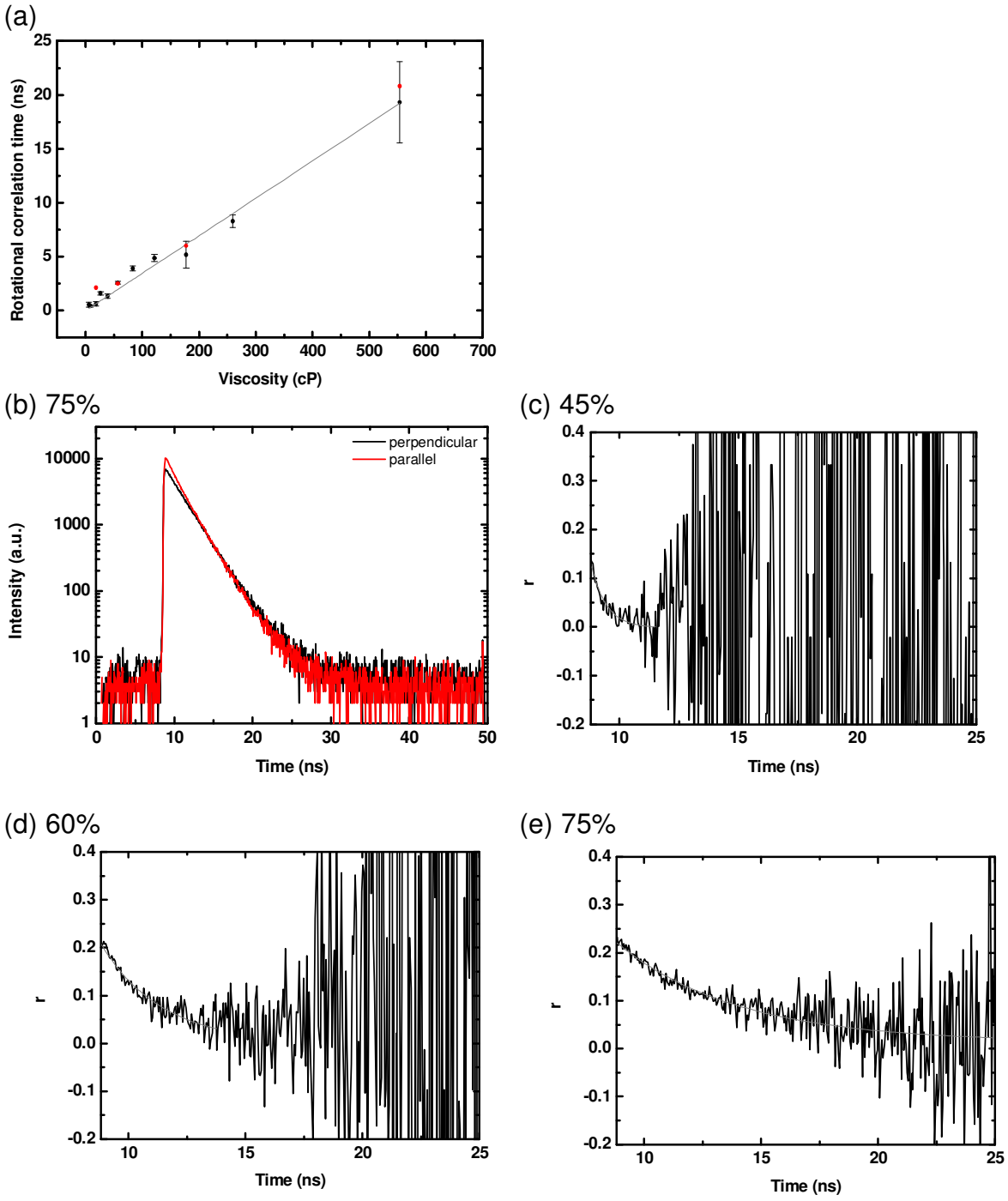

Figure 4. 6 (a) The rotational correlation time of BODIPY-C_{12} in mixtures of methanol/glycerol with different viscosity, including the results from this measurement (●) and other measurement (in section 4.4.3) (●). A straight grey line is used to fit black points according to eq. 2.28. (b) The polarized fluorescence decays of BODIPY-C_{12} in solution with 75% V/V glycerol. Parallel and perpendicular denote the polarization of the collecting fluorescence compared to the polarization direction of the incident light. The anisotropy decay for BODIPY-C_{12} in mixture with (c) 45%, (d) 60% and (e) 75% of glycerol.

4.3.3 Steady-State Anisotropy of BODIPY-C_{12} from Time-Resolved Fluorescence Measurements

The steady-state fluorescence anisotropy can also be calculated from the time-resolved fluorescence decay. The intensities of the two polarizations are the integrated areas under the fluorescence decay, and the anisotropy values can be calculated using eq. 1.17. The steady-state anisotropy values calculated from the time-resolved measurements for BODIPY-C_{12} in mixtures are shown in Table 4. 1.

Table 4. 1 The lifetime, rotational correlation time and anisotropy of BODIPY-C_{12} in methanol/glycerol mixtures.

Volume % of glycerol	Viscosity (cP) at 22℃	Lifetime (ns)	Rotational correlation time (ns)	Steady-state anisotropy
0	0.6	0.28	too short	0.0014
5	0.9	0.29	too short	
10	1.3	0.32	too short	0.0090
15	1.9	0.36	too short	
20	2.7	0.36	too short	0.0411
25	4.0	0.36	too short	0.0268
30	5.8	0.42	0.06	0.0382
35	8.5	0.46	0.43	0.0470
40	12.5	0.58		
45	18.2	0.50	0.63	0.0720
50	26.6	0.60	1.61	0.1187
55	38.9	0.67	2.16	0.1280
60	56.9	0.78	2.58	0.1362
65	83.1	1.00	3.91	0.1431
70	121.4	1.37	4.87	0.1511
75	177.4	1.84	5.17	0.1580
80	259.3	1.93	6.81	0.1642
85	378.8	2.45		
90	553.6	2.90	19.33	0.1825

A relationship between anisotropy and viscosity for BODIPY-C_{12} in methanol/glycerol mixtures is shown in Figure 4. 7(a). A comparison of two sets of data is shown in Figure 4. 7(b), the different NA of objective lenses results in

different anisotropy values at the same viscosity. The anisotropy measurement was carried out using a NA=0.75 objective lens for red points (see Figure 4. 7(b)) which had a higher anisotropy values compared to the measurement using a NA=1.2 objective lens (black points).

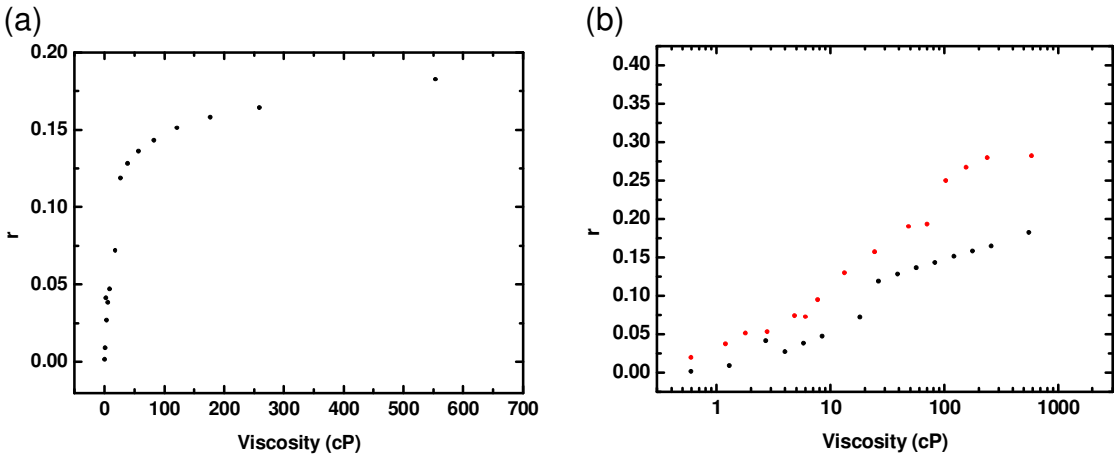

Figure 4. 7 A plot of steady-state anisotropy of BODIPY-C_{12} versus viscosity with a (a) linear viscosity scale and (b) logarithmic viscosity scale. (b) A comparison of anisotropy vs. viscosity between two sets of data from time-resolved anisotropy measurement (●, Figure 4. 6) and polarization-resolved fluorescence measurement (●, Figure 4. 3).

The initial anisotropy can be calculated using eq. 4.3 which is a rearrangement equation for eq. 4.1. The intercept of a plot of $1/r$ versus $\eta^{\alpha-1}$ is the inverse of r_0.

$$\frac{1}{r} = \frac{1}{r_0} + \frac{zk_BT}{r_0 k_r V}\eta^{\alpha-1} \qquad (4.3)$$

where the parameters are the same as eq. 4.1.

According eq. 4.3, a plot of r^{-1} vs. $\eta^{\alpha-1}$ for FITC is shown in Figure 4. 8. In this case, α is zero and $z = \Phi$ because FITC is a rigid molecule. The initial anisotropy can be calculated using the intercept of the plot. The intercept for viscosity from 0.6 to 600 cP is 4.6 ± 2.1 which correspond to r_0 of 0.28 ± 0.12, as shown in Figure 4. 8(a). If we fit the data points for viscosities above 25 cP, then the intercept is 2.65 ± 0.07 with the corresponding r_0 of 0.38 ± 0.01 (Figure 4. 8(b)). This is in agreement with the literature value for FITC. The slope is 0.100 ± 0.004 for the plot of Figure 4. 8(b) which yields the radius of 0.47 nm.

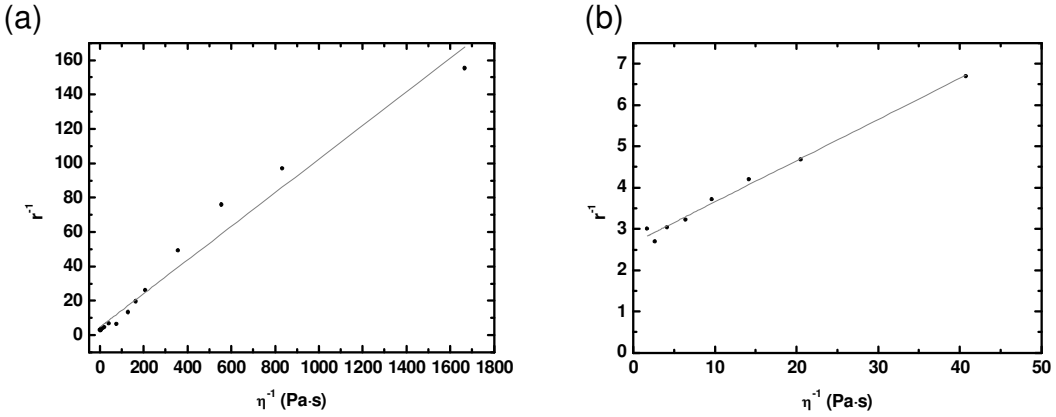

Figure 4. 8 A plot of r^{-1} versus η^{-1} for FITC (A rearrangement of date for FITC from Figure 4. 1) in viscosity between (a) 0.6-600 cP and (b) 25-600 cP. The grey lines are the best fit to the data (Adj. R-Square = 0.973 (a) and 0.989 (b)). The value of r_0 can be estimated using eq. 4.3.

Rearranging the data of Figure 4. 3, a plot for DCVJ according to eq. 4.3 is depicted in Figure 4. 9. There is a straight line on the plot of r^{-1} versus $\eta^{\alpha-1}$ according to eq. 4.3, and r_0 can be calculated from the intercept. A fit of straight line yields an intercept of 3.05 ± 0.04, and the initial anisotropy was calculated to be 0.33.

A straight line is used to fit the data with viscosities above 4.8 cP yielding an intercept of 2.95 ± 0.02 and a gradient of 0.040 ± 0.003, as shown in Figure 4. 9(b). The value of r_0 is calculated to be 0.34, and it is similar to that obtained from Figure 4. 9(a).

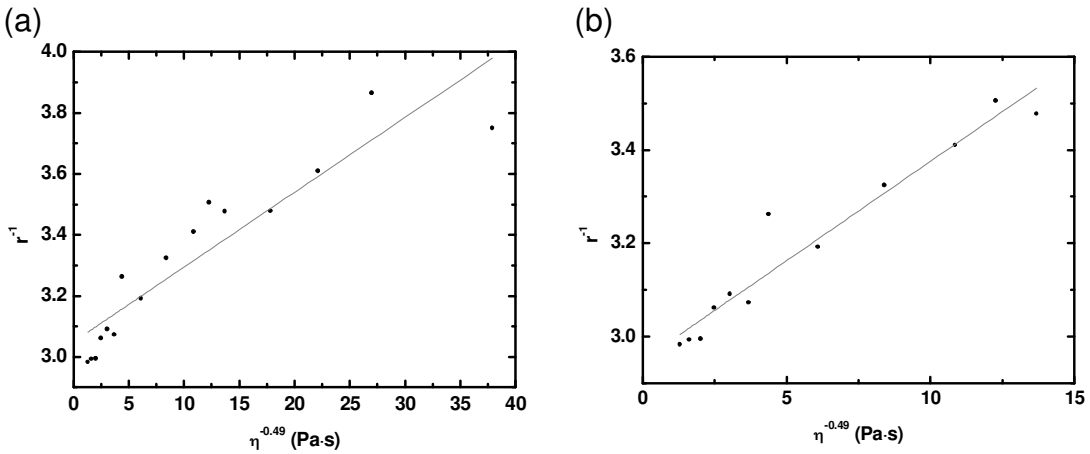

Figure 4. 9 A plot of r^{-1} versus $\eta^{-0.49}$ for DCVJ (a rearrangement of date for FITC from Figure 4. 3) in viscosity between (a) 0.6-600 cP and (b) 4.8-600 cP. The value of r_0 can be estimated using eq. 4.3. (a) The grey line with a gradient of 0.024 ± 0.003 and an intercept of 3.05 ± 0.04 (Adj. R-Square = 0.845). (b) The straight line with a gradient of 0.040 ± 0.003 and an intercept of 2.95 ± 0.02 (Adj. R-Square = 0.934).

According to eq. 4.3, it appears a straight line on the plot of r^{-1} versus $\eta^{\alpha-1}$, and the inverse of intercept is the initial anisotropy. A plot of r^{-1} versus $\eta^{\alpha-1}$ for BODIPY-C_{12} from two data sets is shown in Figure 4.10.

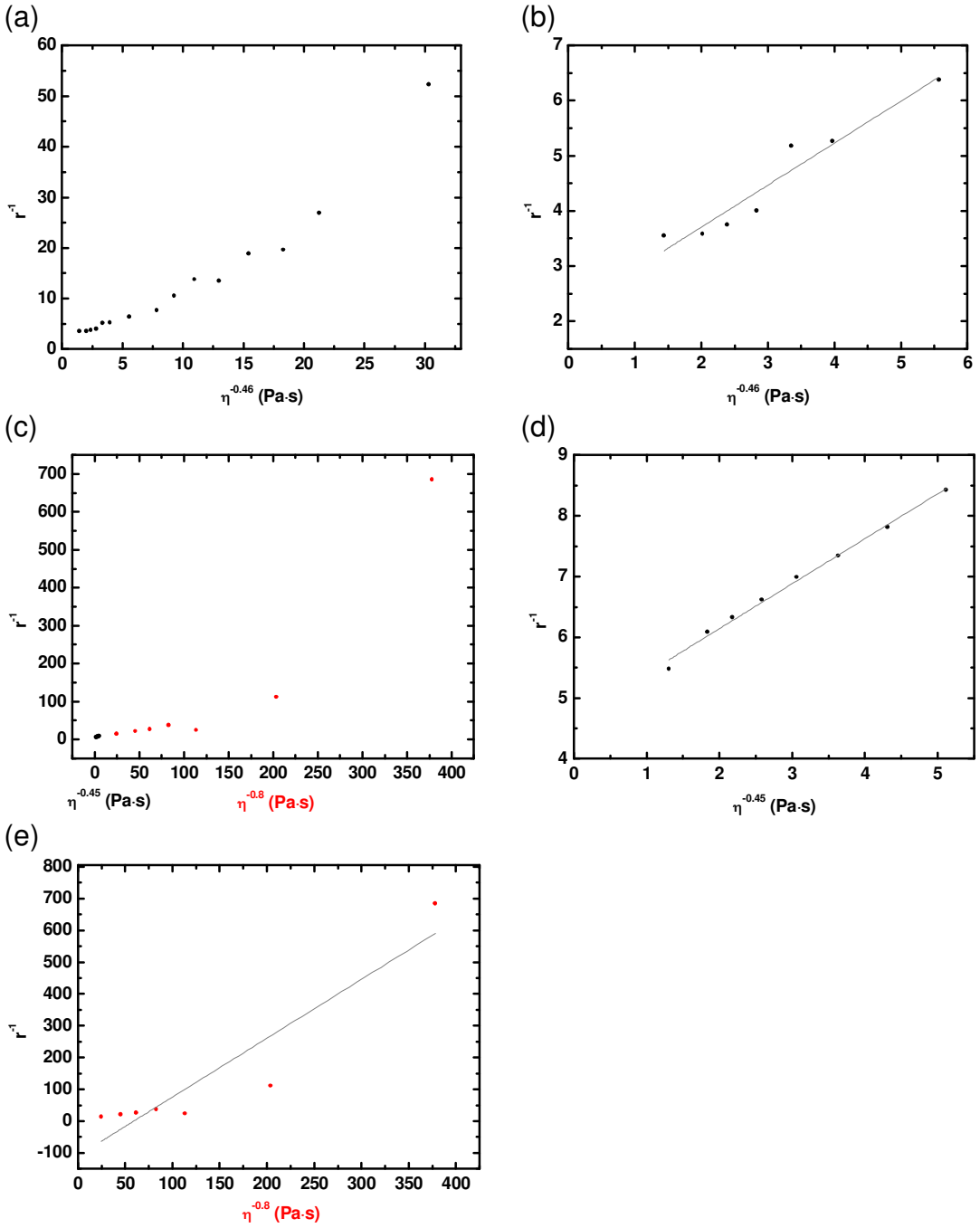

Figure 4.10 A plot of r^{-1} versus $\eta^{\alpha-1}$ for BODIPY-C_{12} in methanol/glycerol mixtures. The value of r_0 can be estimated using eq. 4.3. (a, b) The data is from Figure 4. 3. (c-e) The data set is from Figure 4. 7(a), and there are two α values, which is 0.2 in low viscosities, and 0.55 in high viscosities. (c) has 2-axis labels. The red points denote the data in low viscosities. The black points denote in high viscosities. The grey straight lines are the best fit to the data. (Adj. R-Square = 0.921 (a), 0.993 (d) and 0.842 (e))

The intercept was found to be 2.18 ± 0.30, and r_0 was in a region of 0.47 ± 0.06 for the steady-state fluorescence anisotropy measurement using a NA=0.75 objective lens (Figure 4.10(a, b)). In general, the maximum of r is r_0, and r_0 is 0.4 for fluorophores in isotropic solutions using one-photon excitation. Moreover, a high NA objective lens results in a decrease in anisotropy.

The second data set is from the time-resolved fluorescence anisotropy measurement using a NA=1.2 objective lens (in section 4.3.2). There are two α for BODIPY-C_{12} among the viscosity form 0.6 cP to 600 cP according to eq. 2.10 (see Figure 3. 9). Therefore, two relationships between r^{-1} vs. $\eta^{\alpha-1}$ for BODIPY-C_{12} are shown in Figure 4.10(c). The value of α is 0.2 in low viscosities, and 0.55 in high viscosities. For low viscosities, a negative intercept was found and yielded a wrong value of r_0, as shown in Figure 4.10(e). The value of r_0 is the intrinsic property of a fluorophore, and it would not change due to different solvent. If the setup could not be recorded the correct polarized fluorescence components due to a fast rotation, then the value of r is wrong. Hence, it could not be used to extract r_0 precisely.

In contrast, an intercept of 4.66 ± 0.07 is found in high viscosities ($\alpha = 0.55$), and r_0 is calculated to be 0.22. Furthermore, the value of r_0 and the constant of eq. 4.3 is in agreement with the results from time-resolved fluorescence anisotropy measurements (section 4.3.2) and fluorescence lifetime versus viscosity (section 3.2.5).

There is a requirement for the relation between anisotropy and viscosity of a freely rotation fluorescent molecule (eq. 4.3), which is that the orthogonally

polarized fluorescence decays should be precisely collected. In other words, the correct r_0 can be observed on time-resolved fluorescence decay.

4.3.4 Combination of Lifetime and Rotational Correlation Time of BODIPY-C_{12} in Methanol/Glycerol Mixtures

It has been demonstrated that the fluorescence lifetime of BODIPY-C_{12} is a function of the viscosity according to the Förster-Hoffmann equation (eq. 2.10). The rotational correlation time increases linearly with the viscosity based on the Stokes-Einstein-Debye equation (eq. 2.28). Hence, a combination of eq. 2.10 and eq. 2.28 shows that the fluorescence lifetime of the BODIPY-C_{12} fluorescent molecular rotor is a function of the rotational correlation time, which is

$$\log \tau_f = \alpha \log \theta + \alpha \log \frac{k_B T}{V} + \log \frac{z}{k_r} \qquad (4.\ 4)$$

On the basis of this theory (eq. 4.4), a plot of logarithmic fluorescence lifetime versus logarithmic rotational correlation time is predicted to be linear. Such a plot is independent of η, and the gradient is the same as the gradient of the plot for fluorescence lifetime vs. viscosity both in logarithmic scales (see Figure 3. 9).

The fluorescence lifetime versus the rotational correlation time of BODIPY-C_{12} is plotted with double logarithmic scales in Figure 4.11. According to eq. 4.4, a straight line is able to fit the data of the plot (Figure 4.11). The gradient of the straight line (see grey line in Figure 4.11) is 0.53 ± 0.04 with the intercept of -0.23 ± 0.03 for the results from Table 4. 1 and it is in good agreement with the previous results in section 3.2.5. The blue line describes the data points from the literature,[128] and the gradient is 0.53 ± 0.09 with an intercept of -0.02 ± 0.07.

The green line is used to describe the all data points based on eq. 4.4, and the slope is 0.56 ± 0.06 with an intercept of -0.16 ± 0.04. It was found that the slopes for all fitting results are consistent, but with a different intercept. The reason for a different intercept between two sets of data is a different quantum yield. The fluorescence quantum yield of BODIPY-C_{12} has been reported[100] and it is higher than that in the measurements in section 3.2.4, resulting in a different z constant of eq. 2.9 and therefore changes the intercept according to eq. 4.4. Moreover, the radiative rate constant calculation is based on the fluorescence quantum yield and fluorescence lifetime, and the radiative rate constant is different for the two sets of data. The radius of the molecule is the same for these two sets of measurements, so the different intercept according to eq. 4.4 results from a different z / k_r.

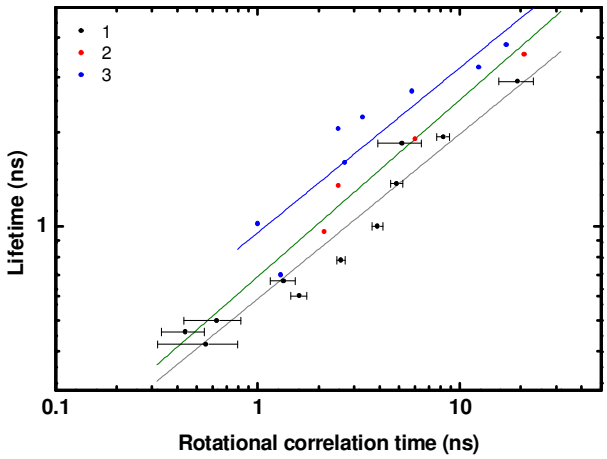

Figure 4.11 The relationship between fluorescence lifetime and rotational correlation time of BODIPY-C_{12} in methanol/glycerol mixtures. (1) denotes the data from Table 4. 1, (2) denotes the data from Figure 4.14 and (3) denotes the results from the literature.[128] A straight line (grey) is used to fit the data (1) according to eq. 4.4, the blue line is for the data (3) and the green line is for all data points (1-3).

A set of fluorescein in NaOH/glycerol mixtures with different viscosities was prepared to study the relationship between lifetime and rotational correlation time for a rigid molecule. The fluorescence lifetime versus rotational correlation time of fluorescein is illustrated in Figure 4. 12, which shows a decrease in the fluorescence lifetime from 3.7 to 3.2 ns. This can be explained using eq. 1.2 and

eq. 2.11 which reports that $\tau_f^{-1} \propto n^2$, assuming the same fluorescence quantum yield for all mixtures. The refractive index of the mixtures is in the region of 1.409-1.474. An increasing refractive index results in a decreasing lifetime. To sum up, the relationship between fluorescence lifetime and rotational correlation time shows a completely different trend for rigid molecules and fluorescent molecular rotors.

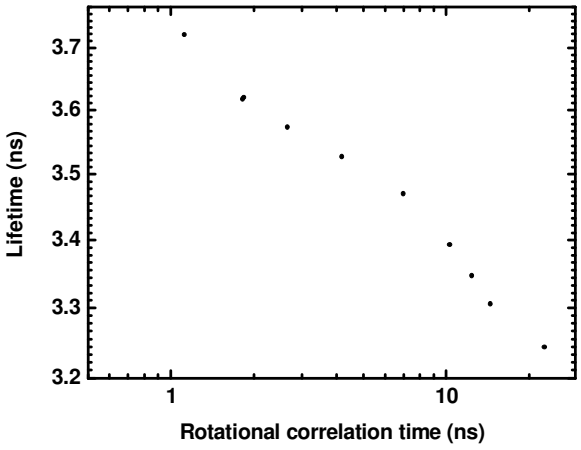

Figure 4. 12 The fluorescence lifetime versus rotational correlation time of fluorescein in different ratios of 0.1M NaOH/glycerol. This is a rigid fluorescent molecule, not a fluorescent molecular rotor.

4.4 Time-Resolved Polarization Fluorescence of BODIPY-C_{12} in cells

4.4.1 Experimental Section

HeLa cells were cultured in DMEM with 10% FBS, 1% 1x non essential amino acid, 1 mM sodium-pyruvate and 0.1 % penicillin/streptomycin on a 75 cm^2 culture flask (Greiner) in an incubator at 37℃ in a 95% air/5% CO_2. The cells were transferred to a 6-well glass bottom plate (WaferGen smartslide-6^{TM} micro-incubator) and incubated for one night. The medium was replaced with OptiMEM prior to staining dye and imaging.

For staining, a volume of 20 µl of BODIPY-C_{12} (2.65 mM) was added into a well of a micro-incubator and slightly shaken, then placed into an incubator for 30 minutes. The medium was removed and the cells were washed with clear DMEM five times. Finally, a well of the micro-incubator was filled by DMEM at 37℃ with 5% CO_2 atmosphere and was placed on the stage of the confocal fluorescence microscope to carry out time-resolved fluorescence anisotropy experiments. The imaging procedure is same as in section 4.3.1.

4.4.2 Rotational Correlation Time of BODIPY-C_{12} in Cells

The tr-FAIM measurements were implemented at 37℃ and 5% CO_2 to keep the cells physiologically alive. An exposure time for this experiment did not exceed more than 15 minutes. However, the number of photons in a single pixel is still not enough to have a good statistical analysis of time-resolved fluorescence anisotropy decay, even using a long exposure time. The accumulation time could not be too long; otherwise the cells die or change the morphology. Hence, pixel binning is used to process the time-resolved fluorescence anisotropy data.

The fluorescence decays with two orthogonal polarizations which are in parallel and perpendicular directions with respect to the incident light are recorded. We used TRI2 software to produce the fluorescence anisotropy decays. The fluorescence intensity image of BODIPY-C_{12} in HeLa cells are shown in Figure 4.13(a). The fluorescence decays and the corresponding fluorescence anisotropy decays of lipid droplets and the regions outside lipid droplets are illustrated in Figure 4.13(b-e). Combination of fluorescence decays using the denominator of eq. 1.18 leads the fluorescence decay of a fluorophore. The fluorescence intensity for both polarizations is over 10,000 counts in the peak, and therefore it should have a good statistical accuracy. A bi-exponential function was used to fit the fluorescence decays (Figure 4.13), the lifetimes for lipid droplets were found to be 1.26 ns and 3.77 ns; 1.4 ns and 3.79 ns for the regions outside lipid droplets.

For the analysis of time-resolved fluorescence anisotropy decays, a monoexponential decay function was not able to yield a good fit. The anisotropy decays of BODIPY-C_{12} in two different regions show a “dip-and-rise” curve (see Figure 4.13(d-e)). Accordingly, we have to use other models to describe the anisotropy decay which is called associated anisotropy.[1] This “dip-and-rise” phenomenon has been reported using different fluorescent molecules applied in cells.[123, 197-201] It consists of two distinct lifetimes and two distinct rotational correlation times in a system which form a “dip-and-rise” anisotropy decay. Here, some models for fitting associated anisotropy are considered and the mathematics formulae are listed below.[202]

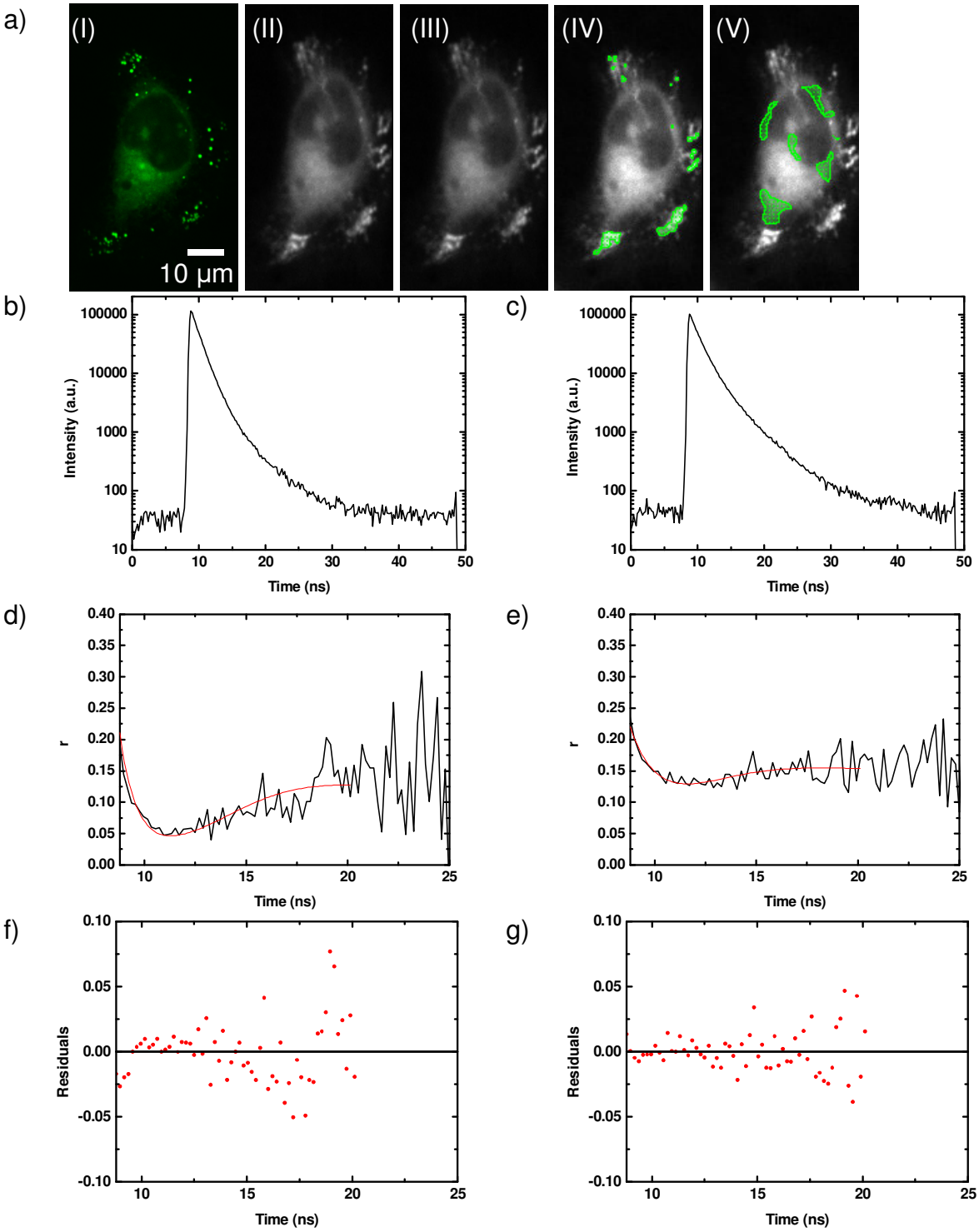

Figure 4.13 (a) The fluorescence intensity image of HeLa cells stained with BODIPY-C_{12}. (a-I), (a-II) and (a-III) denote total intensity, intensity in perpendicular direction and intensity in parallel direction to the incident light, respectively. (b) The intensity decay of BODIPY-C_{12} in puncta (green mask of a-IV), and (d) the corresponding time-resolved anisotropy decay with (f) the residuals. (c) The intensity decay and (e) time-resolved anisotropy decay with (g) the residuals of BODIPY-C_{12} in the regions outside puncta (green mask of a-V).

The time-resolved fluorescence anisotropy decay, $r(t)$, for the unrestricted isotropic rotations of fluorophores which have two lifetimes in a heterogeneous environment is[202]

$$r(t) = \frac{A_1 e^{-(t-t_0)/\tau_1} \cdot r_{01} e^{-(t-t_0)/\theta_1} + A_2 e^{-(t-t_0)/\tau_2} \cdot r_{02} e^{-(t-t_0)/\theta_2}}{A_1 e^{-(t-t_0)/\tau_1} + A_2 e^{-(t-t_0)/\tau_2}} \quad (4.5)$$

where τ is the fluorescence lifetime, r_0 is the initial anisotropy, θ is the rotational correlation time of the fluorophore, and A is the amplitude of the fluorescence lifetime. The subscripts 1 and 2 refer to component 1 and component 2. When the dye has a longer lifetime, a greater rotational correlation time and less population related to the other one, the dip-and-rise curve is observed.

In another case, a different type of associated anisotropy can occur. The fluorophores have two lifetimes in a heterogeneous environment. One fluorophore rotates freely, and the other is bound to a big object which rotates. The rotational correlation time of the object is of the same order of the lifetime, and the anisotropy decay is given by

$$r(t) = \frac{A_1 e^{-(t-t_0)/\tau_1} \cdot r_{01} e^{-(t-t_0)/\theta_1} + A_2 e^{-(t-t_0)/\tau_2} \cdot r_{02}[b_2 e^{-(t-t_0)/\theta_2} + (1-b_2)] e^{-(t-t_0)/\theta_p}}{A_1 e^{-(t-t_0)/\tau_1} + A_2 e^{-(t-t_0)/\tau_2}} \quad (4.6)$$

where b is the limiting anisotropy, θ_p is the rotational correlation time of the object and other parameters are the same as that in eq. 4.5.

Here is the other case which results in a dip-and-rise curve of the time-resolved fluorescence anisotropy decay. The following formula is used to describe more complex systems. The fluorophore with a hindered rotation has two lifetimes in a heterogeneous environment. In addition, the fluorophores attached to a particle rotate together. If the particle has a significant size, the last exponential term in the numerator becomes one. Consequently, the rotational particle cannot be observed in the fluorescence decay. If the values of θ_p and τ_2 are in the same order, the signal from the rotation of a particle would contribute to the anisotropy decay. The time-resolved fluorescence anisotropy is then[202]

$$r(t) = \frac{\{A_1 e^{-(t-t_0)/\tau_1} \cdot r_{01}[b_1 e^{-(t-t_0)/\theta_1} + (1-b_1)] + A_2 e^{-(t-t_0)/\tau_2} \cdot r_{02}[b_2 e^{-(t-t_0)/\theta_2} + (1-b_2)]\} e^{-(t-t_0)/\theta_p}}{A_1 e^{-(t-t_0)/\tau_1} + A_2 e^{-(t-t_0)/\tau_2}} \quad (4.7)$$

where the parameters are the same in eq. 4.6. For example, associated anisotropy occurs in the situation where the rotational correlation time is the same for all dyes but there are more dyes with a shorter fluorescence lifetime and a greater limiting anisotropy and fewer dyes with a longer fluorescence lifetime and a lower limiting anisotropy.

In order to get the rotational mobility of dye in cells, the values of the initial anisotropy, fluorescence lifetimes and relative proportion of two lifetimes were fed into these equations (eq. 4.5-4.7). It was found that the errors for unknown parameters are too big. It has been reported and discussed in section 4.3.4 that the fluorescence lifetime of BODIPY-C_{12} is related to the rotational correlation time according to eq. 2.10 and eq. 2.28. Hence, the ratio of two rotational correlation times was also fed into the equation, and it can be correlated using eq. 4.8.

$$\frac{\tau_1}{\tau_2} = (\frac{\theta_1}{\theta_2})^{\alpha} \quad (4.8)$$

where τ , θ are fluorescence lifetime and rotational correlation time of fluorophores with the subscripts 1 and 2 referring to the components from the shorter lifetime and the longer lifetime, respectively. The value of α is the same as eq. 2.10.

The results show that eq. 4.6 for BODIPY-C_{12} in lipid droplets of this cell (see Figure 4.13(a, IV)) leads to the better description of the dip-and-rise behaviour. In Figure 4.13, it was found that the rotational correlation time of BODIPY-C_{12} in lipid droplets is 1.03 ns for the shorter lifetime with a free rotation. The rotational correlation time is 7.55 ± 0.38 ns, and the limiting anisotropy is 0.11 ± 0.01 for the longer lifetime of BODIPY-C_{12}.

For the regions outside lipid droplets, the best fit model to describe the decay is eq. 4.7. The rotational correlation time of the shorter lifetime component is 1.17 ns, and the limiting anisotropy is 0.06 ± 0.02. The second restricted rotation molecules with the longer lifetime have a rotational correlation time of 7.17 ± 0.85 ns, and the limiting anisotropy is 0.14 ± 0.01. The viscosities were converted using the calibration (Table 4. 1). The viscosities in lipid droplets were found to be 30 cP and 218 cP. Furthermore, the viscosities for the regions outside the lipid droplets are 34 cP and 207 cP.

We use the models (eqs. 4.5-4.7) to fit some time-resolved fluorescence anisotropy decays of BODIPY-C_{12} in cells. There are two lifetimes and two rotational correlation times in lipid droplets and in the regions outside droplets. In addition, there are more BODIPY-C_{12} fluorophores with a shorter fluorescence lifetime and fewer BODIPY-C12 fluorophores with a longer fluorescence lifetime in both regions.

4.4.3 BODIPY-C_{12} in Methanol/Glycerol Mixtures in a Multiwell plate

In order to understand this effect, a model system consisting of BODIPY-C_{12} in homogeneous solutions of different viscosities in a multiwell plate. To compare the anisotropy decay of the fluorescent molecular rotor in cells and solutions, the fluorescence lifetime in solutions similar to that in cells are used to carry out experiments. BODIPY-C_{12} in the mixtures of glycerol/methanol with glycerol volume percentage of 45%, 60%, 75% and 90% were individually dropped into four separate wells of a 1536-well glass-bottomed plate (Greiner), individually. The time-resolved fluorescence anisotropy of the four solutions is measured simultaneously and shown in Figure 4.14, with the intensity images illustrated in Figure 4.14(a). The number on Figure 4.14(a) denotes the volume fraction of glycerol of methanol/glycerol mixtures. From this measurement, the fluorescence lifetime and the rotational correlation time of BODIPY-C_{12} can be measured. The fluorescence decays calculated using the denominator of eq. 1.18 are shown in Figure 4.14(b), and the fluorescence lifetimes are 0.99 ± 0.12, 1.37 ± 0.12, 1.92 ± 0.13 and 3.57 ± 0.02 ns for the mixtures contained glycerol of 45%, 60%, 75% and 90%, respectively.

The molecules in each well rotate freely in the solutions, and thus the anisotropy decay can be fitted by a monoexponential decay function with $r_\infty = 0$. The anisotropy decays are shown in Figure 4.14(c). It was found that the rotational correlation times are 2.13 ± 0.70, 2.51 ± 1.19, 6.00 ± 2.59 and 20.82 ± 3.16 ns for BODIPY-C_{12} in mixtures with glycerol volume fraction of 45%, 60%, 75% and 90%, respectively.

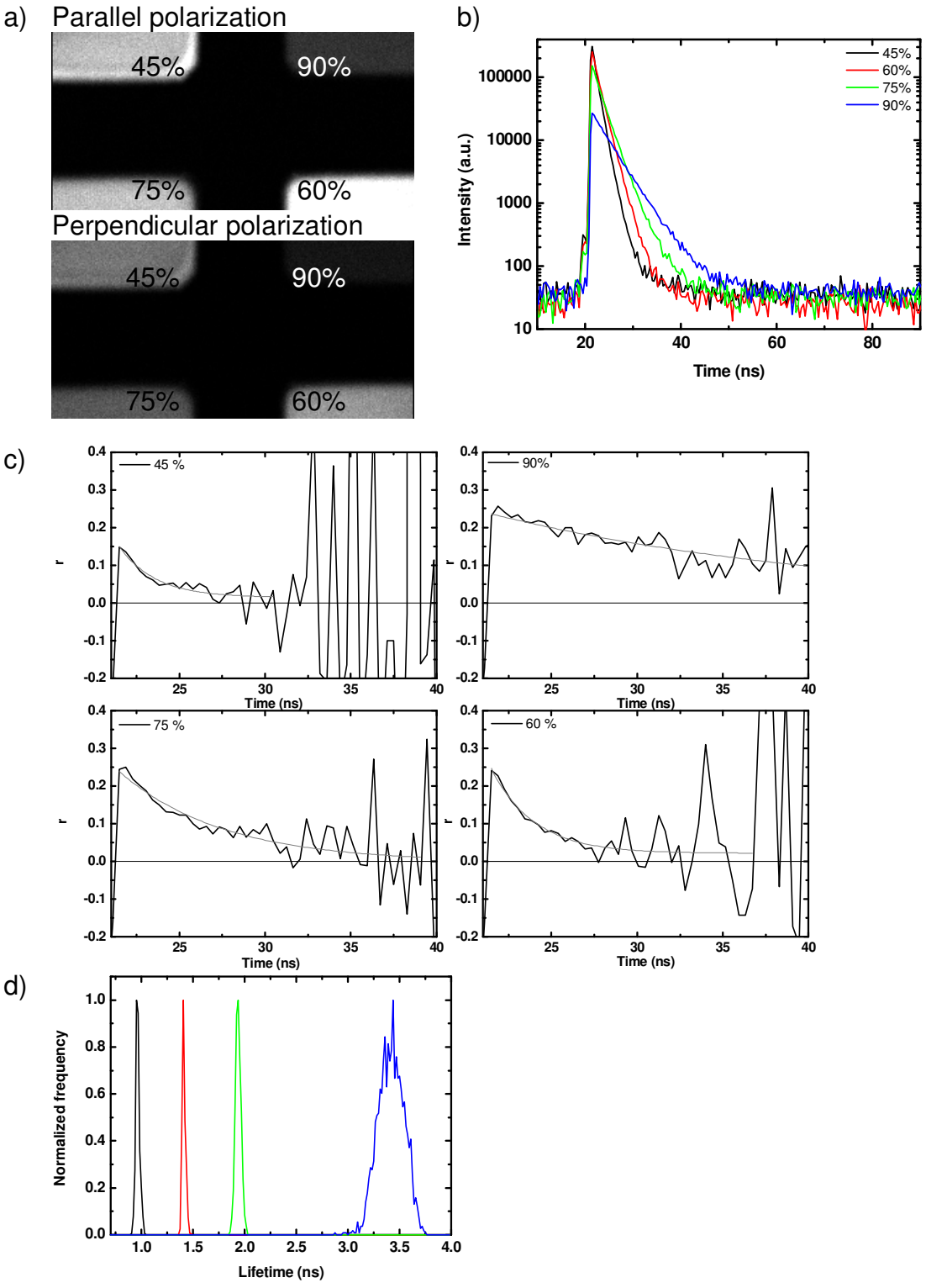

Figure 4.14 (a) The two orthogonal polarized fluorescence intensity images, (b) fluorescence decays and (c) time-resolved fluorescence anisotropy decays of BODIPY-C_{12} in four mixtures with different ratio of glycerol/methanol (45%, 60%, 75% and 90% of glycerol). (d) The lifetime histogram of 4 wells individually, black denotes 45%, red denotes 60%, green denotes 75% and blue denotes 90%.

We combine two wells to create a fluorescence decay and fluorescence anisotropy decay. The fluorescence lifetimes of BODIPY-C_{12} in the mixtures containing 60% and 90% of glycerol are similar to the fluorescence lifetime of BODIPY-C_{12} in cells. If 60% and 90% V/V glycerol/methanol solutions in a well, the fluorescence and anisotropy decay can be created using the information from Figure 4.14(b).

By binning the fluorescence decays from two individual wells each containing a homogeneous solution, we mimic a heterogeneous environment consisting of two different viscosities. We therefore expect a double-exponential fluorescence decay, with one decay time reporting the viscosity in one well, and the other decay time reporting the viscosity in the other well. This is shown in Figure 4.15(a, b), which shows 60% and 90% glycerol. A straightforward visual inspection shows that the decay is not mono-exponential, as expected. A bi-exponential function is used to fit the fluorescence decay. The fluorescence lifetimes of BODIPY-C_{12} in the solutions with combination of 60% and 90% are 1.28 ± 0.01 ns and 3.40 ± 0.06 ns which is in agreement with the results from the individual solutions by fitting a monoexponential function.

The corresponding fluorescence anisotropy decay can be calculated using eq. 1.18 (see Figure 4.15(c)). Again, a visual inspection reveals the similarity of the decays with those observed in cells in Figure 4.13, i.e. they show a dip-and-rise behaviour. Eq. 4.5 is used to fit the time-resolved fluorescence anisotropy decay. The rotational correlation times of BODIPY-C_{12} in the solutions with combination of 60% and 90% are 3.03 ± 0.35 ns and 16.55 ± 1.18 ns. Again, this is in excellent agreement with the individual solution fitting a monoexponential fluorescence anisotropy decay function.

A dip-and-rise anisotropy decay can also be seen in Figure 4.15(d), when another two wells (45% and 90%) of fluorescence from Figure 4.14 are

combined. A bi-exponential function is used to fit the fluorescence decay. The fluorescence lifetimes of BODIPY-C_{12} in the solutions with combination of 45% and 90% are 0.90 ± 0.01 ns and 3.34 ± 0.06 ns which again is in agreement with the results from the individual solutions by fitting a monoexponential decay function.

The corresponding fluorescence anisotropy decay can be calculated using eq. 1.18 (see Figure 4.15(d)). Again, a visual inspection reveals the similarity of the decays with those observed in cells in Figure 4.13, i.e. they show a dip-and-rise behaviour. Eq. 4.5 is used to fit the time-resolved fluorescence anisotropy decay. The rotational correlation times of BODIPY-C_{12} in the solutions with combination of 60% and 90% are 2.10 ± 0.44 ns and 19.04 ± 1.26 ns. Again, this is in excellent agreement with the individual solution fitting a monoexponential fluorescence anisotropy decay function.

For both examples, eq. 4.5 can be used to precisely fit the data points for associated anisotropy decay. In addition, when the differences in two fluorescence lifetimes and two rotational correlation times are significant, a dip-and-rise curve is more obvious. We use the procedure of studying a well-controlled and known system in a multiwell plate to gain insight into unknown systems, i.e. cells. On the basis of this, we are more confident that the dip-and-rise behaviour of a fluorescent molecular rotor in cells reports a heterogeneous environment in cells. It does not appear to be an artefact, because this behaviour is reproducible in the controlled environment of the multiwell plate imaging experiment.

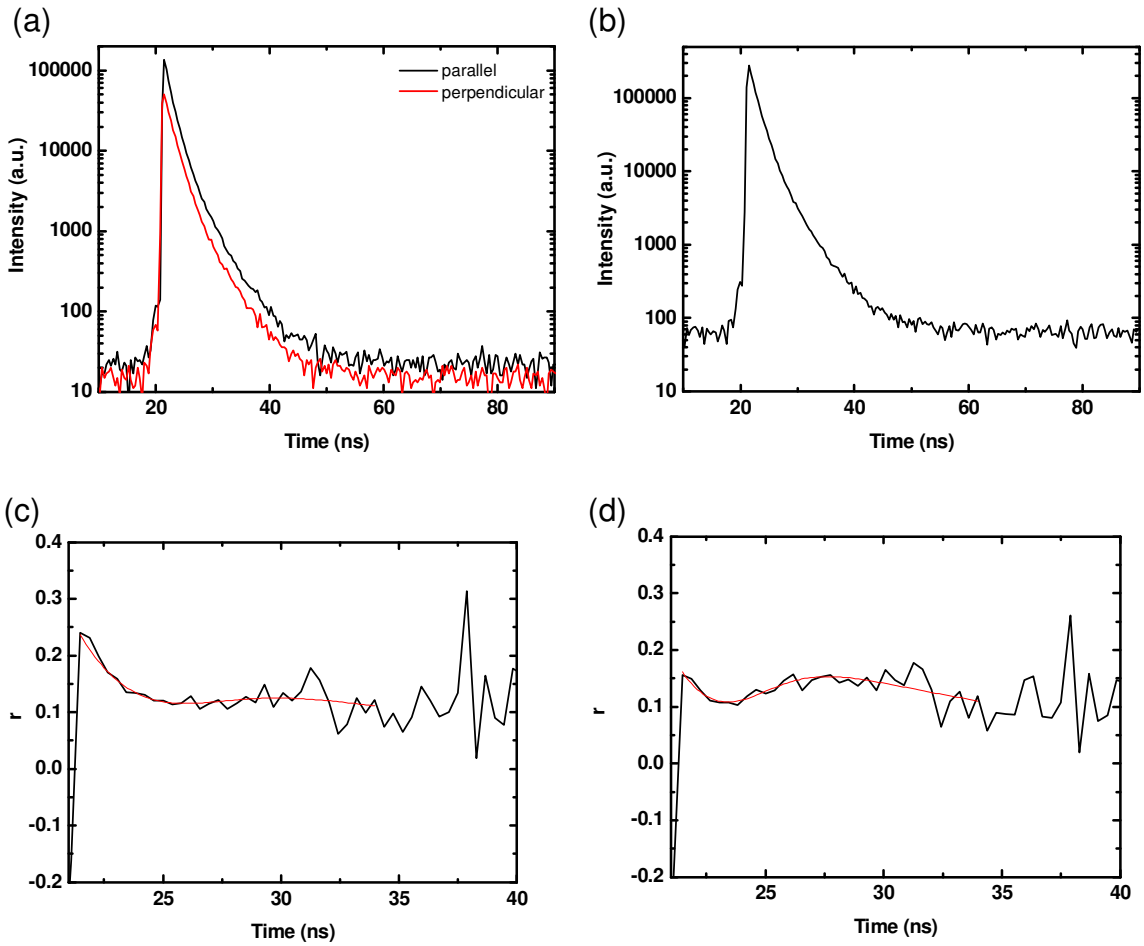

Figure 4.15 (a) The orthogonal polarized fluorescence decays, (b) fluorescence decay and (c, d) the time-resolved fluorescence anisotropy of BODIPY-C_{12} using a combination of the polarized fluorescence decays in two wells. (a-c) 60% and 90%. (d) 45% and 90% of Figure 4.14.

4.4.4 Steady-State Anisotropy Mapping from Time-Resolved Fluorescence Measurements

The fluorescence decay counts in cells in each pixel were not enough to get good statistics for anisotropy decay fitting result in each pixel. Therefore, an integration over the decay and a threshold of photons>600 were used to calculate the steady-state anisotropy by using Matlab. This is another approach to obtain a viscosity map by relating it to the anisotropy (refer to Table 4. 1). The code for creating an anisotropy mapping from a time-resolved fluorescence anisotropy decay is described in the appendix. The fluorescence intensity image and the corresponding steady-state fluorescence anisotropy of BODIPY-C_{12} in

HeLa cell are shown in Figure 4.16. The colour spectrum (see Figure 4.16(c)) is from blue to red for the anisotropy value from 0 increasing to approximately 0.3. The anisotropy mapping of BODIPY-C_{12} in puncta regions, i.e. lipid droplets appears in blue colour, and the regions outside lipid droplets are mainly in yellow. It was demonstrated that an increase in viscosity results in an increasing anisotropy. From the histogram of steady-state anisotropy as shown in Figure 4.16(d), there are two major anisotropy values of 0.143 ± 0.027 and 0.197 ± 0.031 which correspond to a viscosity of 84 cP and 1185 cP, respectively. No r_∞ is taken into account here.

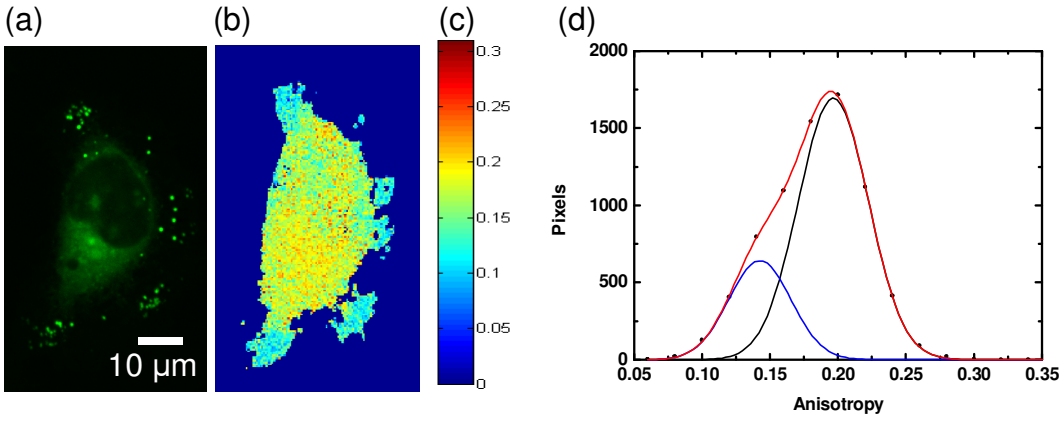

Figure 4.16 (a) The intensity image, (b) the corresponding steady-state anisotropy image with (c) the colour bar and (d) the histogram of BODIPY-C_{12} in HeLa cells.

The viscosities of different regions using different measurements are illustrated in Table 4. 2. It appears that the intracellular viscosities are different according to the lifetime and anisotropy measurements. The viscosity calculated from the lifetime is based on the intramolecular twisting mechanism; however, the viscosity calculated from fluorescence anisotropy measurements is based on the tumbling of the whole molecule.

Table 4. 2 The intracellular viscosities using BODIPY-C_{12} via lifetime and anisotropy measurements.

	Method	Viscosity (cP)	
		Puncta	Outside puncta
HeLa cells	FLIM (a signal pixel) at 32℃	~155	~241
	FLIM (a signal pixel) at 37℃	~118	~169
	Time-resolved fluorescence anisotropy (area binning) at 32℃	~30 ~218	~34 ~207
	Steady-state fluorescence anisotropy [a] (a single pixel) at 32℃	84	1185
	Steady-state fluorescence anisotropy [b]	Up to 70[129]	
SK-OV-3 cells	FLIM at room temperature	~160[100]	~260[100]
	Time-resolved fluorescence anisotropy (area binning) at room temperature	60-80 for whole cells[100, 128]	

[a] The values calculated from the time-resolved fluorescence anisotropy measurements using a 63x water immersion objective lens (NA=1.2)
[b] The values calculated from the steady-state fluorescence anisotropy measurements using a 63x oil immersion objective lens (NA=1.4)[129]

From the time-resolved anisotropy measurements, the fluorophores were found to rotate restrictively, however fluorescence lifetime measurements cannot reveal this phenomenon. Due to hindered rotation of fluorophores in HeLa cells, an appropriate steady-state equation in eq. 4.1 is needed to take this effect into account. There are two fluorescence lifetimes in pixel binning of polarization-resolved fluorescence imaging, and the fluorescence lifetimes of BODIPY-C_{12} in lipid droplets is similar to that outside lipid droplets. The results of fluorescence decay fitting indicate the fluorescence of BODIPY-C_{12} with the shorter lifetime contributes more than that with the longer lifetime to the total fluorescence decay. If BODIPY-C_{12} only tends to be located at the membrane of cells, it may explain why the lifetime of BODIPY-C_{12} in lipid droplets and the regions outside lipid droplets are similar via pixel binning in time-resolved fluorescence anisotropy measurements. The components of lipid droplets and the membranes of ER consist of lipids, proteins etc. Due to a greater contribution of BODIPY-C_{12} with the shorter lifetime to fluorescence decay, we can use a monoexponential decay function to fit the fluorescence decay in a few binned pixels measured via FLIM. It can be seen that the fluorescence lifetime of

BODIPY-C_{12} in lipid droplets is shorter than that outside lipid droplets for lifetime and time-resolved fluorescence anisotropy measurements.

The steady-state anisotropy in cell environments does not take r_∞ into account. We simulate fluorescence decays of a fluorophore with the same fluorescence lifetime and rotational correlation time but different r_∞, and the decays is shown in Figure 4.17(a), and the corresponding anisotropy decay is shown in Figure 4.17(b). By binning the fluorescence decays from two orthogonal polarized decays, the steady-state fluorescence anisotropy can be calculated using eq. 1.17. The steady-state anisotropy for the fluorophore with a lifetime time of 2 ns, rotational correlation time of 2 ns and r_∞=0 is 0.20. In contrast, the steady-state anisotropy for the fluorophore with a lifetime time of 2 ns, rotational correlation time of 2 ns and r_∞=0.1 is 0.25. For the anisotropy for fluorescent molecules with the same rotational correlation time, the hindered rotation produces an overestimate.

A calibration of anisotropy versus viscosity based on eq. 4.1 is for a freely rotational fluorophore. In our case, BODIPY-C_{12} in cells has been found to rotate restrictively. According to the simulation, the hindered dye compared to the freely rotational dye results in a higher steady state anisotropy. Hence, the viscosity measured based on the steady-state fluorescence technique using BODIPY-C_{12} and the calibration (Table 4. 1) may overestimate viscosity.

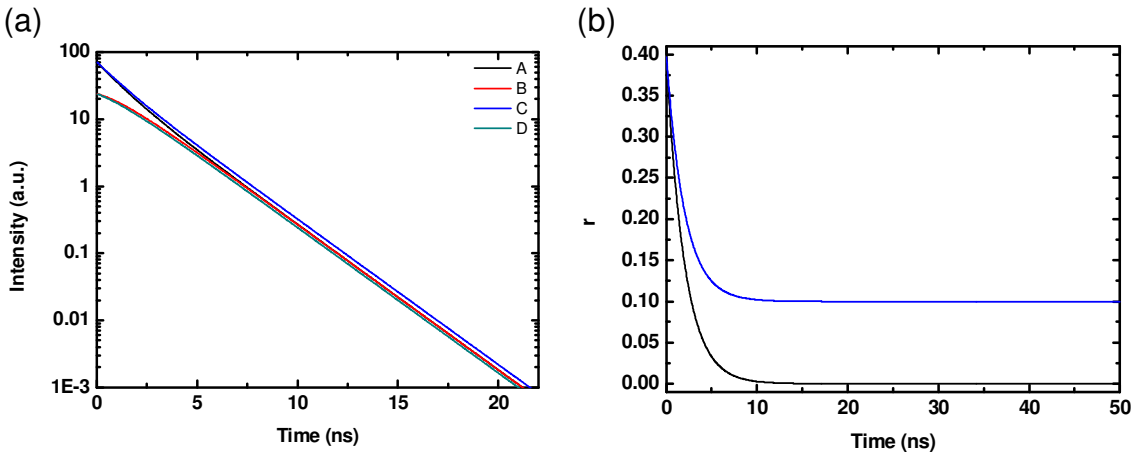

Figure 4.17 (a) Fluorescence decays of a fluorophore with a fluorescence lifetime of 2 ns, a rotational correlation time of 2 ns, r_0 =0.4 and (A: parallel decay, B: perpendicular decay) r_∞ =0, (C: parallel decay, D: perpendicular decay) r_∞ =0.1. (b) Fluorescence anisotropy decay for the cases with r_∞ =0 (black line) and r_∞ =0.1 (blue line).

4.4.5 Combination Fluorescence Lifetime and Rotational Correlation Time of BODIPY-C_{12} in Cells

The relationship between fluorescence lifetime and rotational correlation time for BODIPY-C_{12} in HeLa cells and methanol/glycerol solutions is compared in Figure 4.18. The black data points denote the BODIPY-C_{12} in solutions, the green points are in lipid droplets, and orange points denote the region outside lipid droplets. The data points for BODIPY-C_{12} in HeLa cells do not lie on the straight line of BODIPY-C_{12} in methanol/glycerol mixtures (Figure 4.18). In other words, the fluorescence properties of BODIPY-C_{12} in cells are not in agreement with that in solutions. It has been reported that there are straight lines with the same gradient but different intercept in the plot of double logarithmic scale of lifetime and viscosity.[120] According to Peng and his co-workers' investigation, the fluorescent molecular rotors in the same viscosity but different solvents could cause different fluorescence lifetime. It means the constant z of eq. 2.9 and eq. 2.10 changes in different solutions. Therefore, fluorescent molecular rotors in different environments could follow a straight line but different intercept on a plot of log lifetime versus log rotational correlation time. This is an explanation why there is a discrepancy in the relationship between lifetime and

rotational correlation time of BODIPY-C_{12} in cells and methanol/glycerol mixtures.

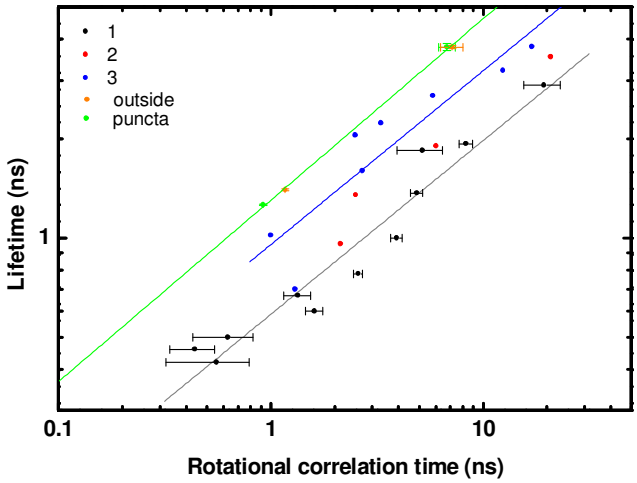

Figure 4.18 The relationship between the fluorescence lifetime and rotational correlation time of BODIPY-C_{12} in methanol/glycerol mixtures from (●, ● and ●) Figure 4.11, and cell environments (● denotes lipid droplets, and ● denotes the regions outside lipid droplets). The light green line is used to describe the behaviour of BODIPY-C_{12} in cells.

4.5 Fluorescence Lifetime and Rotational Correlation Time of BODIPY-C_{12} in Silicone oil

The relationship between lifetime and rotational correlation time of BODIPY-C_{12} in cells is different to that in methanol/glycerol solutions. Hence, another solvent has been proposed to use. We prepared a stock solution of BODIPY-C_{12} in Heptane, and a set of silicone fluid (XIAMETER PMX-200, Dow Corning) whose viscosity is from 100 centiStokes (cSt) to 1000 cSt with a constant dye concentration of 16.5 μM.

Here, we measured the fluorescence decays of BODIPY-C_{12} in silicone oils shown in Figure 4.19. A monoexponential decay function was used to fit the fluorescence decays. The fluorescence lifetimes are listed in Table 4. 3. The

fluorescence lifetime is almost the same in silicone oil regardless of variations of viscosity.

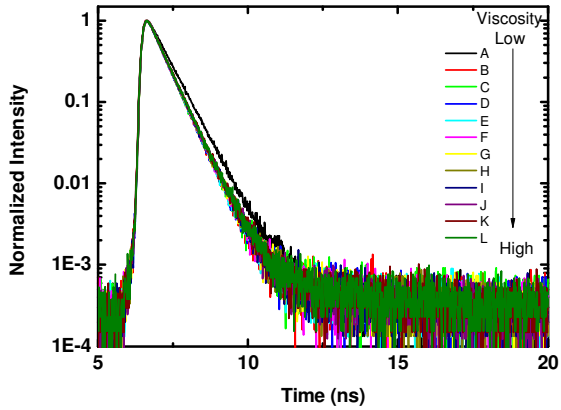

Figure 4.19 The fluorescence lifetime of BODIPY-C_{12} in solutions. The symbol from A to L denotes different viscosity solvents with an increasing tendency, and the solvent description is illustrated in Table 4. 3.

Table 4. 3 Viscosity, lifetime and rotational correlation time of BODIPY-C_{12} in silicone oil.

Symbol	Solvent descriptions	η (cSt) at 25℃	η (cP) at 25℃	τ_f (ns)	θ (ns)
A	Heptane	-	0.386	0.607	
B	100 cSt	100	96[b]	0.517	0.26
C	1.8 ml 100 cSt + 0.2 ml 1000 cSt	190[a]	-	0.519	0.38
D	1.6 ml 100 cSt + 0.4 ml 1000 cSt	280[a]	-	0.518	0.35
E	1.4 ml 100 cSt + 0.6 ml 1000 cSt	370[a]	-	0.521	0.33
F	1.2 ml 100 cSt + 0.8 ml 1000 cSt	460[a]	-	0.524	0.34
G	1.0 ml 100 cSt + 1.0 ml 1000 cSt	550[a]	-	0.524	0.32
H	0.8 ml 100 cSt + 1.2 ml 1000 cSt	640[a]	-	0.526	0.35
I	0.6 ml 100 cSt + 1.4 ml 1000 cSt	730[a]	-	0.530	0.34
J	0.4 ml 100 cSt + 1.6 ml 1000 cSt	820[a]	-	0.531	0.31
K	0.2 ml 100 cSt + 1.8 ml 1000 cSt	910[a]	-	0.534	0.31
L	1000 cSt	1000	967[b]	0.535	0.36

[a] The intermediate viscosity is calculated using $\eta_{mix} = V_1\eta_1 + V_2\eta_2$, where V_1, V_2 are the volume fraction of 100 cSt and 1000 cSt of silicone oil.

[b]The specific gravity for 100 cSt and 1000 cSt silicone fluids is 0.964 and 0.970 at 25℃,[203] and the density of water is 0.9971 g/ml at 25℃.[204] Hence, the density of fluids can be calculated and using eq. 1.29, the viscosity in cP can be calculated.

In addition, the result shows the fluorescence lifetime of BODIPY-C_{12} in methanol (280 ps, section 3.2.5) is lower than that in heptane (607 ps). However, the viscosity of methanol (0.6 cP) is higher than that of heptane (0.386 cP). According to the Förster-Hoffmann equation (eq. 2.10), fluorescence lifetime increases with increasing viscosity. It has been reported that the fluorescence lifetime of crystal violet apparently increases with decreasing solvent dielectric constant, at same viscosity, and a hypothesis that the variation of solvent dielectric constant results in a different potential surface during the relaxation process was proposed.[205] If the relaxation mechanism of BODIPY-C_{12} in non polar solvents is different to that in polar solvents, then it could be an explanation why the fluorescence properties behave in different ways.

A small hint of different relaxation state of BODIPY-C_{12} in methanol/glycerol mixtures and silicone oil can be seen form a comparison of emission spectrum of BODIPY-C_{12} shown in Figure 4.20. It has been shown that the emission spectrum of BODIPY-C_{12} in methanol/glycerol solutions red shifts as the refractive index increases (see section 3.2.3). It seems that the emission spectra of BODIPY-C_{12} are different in silicone oil and methanol/glycerol mixtures. The refractive index of 40% V/V glycerol was measured to be 1.4037 (see Table 3. 1), which is similar to that of silicone fluids (n=1.4030 for 100 cSt and 1.4035 for 1000 cSt),[203] but viscosity and dielectric constant are different. The dielectric constant is ~2 for silicone oil[206] and 31-39 for methanol/glycerol mixtures (Table 3. 1). Moreover, a blue shift of the emission spectrum of BODIPY-C_{12} is found for an increase in refractive index of silicone oils, which is the opposite with respect to the relationship between emission spectrum and refractive index in methanol/glycerol mixtures. However, from this information alone, we could not make a conclusion that only dielectric constant influences the relaxation mechanism for BODIPY-C_{12}.

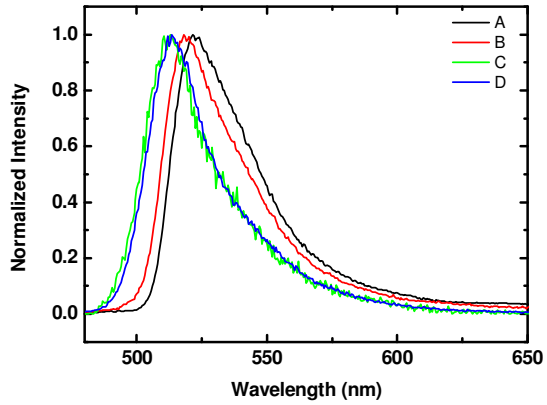

Figure 4.20 Emission spectrum of BODIPY-C_{12} in silicone fluids of (A) 100 cSt and (B) 1000 cSt, and methanol/glycerol mixtures with (C) 40% of glycerol and (D) 90% of glycerol.

The rotational correlation times of the dye in silicone oils were also measured. The polarization fluorescence and anisotropy decays of BODIPY-C_{12} in viscosity of 100 and 1000 cSt silicone oil are shown in Figure 4.21. Figure 4.21(a-b) shows a fast rotation of BODIPY-C_{12} due to the overlapping of the orthogonal polarized fluorescence decay before the lifetime. The rotational correlation time of dye were found to be 0.3-0.4 ns in the viscosity range of 100-1000 cSt. These seem to be no correlation between viscosity and rotational correlation time exists among these fluids. There are few hypotheses for that, first, BODIPY-C_{12} in silicone oil has different sensitivity. It may have the same tendency like Figure 3. 9 but at different viscosity regime. Second, the relaxation mechanism of BODIPY-C_{12} for non-polar solvents may be different for polar environments. A further study is necessary in order to understand the different behaviour for BODIPY-C_{12} in silicone oil.

The details of BODIPY-C_{12} in silicone oils are illustrated in Table 4. 3. A comparison of fluorescence lifetime versus rotational correlation time of BODIPY-C_{12} is illustrated in Figure 4.22. It seems that silicone oil is still not an appropriate medium to describe the behaviour of BODIPY-C_{12} in cells, i.e. the data points do not lie on the same straight line.

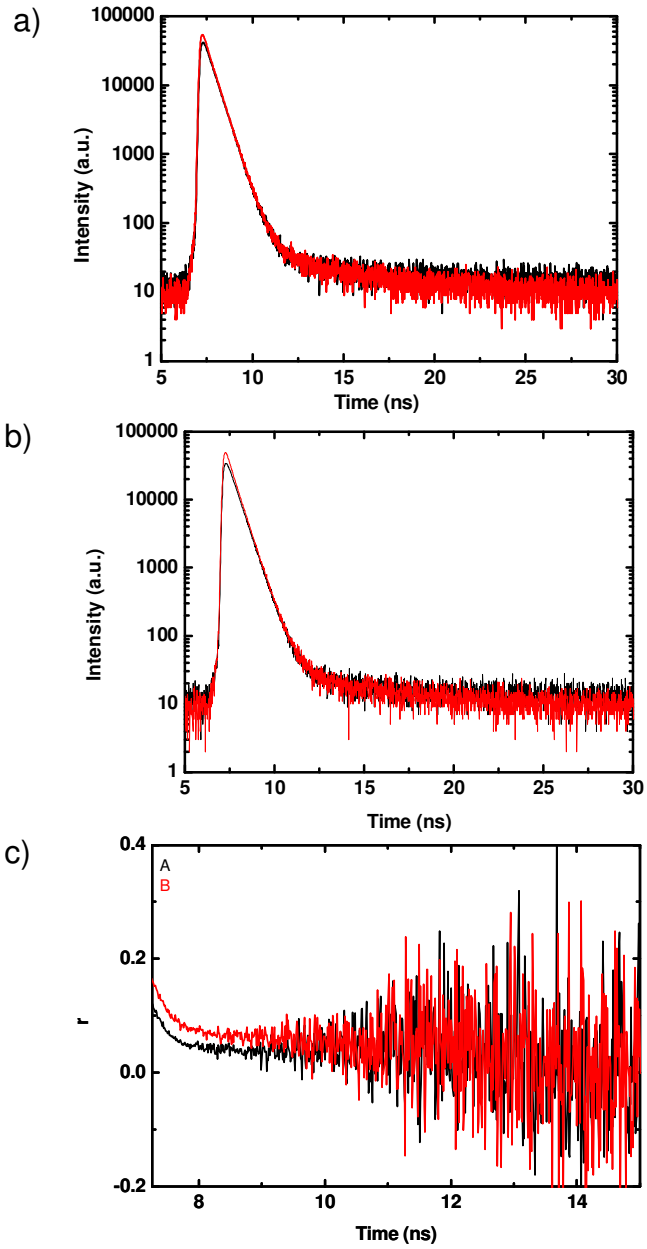

Figure 4.21 The orthogonal polarized fluorescence decays of BODIPY-C_{12} in (a) 100 and (b) 1000 cSt silicone oils. (c) The anisotropy decays for (A) 100 cSt and (B) 1000 cSt silicone oils. In panel a and b, the red line denotes the fluorescence decay in parallel polarization compared to the incident light, and the black line denotes the fluorescence decay in the perpendicular polarization.

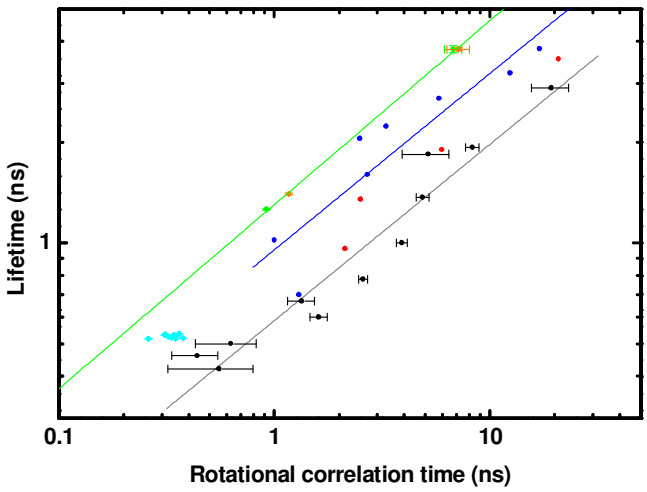

Figure 4.22 The relationship between fluorescence lifetime and rotational correlation time of BODIPY-C_{12} in (●) silicone oil, HeLa cells and methanol/glycerol mixtures (the data are the same as in Figure 4.18).

4.6 Summary

By combining the Perrin equation and the Stokes-Einstein-Debye equation with the Förster-Hoffmann equation, a theoretical framework is created which means the anisotropy of a fluorescent molecular rotor can quantitatively be related to viscosity. This is described by eq. 4.1 for not only typical fluorescent molecules but also fluorescent molecular rotors. BODIPY-C_{12} provides a best dynamic range in wide range of viscosity. Steady-state polarization-resolved fluorescence technique offers a good solution to measure viscosity from anisotropy, i.e. it is relatively rapid and easy. However, hindered rotations cannot be identified with this technique, and lead to an overestimation of the steady-state anisotropy values. Nevertheless, steady-state anisotropy imaging still provides contrast between different regions in cells.

An equation based on the Förster-Hoffmann equation and the Stoke-Einstein-Debye equation (eq. 4.4) has been made to link the relationship between fluorescence lifetime and rotational correlation time for fluorescent molecular rotors. The experimental results well overlap with the theoretical framework for BODIPY-C_{12}. It has also been demonstrated that the behaviour between

fluorescence lifetime and rotational correlation time for fluorescent molecular rigid molecules is different.

More information about the interaction between fluorophores and medium can be measured using time-resolved fluorescence anisotropy technique. It was found that the fluorescent molecular rotor in cells with two different viscosity environments results in two fluorescence lifetimes and rotational correlation times which may lead a dip-and-rise anisotropy decay. Regarding this phenomenon, it has also been explicitly demonstrated that BODIPY-C_{12} solutions in multiwell plate perform the same way as BODIPY-C_{12} in cells. However, for a rigid molecule in the same conditions as a fluorescent molecular rotor, the anisotropy decay follows an exponential function as expected, and shown in the appendix. It was also found that BODIPY-C_{12} as a fluorescent molecular rotor fails to respond to the viscosity in silicone oil with viscosity of 96-967 cP.

There are heterogeneous environments in lipid droplets and the regions outside lipid droplets. From time-resolved fluorescence anisotropy measurements, the fluorophore population in low viscosity environments in cells is higher than that of high viscosity environments. This also follows from the analysis of FLIM, using a monoexponential decay function to fit the decay in each pixel.

All in all, the viscosity of the environment can be measured by BODIPY-C_{12} via fluorescence lifetime and fluorescence anisotropy measurements.

Chapter 5

The Dipole Moment of a Fluorophore Relative to the Solvent Refractive Index

5.1 Introduction

The variation of the radiative rate of a fluorophore is proportional to the square of the refractive index of the solution according to the Strickler-Berg formula (eq. 2.11).[77, 207] This is predicted theoretically and has been demonstrated experimentally by measuring the fluorescence lifetime and fluorescence quantum yield as a function of the refractive index of the fluorophore's environment. The refractive index is the ratio of the speed of light in vacuum divided by the speed of light in the medium, and it varies with solvent or the pressure.

Dmitri Toptygin et al. has proposed an advanced model (eq. 2.18) where the relationship between the radiative rate constant and the refractive index of the solution can yield the electronic transition dipole and the shape of the fluorescent molecule.[162] Toptygin and his research group have successfully extracted the information of a tryptophan residue in a protein using eq. 2.18. The electronic transition dipole moment is associated with the transition between two states, and its magnitude can be also calculated through the wave functions of two electronic states. In this thesis, various fluorescent molecules are used to examine this model, e.g. Rhodamine 123 (Rh123), Nile red, BODIPY-C_{12} and its related molecule, PM546. Our results show that Nile red in methanol/glycerol mixtures does not follow the model (eq. 2.18), and it could be due to the complex fluorescence mechanism of Nile red.

The molecular structure of PM546, Nile red and Rh123 is shown in Figure 5. 1.

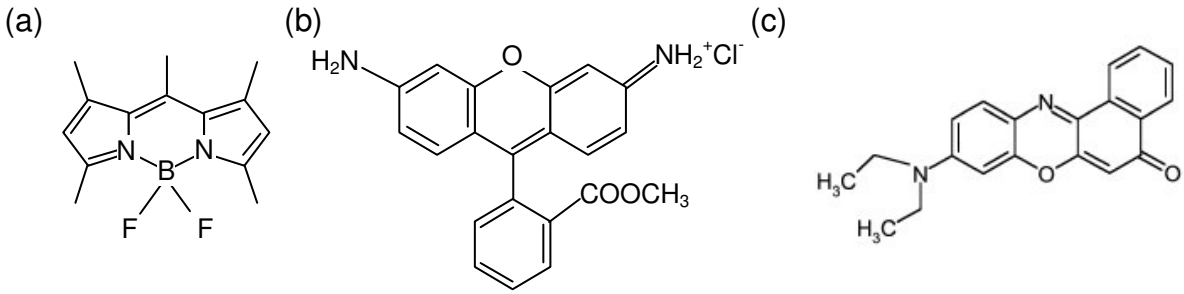

Figure 5. 1 The molecular structure of (a) PM546, (b) Rh123, and (c) Nile red.[208]

5.2 Experimental Section

Stock solutions of Rh123 (Sigma), PM546 (Exciton), BODIPY-C_{12} and Nile red (Invitrogen) were prepared in methanol. The concentration for Rh123, PM546, BODIPY-C_{12} and Nile red was 1.21 mM, 0.60 mM, 2.65 mM and 0.60 mM, respectively. Methanol was mixed with a different ratio of glycerol in order to change the refractive index of the solutions. The binary mixtures were made from 0% up to 95% of volume fractions of glycerol with the same concentration of dye. The final dye concentration for the spectroscopic measurement is 14.5 μM for Rh123, 2.44 μM for PM546, 13 μM for BODIPY-C_{12}, and 2.51 μM for Nile red. The refractive indices of the solutions were measured using a refractometer as mentioned in section 2.2.2 and section 3.2.2. The parameters for absorption and emission spectra measurements are illustrated in Table 5. 1.

Table 5. 1 The volume (V) and the concentration ([C]) of dye solutions and parameters for absorption and emission spectra measurements.

		PM546	BODIPY-C_{12}	Nile red	Rh123
Stock solution concentration (mM)		0.60	2.65	0.60	1.21
Absorption	V (ml)	2	2	2	2
	[C] (μM)	2.44	13.00	2.51	14.50
	Scan Speed (nm/min)	120	300	120	120
	Slit width (nm)	2	2	2	2
Emission	Ex. (nm)	465	473	488	475
	Scan Speed (nm/min)	120	300	120	150
	Slit width (nm)	3	2.5	3	7

Fluorescence lifetime measurements were carried out using the pulsed diode laser (Hamamatsu, PLP-10 470 nm) at 10 or 20 MHz. TCSPC combined with a confocal microscope (Leica, TCS SP2) was used. Individual wells in a 96-wells-glass-bottom microplate were filled with 200 μl of PM546, Nile red, BODIPY-C_{12} and Rh123 solutions. The fluorescence signal was captured through an objective (Leica) and a band-pass filter before being collected by a hybrid PMT detector. The band-pass filter for Rh123 is 550 nm (Semrock, FF01-550/88-25), 650 nm (Thorlabs) for Nile red, and 514 nm (Semrock) for BODIPY-C_{12} and PM546.

5.3 PM546

5.3.1 Absorption and Emission Spectra

Absorption and emission spectra of PM546 in methanol and glycerol mixtures with 10% and 90% of glycerol are shown in Figure 5. 2. The absorption and emission spectra show a slight bathochromic shift as the percentage of glycerol is increased, that is, the solvent polarity is increased. The spectral position of the absorption and emission band can be used to estimate the variation of the transition dipole moment of a fluorophore using three solvatochromic models.

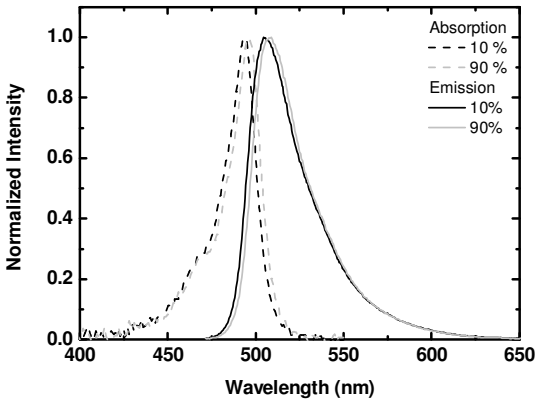

Figure 5. 2 The absorption (dashed line) and emission spectra (solid line) of PM546 in the mixtures with volume percentage of 10% (black) and 90% glycerol (grey).

Here, the solvatochromic methods (eq. 2.21 – eq. 2.26) are used to estimate the dipole moments of fluorophores. The absorption and emission peaks of PM546 show a linear increase with a increasing on refractive index (see Figure 5. 3(a)). The y-axis values for eq. 2.21 and 2.23 are Stoke shifts, and the difference between two models is the x-axis is using different parameters to present the solvent polarity function. It results in different intercept and gradient of the plot according to eq. 2.21 and eq. 2.23. It can be seen there is a linear relationship between the Stokes shift and the solvent polarity function for PM546 using eq. 2.21 and eq. 2.23, as shown in Figure 5. 3(b, c). A small Stokes shift is observed for PM546 in methanol/glycerol solutions in this experiment, and it is consistent with the theoretical calculation[195] and other experimental results[209] for PM546. It has been suggested that a small Stokes shift results from a similar geometry in the ground and excited state.[195]

The Stokes shifts for PM546 in all solution are similar, and thus the differences of dipole moments in each solvent are similar according to eq. 2.21 and eq. 2.23. A finding of $\mu_e > \mu_g$ for PM546 in methanol and glycerol mixtures is observed due to a negative gradient in Figure 5. 3(d) according to the Kawski-Chamma-Viallet's model (eq. 2.25). However, the theoretical calculation shows $\mu_e < \mu_g$.[195] The solvent is different in the experiment and the theoretical

calculations and this probably yields the different results. In other words, the interaction of solute and solvent was not taken into account in the theoretical method.

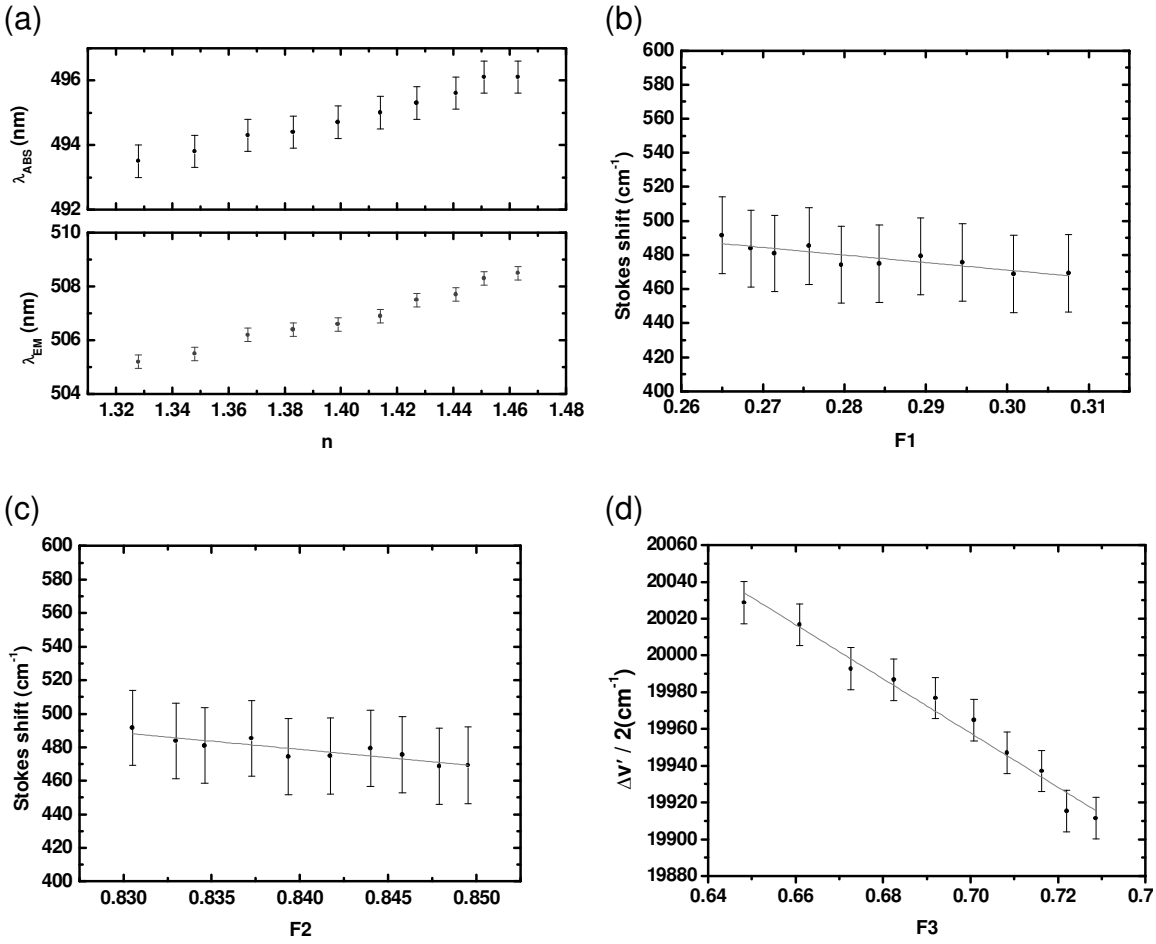

Figure 5. 3 (a) Absorption and emission peaks of PM546 in methanol/glycerol solutions. The variation of Stokes shift of PM546 with F1 (b) and F2 (c) in methanol/glycerol mixtures. (d) The relationship between arithmetic mean of Stokes-shift and F3 of PM546 in mixtures of glycerol and methanol.

Using the fluorescence quantum yield (Φ) of PM546 in methanol as a reference, Φ=0.99,[210] correcting the emission intensity for a slight concentration difference and assuming the same extinction coefficient of PM546 in mixtures, the quantum yield of PM546 in mixtures can be calculated from eq. 3.2. Errors in the calculation of fluorescence quantum yield may be produced due to this assumption. The calculated fluorescence quantum yield of PM546 in the

solutions is shown in Figure 5. 4. The fluorescence quantum yield of PM546 is in the range of 0.92 to 1.01 over the squared refractive index of 1.70 to 2.20. The value of Φ should be no more than 1, and within the standard deviation of the results, this is the case Φ of PM546 in the solutions is constant.

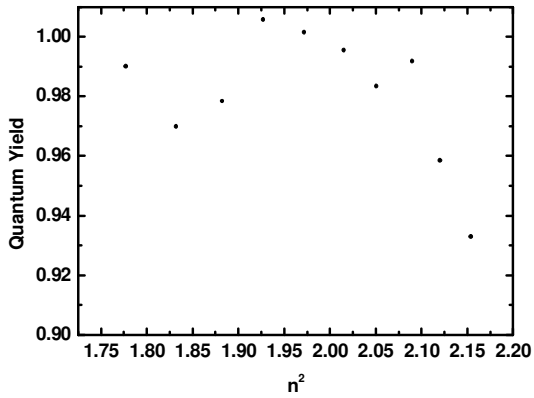

Figure 5. 4 A plot of fluorescence quantum yield versus the squared refractive index of solvents for PM546 in methanol/glycerol mixtures.

The quantum yield (Φ) can be estimated from another point of view too. The radiative rate constant (k_r) of a fluorescent molecule is a function of the square of the medium refractive index (n) according to eq. 2.11. Using this concept and eq. 1.2 one can write:

$$\Phi = \frac{k_{r0} \cdot n^2}{k_{r0} \cdot n^2 + k_{nr}} \tag{5. 1}$$

where

$$k_r = k_{r0} \cdot n^2 \tag{5. 2}$$

Figure 5. 5 shows a relationship between fluorescence quantum yield and the squared refractive index for fluorescence quantum yield of 0.40 and 0.94 in refractive index of 1.33 according to eq. 5.1. If the non-radiative rate constant is constant and the radiative rate constant obeys eq. 2.11, the quantum yield of a

fluorophore increases with refractive index of solution. The effect of the refractive index on the quantum yield is larger for small quantum yields than for high quantum yields. It is approaching 1 if the refractive index=∞ based on eq. 5.1.

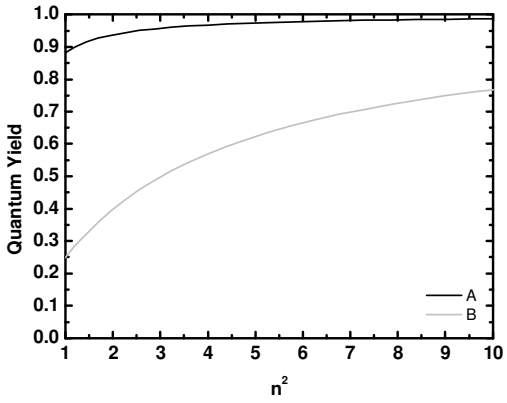

Figure 5. 5 Simulation the relationship between quantum yield and the squared refractive index according to eq. 5.1. The fluorescence quantum yield trend is estimated assuming the non-radiative rate constant is independent on refractive index for a quantum yield of (A) 0.94 and (B) 0.40 in n=1.33.

The fluorescence quantum yield of a dye also varies with the refractive index of a medium. Using eq. 5.1, the quantum yield of PM546 is 0.99 in methanol and 0.99 in 90% V/V glycerol. Thus, in this case the fluorescence quantum yield of PM546 in the mixtures is constant.

5.3.2 Lifetime

The normalized fluorescence decay of PM546 in mixtures is shown in Figure 5. 6. The notes in the figures present the volume fraction of glycerol in the binary mixtures. A monoexponential decay function is used to fit the fluorescence decay, and the lifetimes are listed in Table 5. 2. It can be seen that there is a slight decrease of fluorescence lifetime when the ratio of glycerol increases.

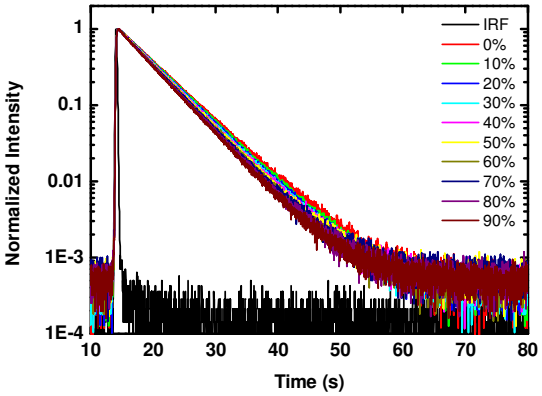

Figure 5. 6 The fluorescence decay of PM546 in mixtures of methanol and glycerol. The percentage values indicate the glycerol percentage.

Table 5. 2 The refractive indices and fluorescence lifetime of PM546 in methanol/glycerol solutions, respectively.

Volume % of glycerol	Refractive index	τ_f (ns)
0	1.328	5.64
10	1.348	5.54
20	1.367	5.44
30	1.383	5.37
40	1.399	5.30
50	1.414	5.23
60	1.427	5.16
70	1.441	5.10
80	1.451	5.02
90	1.463	4.95

A plot of the inverse fluorescence lifetime versus the square of the refractive index is shown in Figure 5. 7. The rate constants of fluorescent molecules can be calculated through a plot based on a rearrangement equation of eq. 1.1 and 5.1.

$$\frac{1}{\tau_f} = k_r + k_{nr} = k_{r0} n^2 + k_{nr} \qquad (5.\ 3)$$

The intercept was found to be $(6.36 \pm 0.35) \times 10^7\ s^{-1}$, and the value of k_{r0} is the slope, which is $(6.37 \pm 0.18) \times 10^7\ s^{-1}$. This model assumes a fixed non-radiative rate constant for PM546 among methanol/glycerol solutions. In order to validate the fitting results, a check of the fluorescence quantum yield of PM546 between the literature and a calculation using the fitting results (Figure 5. 7) has been made. A fluorescence quantum yield can be calculated using the values from the fitting results, resulting in Φ of 63% in the refractive index of 1.33. However, Φ of PM546 is 0.99.[210] Therefore, the model underestimates Φ for PM546 in methanol/glycerol mixtures. In this case, the non-radiative rate constant may not be a constant.

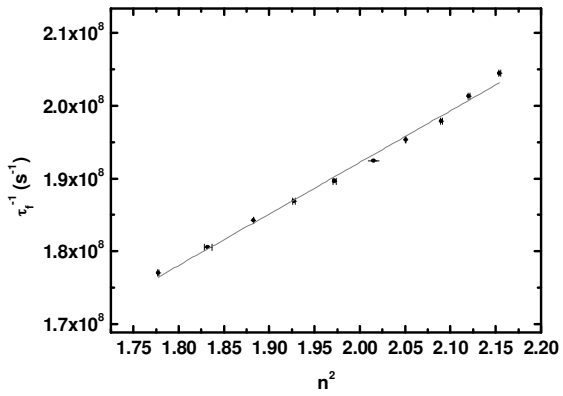

Figure 5. 7 The inverse lifetime of PM546 versus the square of the refractive index of the mixtures.

The radiative rate constant of a fluorescent molecule can be calculated using the definition of fluorescence lifetime and fluorescence quantum yield (eq. 1.1 and eq. 1.2), if the fluorescence lifetime and fluorescence quantum yield are known. The radiative and non-radiative rate constants were calculated from the data, and a plot of the radiative rate constant versus the squared refractive index of PM546 in methanol/glycerol mixtures is shown in Figure 5. 8.

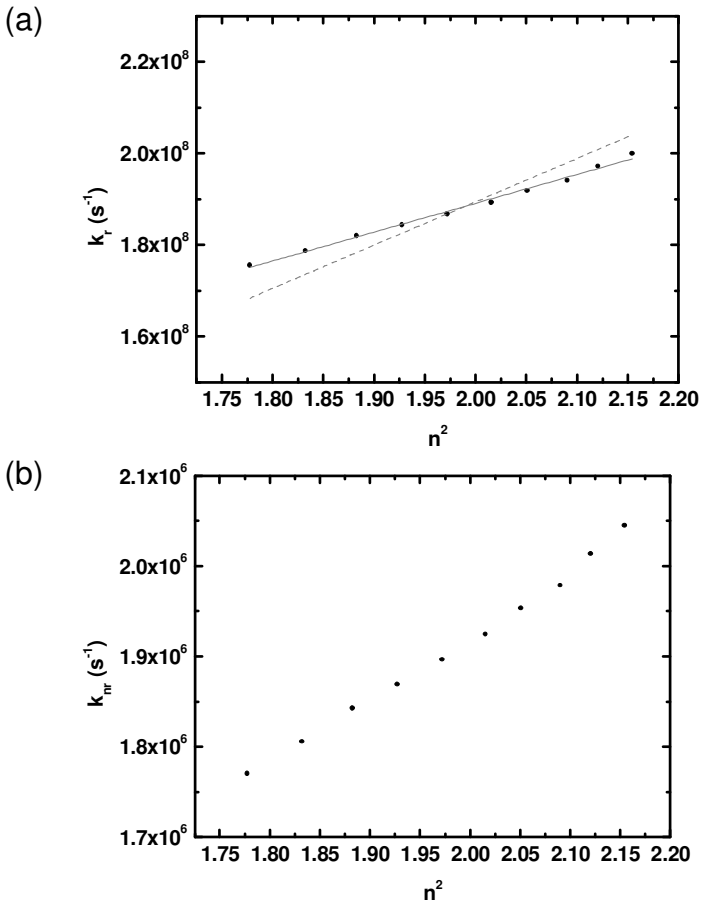

Figure 5. 8 (a) The radiative rate constant of PM546 in the methanol/glycerol mixtures. A fit with variable intercept and gradient is shown in solid line and variable gradient through zero is shown in dashed line. (b) The non-radiative rate constant of PM546 in the mixtures.

According to eq. 2.11, there is a straight line (dashed line) through the zero with a gradient of $(9.47 \pm 0.06) \times 10^{7}$ s^{-1} for the PM546. However, for the best fit of the data with a non-zero intercept, a gradient of $(6.31 \pm 0.18) \times 10^{7}$ s^{-1} with an intercept of $(6.29 \pm 0.35) \times 10^{7}$ s^{-1} is obtained. This could be due to experimental error.

The radiative rate constant of PM546 was calculated from spectroscopy data based on eq. 2.11 yielding a value for the expression that is the gradient of straight-line fit through the origin in Figure 5. 8 of $(1.47 \pm 0.06) \times 10^{8}$ s^{-1}. The experimental results and the theoretical results based on eq. 2.11 are thus not in quantitative agreement. An overestimated radiative rate by the Strickler-Berg

formula occurs when the geometry of the fluorescent molecules change in the excited state via torsional rotation or nonradiative photoisomerization.[14] However, PM546 should be a rigid molecule, so the reason for the overestimation is not understood yet.

The non-radiative rate constant of PM546 in the mixtures varies with the squared refractive index of the solvents, as shown in Figure 5. 8(b).

5.3.3 The Magnitude of the Electronic Transition Moment

The experimental data follow the Toptygin et al.'s equation (eq. 2.18) and they are shown in Figure 5.9. The values of $P1$ and $P2$ (eq. 2.19 & eq. 2.20) can be calculated from the gradient and intercept of a straight line, which are 4.92×10^{-3} $cm^{3/2}$ $s^{-1/2}$ and 0.24 respectively. The magnitude of the transition dipole moment $\mu =$ 7.11 Debye (D) and $L_\mu = 0.19 \pm 0.02$ can be calculated according to eq. 2.19 and eq. 2.20. The value of L_μ is less than 1/3, which means PM546 is an ellipsoidal molecule and the transition moment is along the longest axis of PM546. The finding is consistent with other reports in the literature for pyrromethene dyes. The direction of $S_0 \rightarrow S_1$ transition dipole moment is perpendicular to that of changes in the permanent electric dipole moments.[195, 211-213]

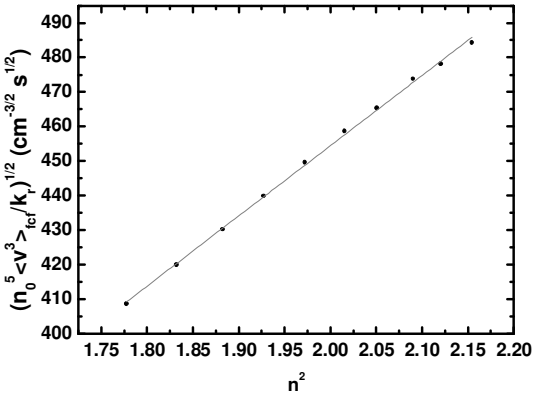

Figure 5.9 Relative variation of the radiative rate with the solvent refractive index for PM546. The straight line represents the data following eq. 2.18. The gradient of this plot is 203.2 ± 2.4 $cm^{-3/2}$ $s^{1/2}$ and the intercept is 48.1 ± 4.8 $cm^{-3/2}$ $s^{1/2}$.

The oscillator strength (f) of the transition 2←1 is correlated with the electronic transition dipole moment (μ_{21}) and the formula is given by[214]

$$\left|\mu_{21}\right|^2 = \frac{3he^2}{8\pi^2 m_e c v} f \qquad (5.4)$$

Here, v is the wavenumber of energy difference between level 1 and level 2, the constant of m_e is the electron mass, h is Planck's constant, c is the light speed in vacuum and e is the charge of an electron.

The value of f was found to be in a range of 0.42 and 1.04 for PM546 using density functional theory (DFT), and it depends on the different models of DFT.[195, 215] The corresponding transition dipole is between 6.5 D and 9.9 D using eq. 5.4 and the value of f calculated from the theory. In addition, it is approximately 6.9 D using the experimental result (f =0.453)[195] and eq. 5.4. It has been reported that the transition dipole of PM546 using some theoretical calculation based on DFT overestimates than that obtained from the experiment.[195] Our result shows that the transition dipole moment of PM546

using Toptygin et al.'s model ($\mu = 7.11$ D) is in excellent agreement with literature values.

The dipole moment of BODIPY and its derivatives have been studied using theoretical calculations.[195, 211, 216] The permanent dipole moment of 3,3',4,4'-difluoro-1,3,5,7-tetramethyl-4a-aza-s-indacene (TM-BODIPY) is 3.27 D in the ground state, 2.73 D in the excited-state and its electronic transition dipole moment is 6.87 D during $S_0 \rightarrow S_1$ transition.[212] The molecular structure of TM-BODIPY is similar to that of PM546, as shown in Figure 5.10. It can be seen that the transition dipole moment is identical for PM546 and TM-BODIPY.

Figure 5.10 The structure of TM-BODIPY.[212]

5.4 BODIPY-C_{12}

5.4.1 The Magnitude of the Electronic Transition Moment

A plot of the radiative rate constant of BODIPY-C_{12} vs. the squared refractive index is shown in Figure 5.11. The fluorescence lifetime and the quantum yield of BODIPY-C_{12} mentioned in chapter 3 lead to the radiative rate constant. A straight line according eq. 2.11 was used to fit the plot yielding a gradient of $(4.5 \pm 0.1) \times 10^7$ s^{-1} (dashed line in Figure 5.11). A fit with variable gradient and intercept results in an inconsistent line to the dashed line, which gradient is $(8.2 \pm 1.8) \times 10^7$ s^{-1} and an intercept is $(-7.4 \pm 3.6) \times 10^7$ s^{-1}. A negative intercept has no physical meaning. The fluorophore is a fluorescent molecular rotor, and the radiative rate constant is small in comparison to the non-radiative rate constant. This would explain the scatter of the data.

The radiative rate constant of BODIPY-C_{12} was calculated from spectroscopy data based on eq. 2.11 yielding a value of $(1.87 \pm 0.07) \times 10^8$ s^{-1} for the expression that is the gradient on the plot of k_r vs. n^2, which is similar to that of PM546 calculated based on the same method. So the results for the radiative rate constant obtained from the gradient of a plot of the time-resolved experimental and theoretical results from the Strickler-Berg formula (eq. 2.11) do not quite agree. A discrepancy in the radiative rate constant obtained by those two methods has been observed for some molecules.[156-161] The reason for the inconsistent results is that the geometry of the fluorescent molecules change in the excited state via torsional rotation or nonradiative photoisomerization.[14]

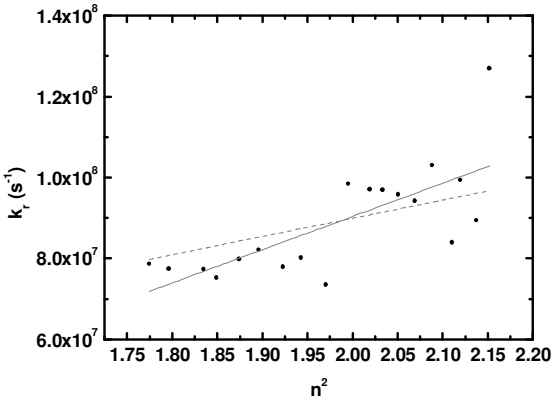

Figure 5.11 The radiative rate constant of BODIPY-C_{12} in the mixtures. Solid line denotes a straight line with variable gradient and intercept values, and the dashed line is for a straight line trough zero.

A relative variation to radiative rate versus the squared refractive index of BODIPY-C_{12} in methanol/glycerol solutions is shown in Figure 5.12. It shows that the experimental results present a bigger deviation from a straight line due to the scatter of the data points, as explained above. There are approximately 50% error for the slope and 25% error for the intercept. The values of P_1 and P_2 for this fluorescent molecule are 9.70×10^{-3} $cm^{3/2}$ $s^{-1/2}$ and 4.34, respectively. The value of $|\mu| = 3.24$ D and $L_\mu = 0.81 \pm 0.10$ are found. It means the transition dipole moment of BODIPY-C_{12} is 3.24 D. The value of L_μ exceeds 1/3, so the

direction of the transition dipole moment is along the smallest axis of the ellipsoidal molecule.

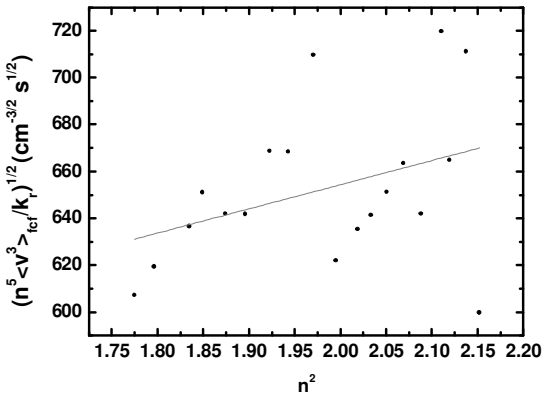

Figure 5.12 Relative variation to the radiative rate with the solvent refractive index for BODIPY-C_{12}. The straight line represents the data following eq. 2.18. The gradient of this plot is 103.13 ± 62.67 $cm^{-3/2}$ $s^{1/2}$ and the intercept is 448.08 ± 124.36 $cm^{-3/2}$ $s^{1/2}$.

5.5 Rh123

5.5.1 Absorption and Emission Spectra

The absorption and emission spectra of Rh123 in 10% and 90% of glycerol are shown in Figure 5.13. The absorption and emission peaks can be extracted from the spectra as shown in Figure 5.14(a). The absorption and emission peaks are shifted to a long wavelength when the polarity of the solvent increases. In addition, the Stokes shift of Rh123 versus the polarity parameters does not show a clear tendency, as shown in Figure 5.14 (b, c). The dipole moment of Rh123 in the excited state is greater than the one in the ground state due to the negative gradient of Figure 5.14 (d). A radius of 0.51 nm[217] is used to compute the value of $\mu_e^2 - \mu_g^2$, which is 0.29 D^2 calculated by using eq. 2.25.

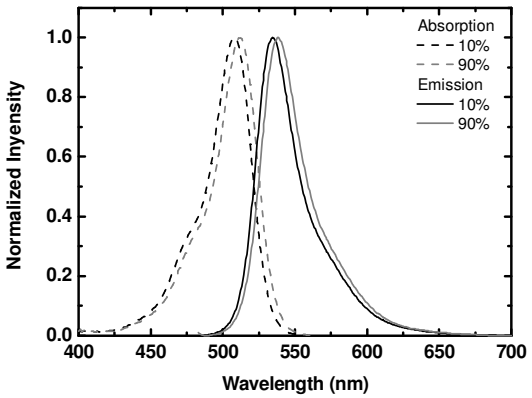

Figure 5.13 The absorption (dashed line) and emission spectra (solid line) of Rh123 in the mixtures with volume percentage of 10% (black) and 90% glycerol (grey).

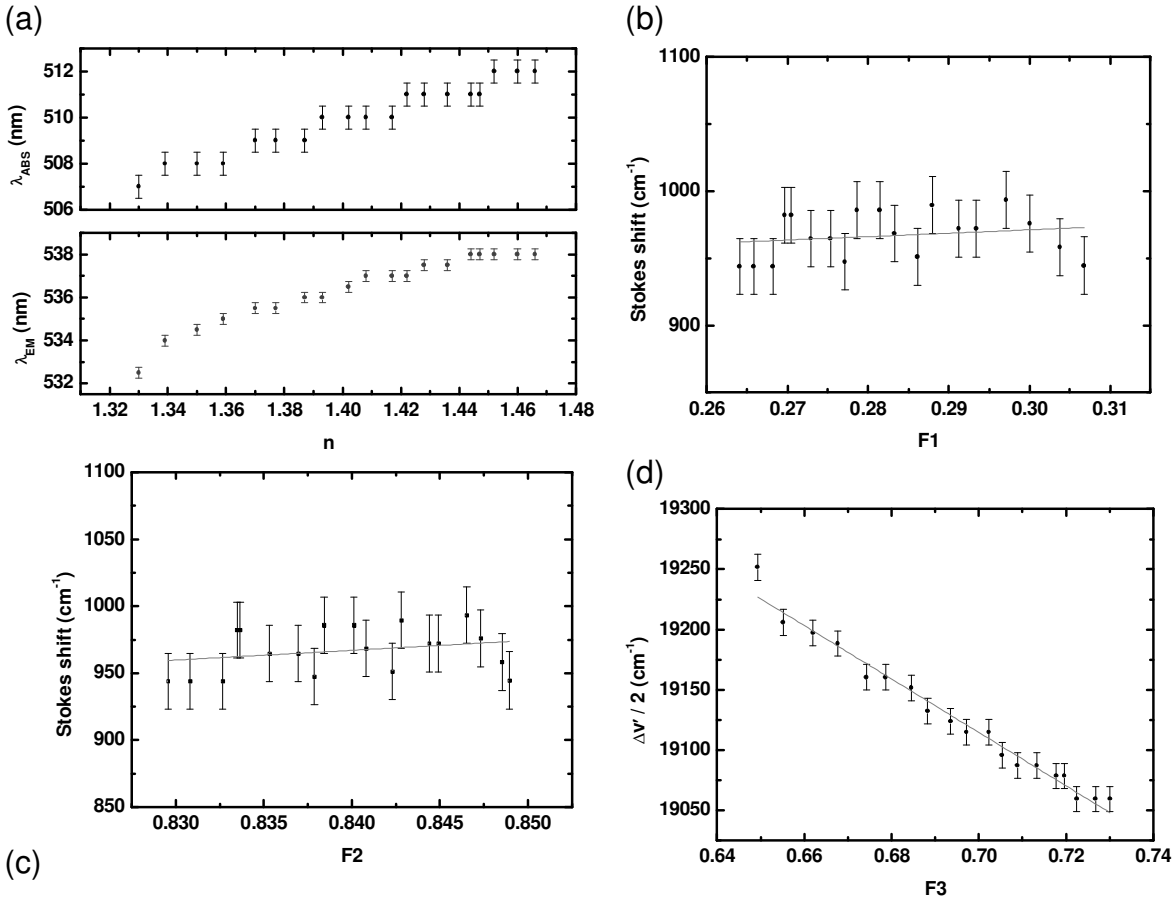

Figure 5.14 (a) Absorption and emission peaks of Rh123 in methanol/glycerol solutions. (b-d) The solvatochromic methods for Rh123 in methanol/glycerol mixtures.

5.5.2 Lifetime

The fluorescence decays of Rh123 in the solutions are shown in Figure 5.15. The lifetime information is extracted from the decay and shown in Table 5. 3. The lifetime of Rh123 in methanol is 3.98 ns, and it decreases when the refractive index increases.

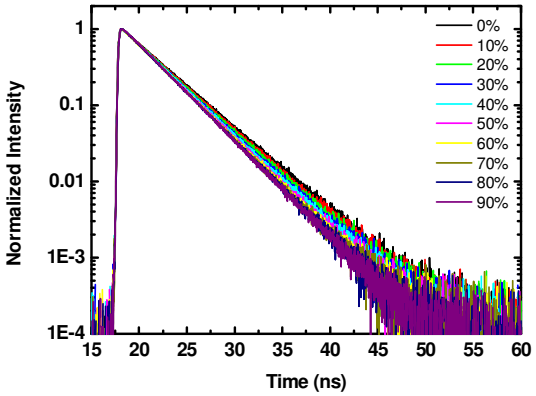

Figure 5.15 The fluorescence decay of Rh123 in methanol/glycerol mixtures. V/V glycerol is indicated.

Table 5. 3 Fluorescence lifetime and the refractive index of Rh123 in mixtures of glycerol and methanol.

Volume % of glycerol	Refractive index	τ_f (ns)
0	1.330	3.978 ± 0.003
5	1.339	3.913 ± 0.002
10	1.350	3.880 ± 0.003
15	1.359	3.826 ± 0.002
20	1.370	3.800 ± 0.003
25	1.377	3.731 ± 0.003
30	1.387	3.705 ± 0.003
35	1.393	3.670 ± 0.003
40	1.402	3.662 ± 0.002
45	1.408	3.610 ± 0.002
50	1.417	3.586 ± 0.002
55	1.422	3.556 ± 0.002
60	1.428	3.536 ± 0.002
65	1.436	3.513 ± 0.002
70	1.444	3.505 ± 0.002
75	1.447	3.491 ± 0.002
80	1.452	3.479 ± 0.003
85	1.460	3.470 ± 0.002
90	1.466	3.462 ± 0.002
95	1.468	3.436 ± 0.002

A plot of the inverse lifetime versus the squared refractive index of Rh123 is shown in Figure 5.16. The experimental results follow a straight line according to eq. 5.3. It has a little bend occurring at high containing glycerol solutions. These data points will be neglected for the fit. Hence, we used a straight line to fit the plot (Figure 5.16) which yield a gradient of $(1.13 \pm 0.02) \times 10^8$ s^{-1} with an intercept of $(5.05 \pm 0.38) \times 10^7$ s^{-1}. The intercept value means the non-radiative rate constant is almost the same among the solutions and the gradient value is k_{ro} based on eq. 5.3.

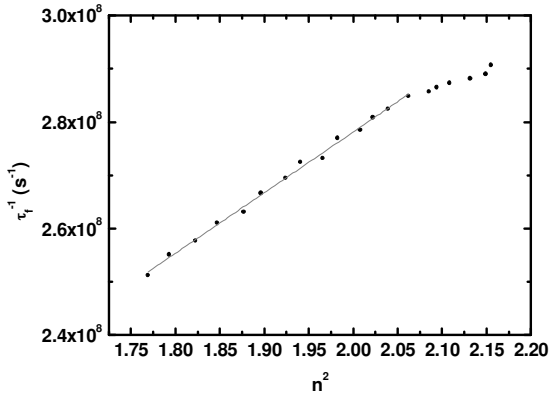

Figure 5.16 The inverse lifetime of Rh123 versus the quadratic refractive index of medium.

The radiative rate constant of Rh123 obtained from the experiment versus the squared refractive index is shown in Figure 5.17. The dashed line indicates a straight-line fit of the data points through the origin. The gradient is $(1.19 \pm 0.01) \times 10^8$ s^{-1}. The grey line is a straight-line fit with a non-zero intercept. The gradient is $(8.62 \pm 0.26) \times 10^7$ s^{-1} and an intercept is $(6.55 \pm 0.51) \times 10^7$ s^{-1}. A comparison of the gradient with the relevant term in the Strickler-Berg formula shows that $(1.510 \pm 0.002) \times 10^8$ s^{-1}. The difference of gradients between the experimental and theoretical methods are only approximately 20%, it could result from the errors of fluorescence quantum yield on the experimental results and variations of the extinction coefficient on the theoretical framework. If these effects are taking into account, the radiative rate constant measured experimentally agree with that calculated using the Strickler-Berg formula.

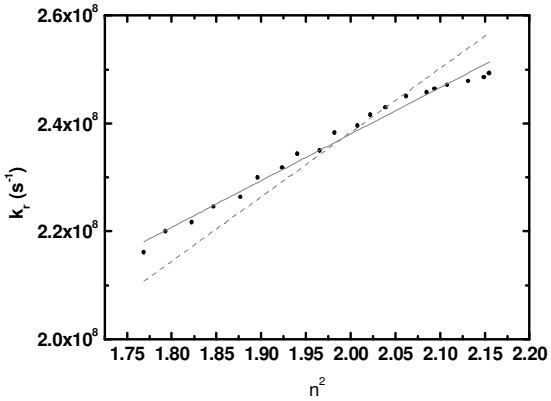

Figure 5.17 The radiative rate constant of Rh123 in the mixtures. A straight line through zero (grey dashed line), and the best fit for the data points (black line).

5.5.3 The Magnitude of the Electronic Transition Moment

Toptygin et al.'s model is used to describe the relationship between the radiative rate constant and the refractive index of Rh123 in methanol and glycerol mixtures. The results are depicted in Figure 5.18. It can be seen that the data follow a straight line according to the model. The values of P_1 and P_2 calculated from the gradient and the intercept of the plot are 6.428×10^{-3} $cm^{3/2}$ $s^{-1/2}$ and 0.4183, respectively. Hence, a value of $|\mu| = 8.09$ D and $L_\mu = 0.30 \pm 0.02$ are obtained. Thus, the intrinsic electronic transition dipole moment is 8.09 D along the longest axis of Rh123 molecule and its shape is ellipsoid.

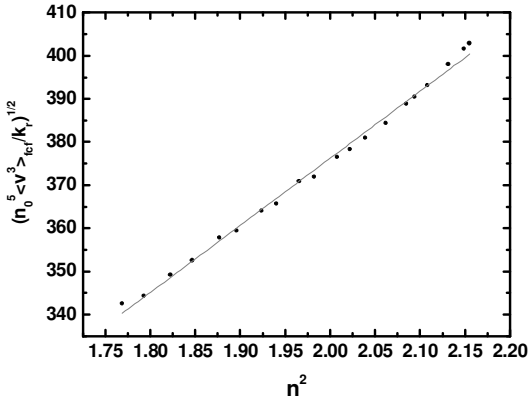

Figure 5.18 Relative variation to the radiative rate with the solvent refractive index for Rh123. The straight line represents the data following eq. 2.18. The gradient of this plot is 155.57 ± 2.49 $cm^{-3/2}$ $s^{1/2}$ and the intercept is 65.1 ± 4.9 $cm^{-3/2}$ $s^{1/2}$.

5.6 Nile red

Nile red has been reported that the fluorescent mechanism involves an intramolecular charge transfer state transition.[218-220] The polarity of the solvent varies the ground and the excited energy states resulting in fluorescence wavelength change. The fluorescence lifetime also varies with solvent. This molecule is very different to other three molecules studied so far, so we do not necessarily expect the theory to hold. However, we apply the theoretical framework to examine its behaviour and see how robust it is.

5.6.1 Absorption and Emission Spectra

The absorption and emission spectra of Nile red in various solutions were measured. The spectra of Nile red in mixtures with 10% and 90% glycerol are shown in Figure 5.19. A single emission peak appears in the polar solvent, which is consistent with results reported in the literature.[208] The band peaks have red shift when the polarity of the solution increases. The peak position versus the refractive index of solutions is shown in Figure 5.20(a). The wavelength of the absorption and emission peak increases with the refractive index, showing an energy level rearrangement of the dye molecules by the solvent molecules. The Stokes shift of Nile red versus the solvent polarity parameters is illustrated using different models, as shown in Figure 5.20(b-d).

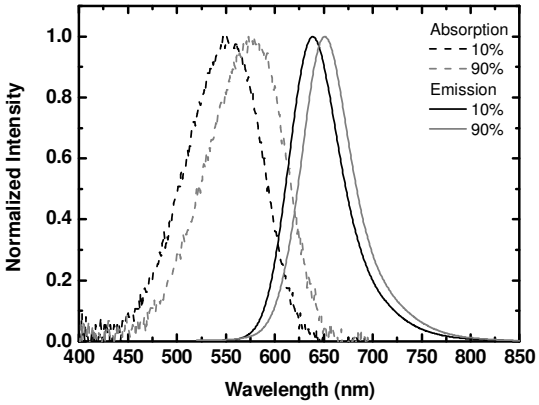

Figure 5.19 The absorption (dashed line) and emission spectra (solid line) of Nile red in the mixtures with volume percentage of 10% (black) and 90% glycerol (grey). The excitation wavelength for the emission spectra is 488 nm.

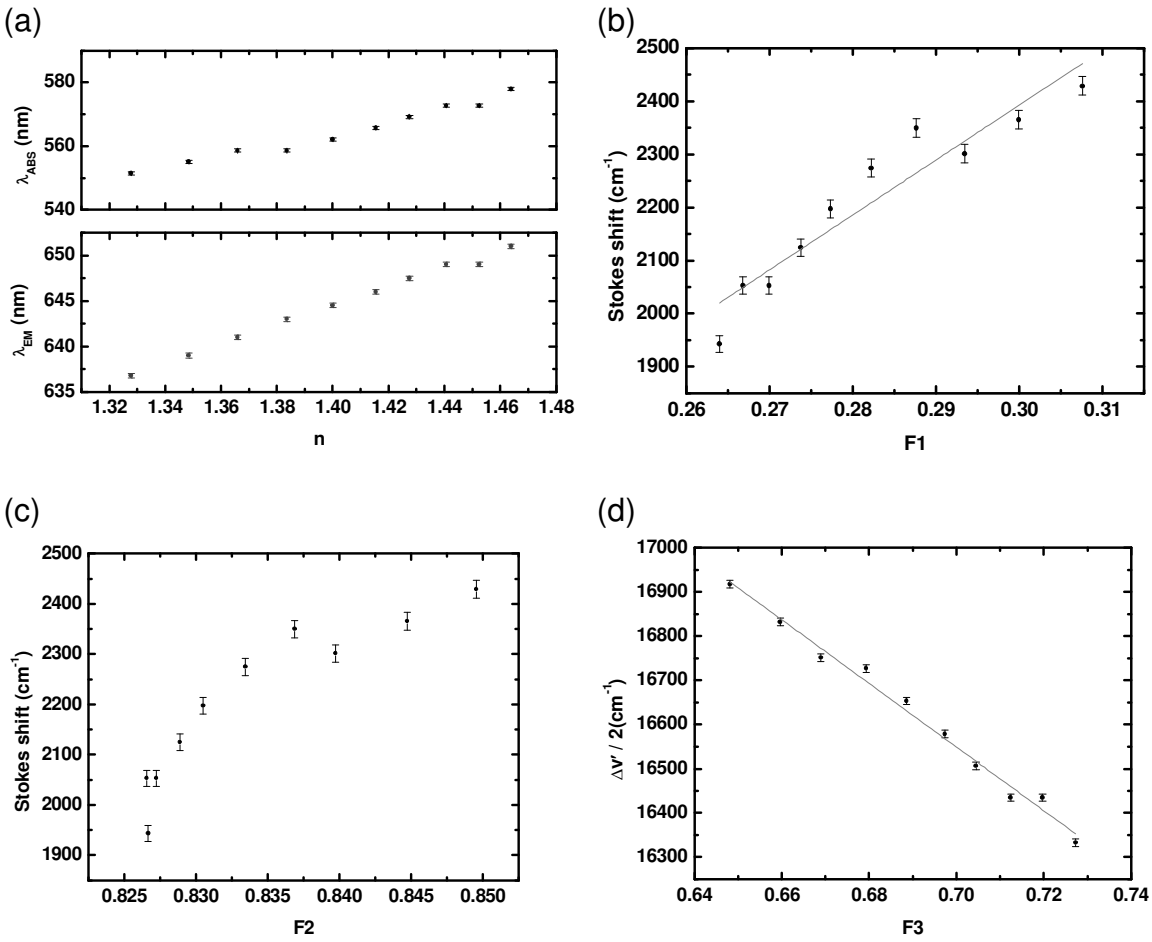

Figure 5.20 (a) Absorption and emission peaks of Nile red in methanol/glycerol mixtures. The solvatochromic methods for Nile red using (b) Lippert's equation, (c) Bakhshiev's equation, and (d) Kawski-Chamma-Viallet's equation.

According to eq. 2.21, a straight line is used to fit the data on the plot Figure 5.20(b), yielding a gradient of 1.03×10^4 cm^{-1}. The difference of dipole moments between the ground state and the excited state can be calculated to be 11.4 D by using a radius of 0.5 nm.[218] Eq. 2.23 fails to estimate the dipole moments of Nile red, i.e. a non-linear relationship between the Stokes shift and the polarity function. The plot of Figure 5.20(d) shows a linear negative function for variation of Stokes shift versus the polarity function ($F3$). The value of $\mu_e^2-\mu_g^2$ is 0.90 D^2 by using eq. 2.25 when a radius of 0.5 nm is used for this molecule.

The fluorescence quantum yield of Nile red in methanol is 0.22 and it decreases with an increase in polarity.[219] The fluorescence quantum yield of Nile red in the mixtures is calculated by comparison with that of methanol using eq. 3.2. The calculated fluorescence quantum yield of this fluorophore versus the refractive index of solutions is shown in Figure 5.21. The fluorescence quantum yield of Nile red decreases as the refractive index increases, which is in agreement with the literature. The fluorescence quantum yield behaviour of Nile red is different to that in Figure 5. 5. The fluorescence properties are listed in Table 5. 4.

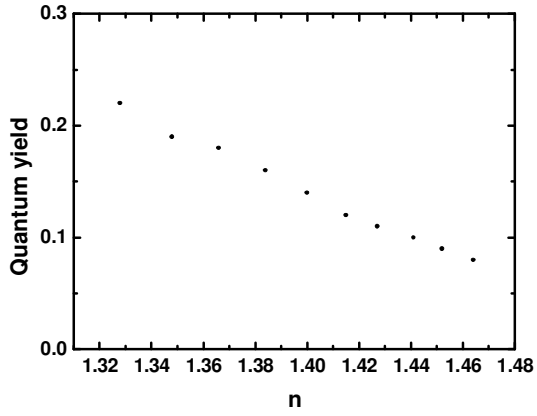

Figure 5.21 The fluorescence quantum yield of Nile red in methanol/glycerol mixtures with 0-90% of glycerol.

Table 5. 4 Fluorescence properties of Nile red in mixtures of glycerol and methanol.

Volume % of glycerol	Refractive index	Quantum yield	τ_f (ns) at 650 nm	k_r (10^7 s^{-1})	k_{nr} (10^8 s^{-1})
0	1.328	0.22	2.618 ± 0.002	8.40	2.98
10	1.348	0.19	2.509 ± 0.001	7.53	3.23
20	1.366	0.18	2.408 ± 0.002	7.33	3.42
30	1.384	0.16	2.377 ± 0.001	6.70	3.53
40	1.400	0.14	2.351 ± 0.001	6.06	3.65
50	1.415	0.12	2.341 ± 0.001	5.21	3.75
60	1.427	0.11	2.342 ± 0.001	4.75	3.80
70	1.441	0.10	2.336 ± 0.001	4.34	3.84
80	1.452	0.09	2.359 ± 0.001	3.70	3.87
90	1.464	0.08	2.363 ± 0.001	3.36	3.90

5.6.2 Lifetime

The fluorescence decays of Nile red in methanol/glycerol solutions is shown in Figure 5.22. A monoexponential decay function is used to fit the fluorescence decays, and the details are illustrated in Table 5. 4. The fluorescence lifetime of Nile red in methanol is 2.62 ns, and it decreases as the ratio of glycerol increases. It agrees with the work by Sarkar and his co-workers, in which the fluorescence quantum yield and fluorescence lifetime decreases with polarity.[219]

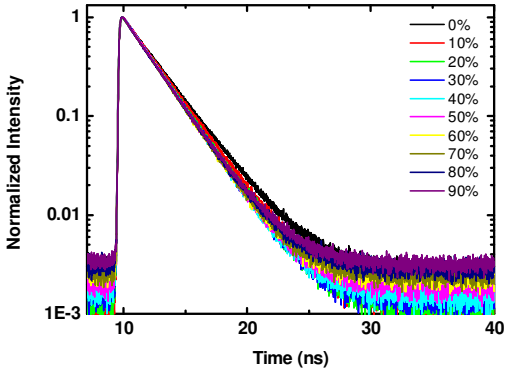

Figure 5.22 The fluorescence decay of Nile red in methanol/ glycerol mixtures with 0-90% of glycerol.

5.6.3 The Magnitude of the Electronic Transition Moment

The values of parameters from the emission spectra, fluorescence quantum yield, and fluorescence lifetime measurements for Nile red are fed into the eq. 2.18 as illustrated in Figure 5.23. The data does not follow a straight line well, and the intercept of a straight-line fit is negative. Therefore the model does not work for this molecule because L_μ should be between 0 and 1. The fluorescence process of Nile red is related to charge transfer mechanism, and involves different state. This could be the reason why the model is not working.

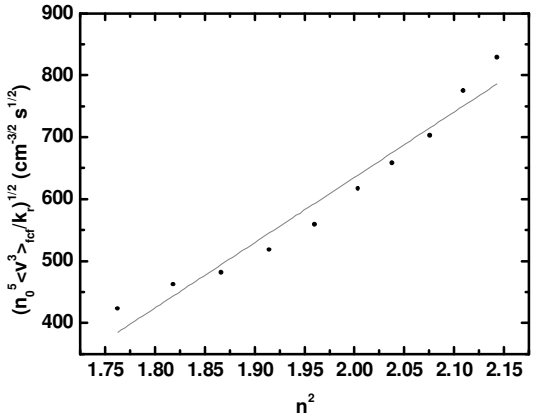

Figure 5.23 Relative variation of the radiative rate with the solvent refractive index for Nile red. The straight line represents the data following eq. 2.18. The gradient of this plot is 1054.06 ± 78.35 $cm^{-3/2}$ $s^{1/2}$ and the intercept is -1472.84 ± 78.35 $cm^{-3/2}$ $s^{1/2}$.

5.7 Summary

The excited-state dipole moments are greater than the ground-state dipole moments for Rh123, Nile red, PM546 and BODIPY-C_{12} in methanol and glycerol solutions based on the Kawski-Chamma-Viallet's formula (eq. 2.25). The electronic and geometrical structure of the molecule in the excited state can be obtained through the spectrum measurements and using the solvatochromic methods. Moreover, the Toptygin et al.'s model also offers more photophysical information of the fluorophores.

A summary of the dipole moments of all molecules is shown in Table 5. 5. The shape of the molecules can be revealed by Toptygin et al.'s model, except for Nile red. The radiative rate constant observed from the Strickler-Berg equation (eq. 2.11) is working for PM546, but not for Rh123 and BODIPY-C_{12}. Our results show that the transition dipole moment of PM546 estimated from Toptygin et al.'s equation is in agreement with the experimental results for PM546 and also other theoretical calculations for the related molecular structure molecule, TM-BODIPY. The Strickler-Berg equation could not deal with the transition dipole moment, but Toptygin et al.'s model can extract the information from time-resolved spectral spectroscopy.

Table 5. 5 The transition dipole moment of PM546, TM-BODIPY, BODIPY-C_{12}, Nile red and Rh123. The red colour denotes the results from solvatochromic method and the orange colour denotes the results from Toptygin et al.'s model.

	Radius (nm)	$\mu_e^2 - \mu_g^2$ (D^2)	μ_e (D)	μ_g (D)	$\lvert\mu\rvert$ (D)	L_μ
PM546	-	-5.13[195]	2.76[195]	3.57[195]	7.11 6.93[195, 209] 6.80[215]	0.191
TM-BODIPY	-	-3.24[212]	2.73[212]	3.27[212]	6.87[212]	
BODIPY-C_{12}	0.3	4.87			3.24	0.813
Nile red	0.5	0.90			-	-
Rh123	0.51[217]	0.30			8.09	0.295

Chapter 6

Conclusions and Future work

6.1 Conclusions

Intracellular viscosity changes have been reported to result in diseases.[110-113] We have discussed some fluorescence techniques using a novel fluorescent molecular rotor to map intracellular viscosity. The viscosity of cell environments can be measured using the fluorescent molecular rotor via FLIM and polarization-resolved fluorescence anisotropy. The advantages of these techniques allow us to measure the viscosity over the whole cells, rather than FRAP or FCS techniques which only can measure the viscosity in a small area. BODIPY-C_{12} offers longer fluorescence lifetimes compared to other fluorescent molecular rotors, such as DCVJ or CCVJ, which is useful in measuring viscosity via fluorescence lifetime measurements and in particular mapping the viscosity via FLIM. Moreover, fluorescence lifetime can distinguish between viscosity and concentration effects, but by intensity measurements alone, the concentration effect could not be discriminated. Fluorescence lifetime measurements are better than ratiometric method measurements because they are straight-forward and can be utilised in any setup for fluorescence lifetime measurement. For ratiometric measurements, all measurements should be carried out on the same instrument to avoid different calibrations due to the spectral sensitivities of detectors.

It has been demonstrated that the locations of BODIPY-C_{12} in cells are lipid droplets and the endoplasmic reticulum, and their environments are thus more viscous than the fluid phase of cytoplasm. The viscosity of lipid droplets may provide information on metabolism of lipids or other interaction related to lipids.

The heterogeneous environments can be reported via fluorescence lifetime of fluorescent molecular rotor or time-resolved fluorescence anisotropy decay. A dip-and-rise curve on time-resolved fluorescence anisotropy decay has been reported for a combination of fluorophores bound to an object and freely rotating fluorophores. The dip-and-rise anisotropy decay has not been reported using fluorescent molecular rotors.

In order to extend our knowledge on photophysical properties of fluorophores, we demonstrated that the transition dipole moment of some fluorophores can be obtained using Toptygin et al.'s model. However, it is not working for Nile red.

6.2 Future Work

FLIM has been used to distinguish normal healthy and cancer cells using the endogenous fluorophores. It would be interesting to measure the fluorescence lifetime of BODIPY-C_{12} in normal and cancer cells. The function of an organelle may be associated with fluorescence lifetime. The intracellular location of BODIPY-C_{12} is lipid droplets and ER. High-resolution microscopy may indicate the precise position. Moreover, incubation of cells with BODIPY-C_{12} and oleic acid can show whether BODIPY-C_{12} is in the lipid core or membrane of lipid droplets.

In section 4.5, the fluorescence lifetime and rotational correlation time of BODIPY-C_{12} in silicone oil has been demonstrated to fail to indicate viscosity. It would be interesting to measure BODIPY-C_{12} in higher viscosity silicone oils, in order to check the response of BODIPY-C_{12} to viscosity and to see whether it is in a low viscosity region or fails to the respond to viscosity altogether.

The fluorescence lifetime of BODIPY-C_{12} is associated with the viscosity of its environment, but not the polarity. However, Nile red is a polarity probe. The co-

localization of BODIPY-C_{12} and Nile red in cells has been demonstrated. A map of viscosity and polarity of the environment can be achieved by measuring either the fluorescence lifetime of two dyes or fluorescence lifetime of BODIPY-C_{12} combined with the emission spectrum of Nile red. Simultaneous measurement of the fluorescence lifetime of fluorescent molecular rotors and the emission spectrum of Nile red is possible because of their distinct emission spectra. The simultaneous measurements of FLIM and spectral ratiometric image have been reported achievable.[221] It provides a method to map the viscosity and the polarity of the dyes' environment simultaneously.

Cell preparation is mentioned in section 3.3.1. Fluorescence signal is through a 50:50 non-polarizing cube beamsplitter attached with two filters (FF01-514/30-25, Semrock and 600 IU 25, Comar) and recorded by two hybrid PMT detectors, simultaneously. The fluorescence images and FLIM of HeLa cells with two channels are shown in Figure 6.1. The emission wavelength at 496-532 nm is dominated by BODIPY-C_{12}, and the recorded emission wavelength at 580-620 nm is manly contributed to by Nile red. The emission peak and lifetime of Nile red varies with the polarity of its surroundings. It was found that there are at least two lifetimes of Nile red in cells as shown in Figure 6.1(c and d). To discriminate the lifetime of Nile red in the specific polarity is ambiguous in the detected window. It is because the lifetime of Nile red is not really linearly dependent on the polarity of the solvent. Hence, to measure the lifetime of BODIPY-C_{12} and the emission spectrum of Nile red may be a better method.

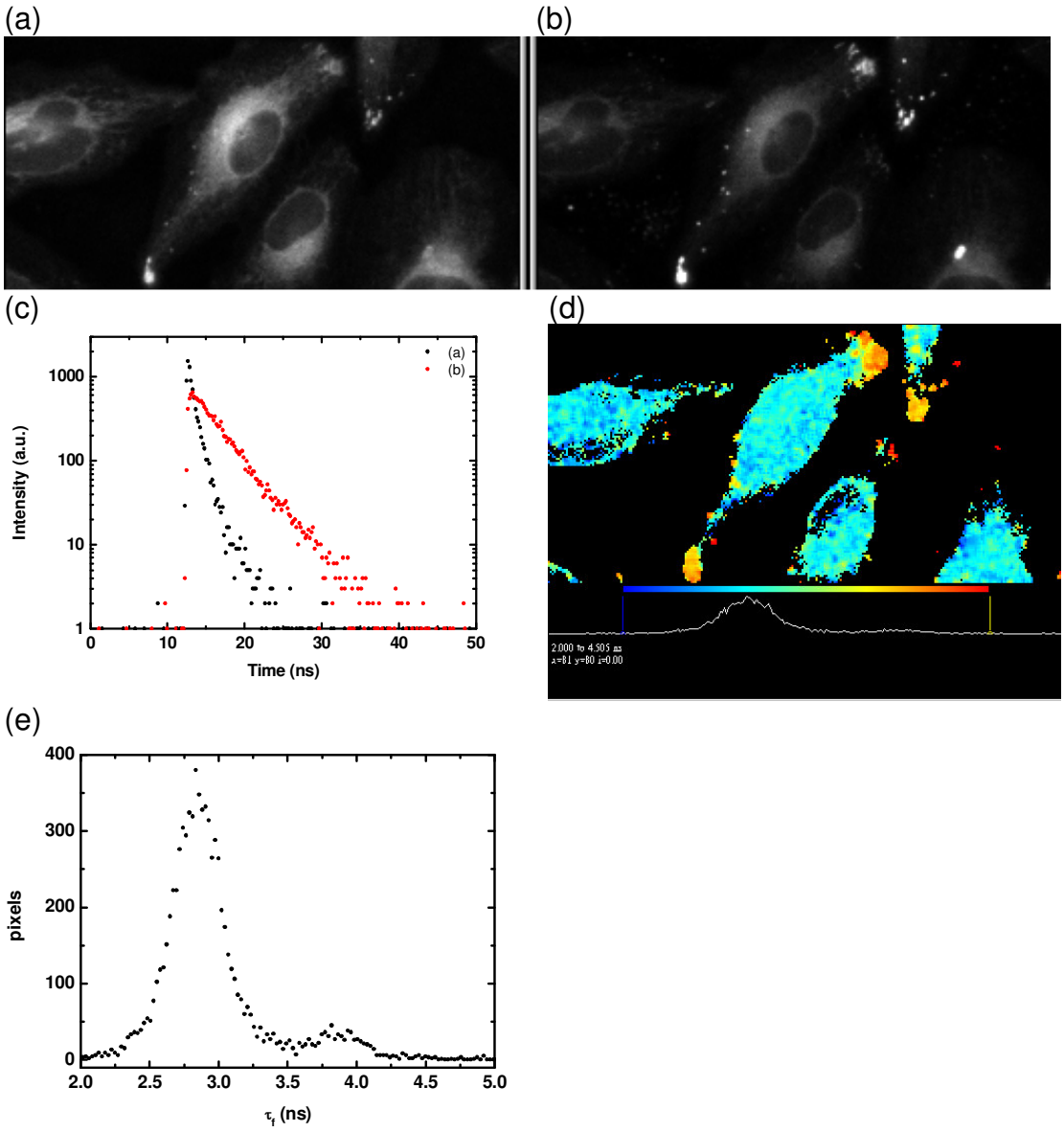

Figure 6.1 The confocal fluorescence intensity images of BODIPY-C_{12} and Nile red in HeLa cells at 37℃, recorded emission wavelength at (a) 496-532 nm and (b) 580-620 nm, simultaneously. (c) The fluorescence decays of (a: 496-532 nm, b: 580-620 nm) channels in a few pixels. (d) FLIM of the latter and (d) its histogram.

The viscosity is an important issue in biology, and BODIPY-C_{12} has been shown to be a candidate to measure the viscosity that is associated with membrane. It will be useful to modify the structure to become a water-soluble molecule or design it for a specific location. It could be used to study the lipid metabolism and to diagnose some lipid related diseases.

Appendix

The quantum yield of BODIPY-C_{12} in binary solutions of glycerol and methanol

The fluorescence quantum yield of an unknown fluorophore can be calculated using a relative method based on eq. 3.2. The integrated area of emission spectrum versus the absorbance of fluorescent molecule in the mixtures is illustrated in Figure A.1. The number in the figure denotes the volume fraction of glycerol for BODIPY-C_{12} in mixtures. Generally, a fluorophore with a high fluorescence quantum yield has higher emission intensity compared to the low quantum yield of the same concentration. The results show that the quantum yield of BODIPY-C_{12} in the solution with 90% of glycerol is higher than in the lower fraction of glycerol solution. The quantum yield of BODIPY-C_{12} being proportional to the viscosity of the solutions can be seen in Figure A.1 (a). Moreover, the quantum yield of fluorescein is much greater then BODIPY-C_{12} in all mixtures.

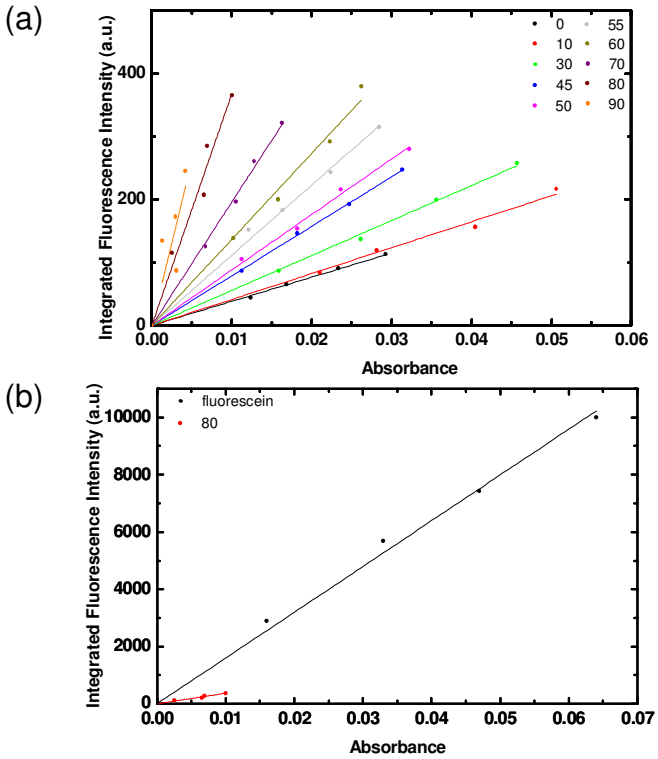

Figure A.1 The emission intensity versus absorbance of BODIPY-C_{12} in (a) methanol/glycerol mixtures and (b) methanol/glycerol solution with 80% of glycerol and fluorescein in 0.1M NaOH. The gradient is proportional to the fluorescence quantum yield.

A Lifetime and Time-Resolved Anisotropy of Fluorescein in Binary Solutions of Glycerol and NaOH

There is a dip-and-rise anisotropy decay for a fluorescent molecular rotor in a heterogeneous environment that has two complete viscosity environments. In order to compare the anisotropy behaviour, we carried out time-resolved fluorescence anisotropy measurement of a rigid molecule in the similar viscosity environment as BODIPY-C_{12} in the mixtures with 60% and 90% of glycerol in section 4.6. A constant concentration of fluorescein in the mixtures of NaOH/glycerol was prepared. The details of samples are illustrated in Table A. 1.

Table A. 1 Details of fluorescein solutions.

Volume % of glycerol		Viscosity (cP)	Refractive index	τ_f (ns)	θ (ns)
76.6%	2.3 ml of glycerol +0.7 ml of 0.1 M NaOH	66	1.4453	3.63	4.5
93.3%	2.8 ml of glycerol +0.2 ml of 0.1 M NaOH	656	1.4655	3.48	18.2

The fluorescence anisotropy decays are calculated using eq. 1.18 and the denominator of eq. 1.18 is fluorescence decay. We combined the fluorescence decay of two solutions of each polarization, and calculated the time-resolved fluorescence anisotropy decay using eq. 1.18. The fluorescence decays of fluorescein in mixtures with 76.6%, 93.3% of glycerol and the sum of decays are shown in Figure A.2, and the corresponding anisotropy decays are shown in Figure A.3. A monoexponential decay function is used to describe the fluorescence and anisotropy decays of fluorescein in individual solutions. It can be seen that there is a slight difference in lifetime due to refractive index effects according to eq. 2.11. From the time-resolved fluorescence measurement, the sum of fluorescence anisotropy decay of fluorescein does not have the similar curve as that of BODIPY-C_{12}, as expected. Indeed, it was found that a simple exponential decay function can be used to fit the anisotropy decay of fluorescence in the heterogeneous environment.

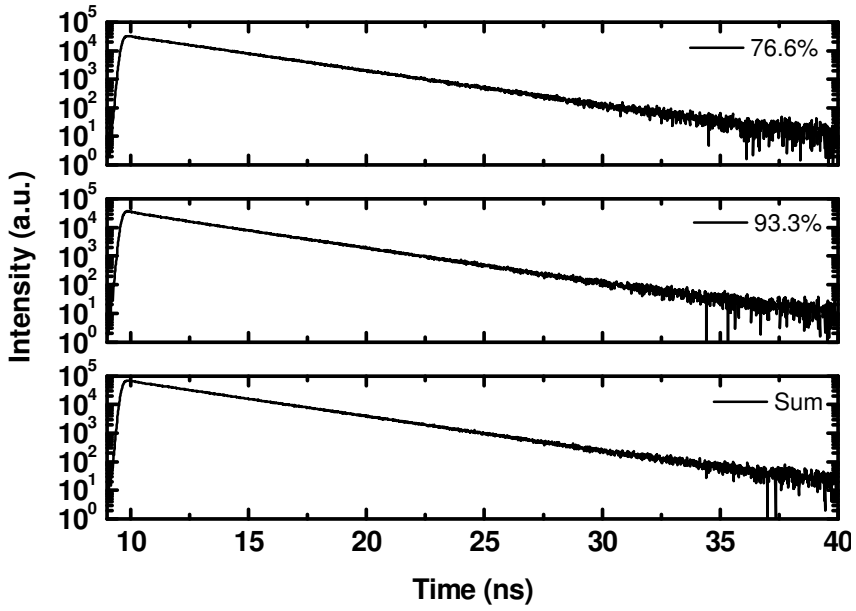

Figure A.2 Fluorescence decays of fluorescein in NaOH/glycerol mixtures. The numbers denote the volume fraction of glycerol.

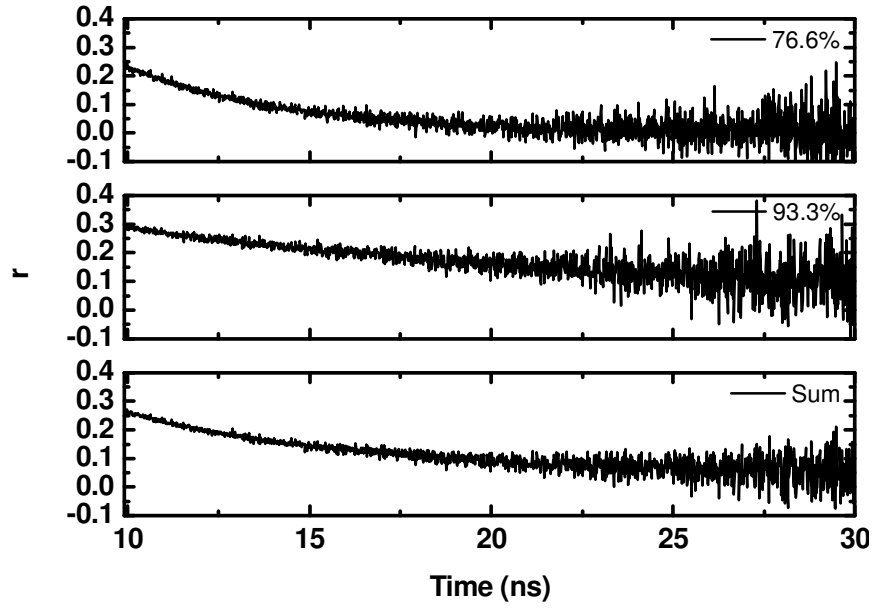

Figure A.3 Time-resolved fluorescence anisotropy decays of fluorescein in the mixtures. The numbers denote the volume fraction of glycerol.

The Depolarization Effect in Microscope

Eq. 1.18 is used to describe the polarization fluorescence carried out in a cuvette spectrometer, it means collimated linear polarized light is used to excite the fluorophore, and the fluorescence signal is collected in the parallel and perpendicular directions to the polarization of the incident light. If the time-resolved polarization fluorescence measurements are taken via a confocal fluorescence microscope, the electric field vector of the excitation light through an objective is not collimated due to depolarization effects. The depolarization effects also influence the fluorescence intensity. Therefore, eq. 1.18 has to be modified.

Here, Rh123 is used as a standard. Rh123 in methanol has a single fluorescence lifetime of 3.57 ns, and an initial anisotropy is 0.37 that measured using a cuvette spectrometer (FluoroCube, HORIBA). The value of r_0 obtained from the measurement is in agreement with the literature value.[196] The laser source is NanoLED-488L with a pulse duration less than 200 ps and a repetition rate of 1 MHz.

The time-resolved fluorescence anisotropy measurements of Rh123 is carried out via the confocal microscope using an excitation light with horizontal polarization, and the fluorescence signal is recorded using different NA objective lens and different pinhole size. First, an air objective lens is used, next a water immersion and then an oil immersion objective. A range of NA between 0.15 and 1.4 is used. The initial anisotropy versus cone half angle of objectives is shown in Figure A.4. The lifetime and anisotropy decays are calculated using eq. 1.18. It can be seen that fluorescence lifetimes are independent on NA of objectives and pinhole size. The anisotropy results show that the initial anisotropy value of Rh123 from 0.33-0.36 (NA=0.15) decreases to 0.28 (NA=1.4). The initial anisotropy does not vary with the pinhole size. The rotational correlation times have 20% of variation in the same NA objective lens. It is difficult to get the correlation between rotational correlation time and different NA. However, the rotational correlation time of Rh123 using an oil

immersion objective is lower than that using an air objective lens. It may result from the continuous heat of laser increasing the local viscosity of focus volume or it is due to the high NA.

The initial anisotropy of Rh123 varying with NA is obtained, and it can be used to estimate the initial anisotropy value of BODIPY-C_{12} in Chapter 4.

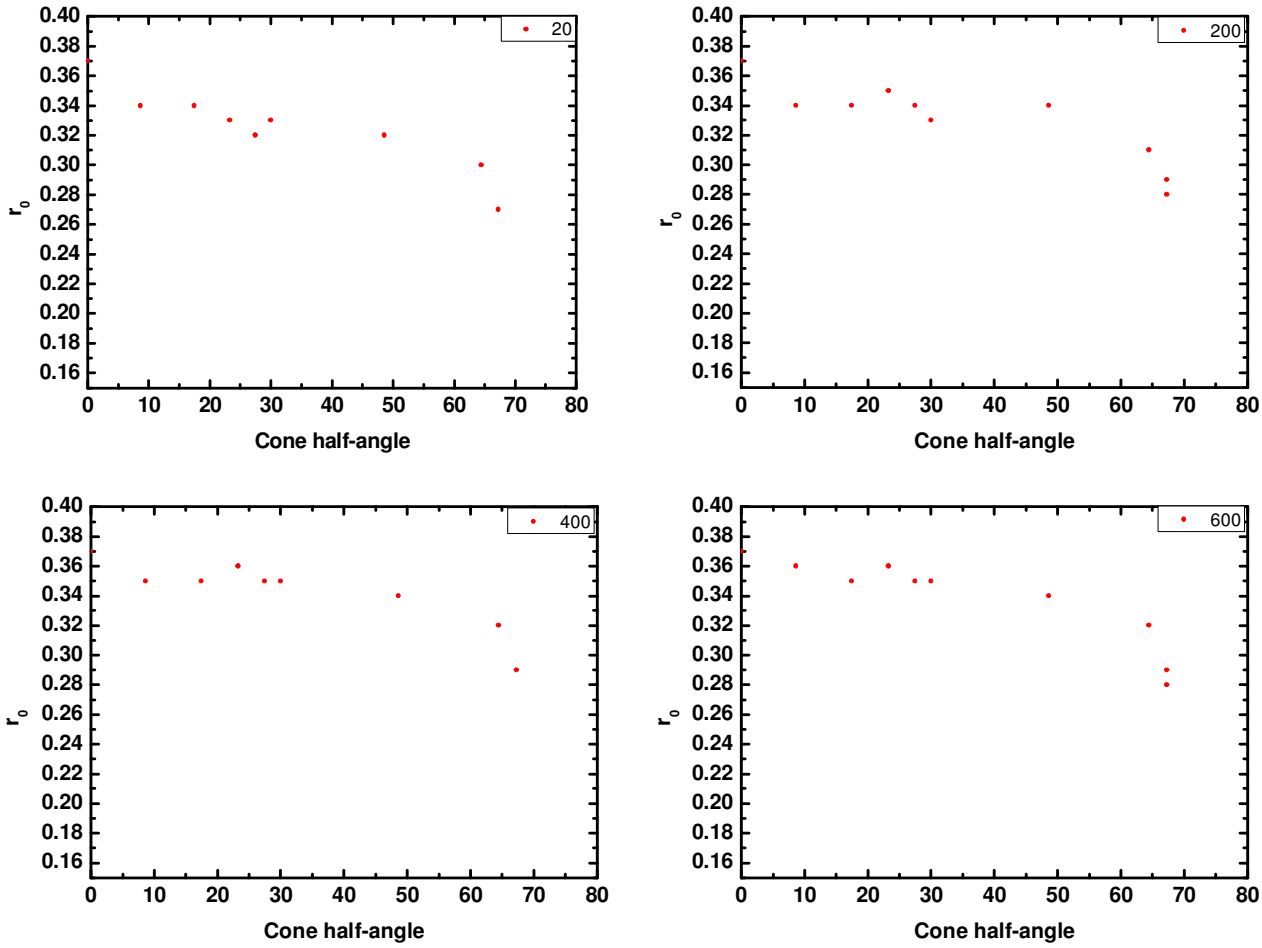

Figure A.4 Four representative relationships between initial anisotropy of Rh123 and cone half-angle of the microscope objective with a different confocal pinhole size. The number in each plot denotes the pinhole size.

Matlab code for Steady-State Fluorescence Anisotropy Mapping from Time-Resolved Fluorescence Anisotropy Decay

Steady-State Fluorescence Anisotropy mapping (pixel of time*x-axis*y-axis=256*256*128) from time-resolved fluorescence anisotropy decay data

Import the decay, and named it as “total”

```
channel_1=zeros(8388608,1);
channel_2=zeros(8388608,1);
for i=1:8388608,
 channel_1(i,1)=total(i,1);
 channel_2(i,1)=total(8388608+i,1);
end
para_range=rand(256,32768);
perp_range=rand(256,32768);
for i=1:256,
 for n=1:32768,
  para_range(i,n)=channel_2(256*(n-1)+i,1);
  perp_range(i,n)=channel_1(256*(n-1)+i,1);
 end
end
para_range(1:21,:)=zeros;
para_range(218:256,:)=zeros;
perp_range(1:21,:)=zeros;
perp_range(218:256,:)=zeros;
```

```
sum_para1=sum(para_range);

sum_perp1=sum(perp_range);

total=sum_para1+2*0.93*sum_perp1;

total1=total;

total1(total<600)=inf;

r_range=(sum_para1-0.93*sum_perp1)./total1;

r_range_matrix=zeros(128,256);

for i=1:256,

 for n=1:127,

  r_range_matrix(i,n)=r_range(1,256*(n-1)+i);

 end

end

save r_range_matrix.txt r_range_matrix –ascii
```

References

1. Lakowicz, J. R., Principles of Fluorescence Spectroscopy, Third Edition. *Springer, New York* **2006**.
2. Stokes, G. G., On the Change of Refrangibility of Light. *Philos. Trans. R. Soc. London* **1852,** *142*, 463-562.
3. Jabłoński, A., Über den Mechanismus der Photolumineszenz von Farbstoffphosphoren. *Z. Physik* **1935,** *94*, 38-46.
4. Lewis, G. N.; Lipkin, D.; Magel, T. T., Reversible Photochemical Processes in Rigid Media. A Study of the Phosphorescent State. *J. Am. Chem. Soc.* **1941,** *63*, 3055-3018.
5. Kasha, M., From Jabłoński to femtoseconds evolution of molecular photophysics. *Acta Phys. Polon. A* **1999,** *95*, 15-36.
6. Kasap, S. O., Optoelectronics and Photonics: Principles and Practices. *Prentice Hall* **2001**.
7. Kasha, M., Characterization of electronic transitions in complex molecules. *Disc. Faraday Soc.* **1950,** *9*, 14.
8. Zhang, Y.; Aslan, K.; Previte, M. J. R.; Geddes, C. D., Metal-enhanced fluorescence from paper substrates: Modified spectral properties of dyes for potential high-throughput surface analysis and assays and as an anti-counterfeiting technology. *Dyes Pigm.* **2008,** *77* (3), 545-549.
9. Rosenthal, C. K., Invention of the microscope. *Nat. Milestones in Light Microscopy* **2009,** *Milestone 1*.
10. Suhling, K., Fluorescence lifetime imaging, in Methods Express, Cell Imaging (ed D. Stephens), chapter 11, Scion Publishing, Bloxham **2006**, 219-245.
11. Claxton, N. S.; Fellers, T. J.; Davidson, M. W., Laser Scanning Confocal Microscopy, http://www.olympusfluoview.com/theory/LSCMIntro.pdf. **Last visited on 15 February, 2012**.
12. MICROSCOPYU, N., http://www.microscopyu.com/articles/formulas/formulasresolution.html Resolution.
13. Huang, B.; Bates, M.; Zhuang, X., Super-Resolution Fluorescence Microscopy. *Annu. Rev. Biochem.* **2009,** *78* (1), 993-1016.
14. Berezin, M. Y.; Achilefu, S., Fluorescence Lifetime Measurements and Biological Imaging. *Chem. Rev.* **2010,** *110*, 2641-2684.
15. Levitt, J. A.; Matthews, D. R.; Ameer-Beg, S. M.; Suhling, K., Fluorescence lifetime and polarization-resolved imaging in cell biology. *Curr. Opin. Biotechnol.* **2009,** *20* (1), 28-36.
16. Suhling, K.; French, P. M. W.; Phillips, D., Time-resolved fluorescence microscopy. *Photochem. Photobiol. Sci.* **2005,** *4* (1), 13-22.
17. Ma, L., A long lifetime chemical sensor: study on fluorescence property of fluorescein isothiocyanate and preparation of pH chemical sensor. *Spectrochim. Acta Part A* **2004,** *60* (8-9), 1865-1872.
18. Hammer, M.; Schweitzer, D.; Richter, S.; Königsdörffer, E., Sodium fluorescein as a retinal pH indicator? *Physiol. Meas.* **2005,** *26* (4), N9-N12.
19. Hanson, K. M.; Behne, M. J.; Barry, N. P.; Mauro, T. M.; Gratton, E.; Clegg, a. R. M., Two-Photon Fluorescence Lifetime Imaging of the Skin Stratum Corneum pH Gradient. *Biophys. J.* **2002,** *83*, 1682-1690.

20. Babcock, D. F., Examination of the Intracellular Ionic Environment and of Ionophore Action by Null Point Measurements Employing the Fluorescein Chromophore. *J. Biol. Chem.* **1983,** *258*, 6380-6389.
21. Biskup, C.; Zimmer, T.; Benndorf, K., FRET between cardiac Na+ channel subunits measured with a confocal microscope and a streak camera. *Nat. Biotechnol.* **2004,** *22* (2), 220-224.
22. Gensch, T.; Komolov, K. E.; Senin, I. I.; Philippov, P. P.; Koch, K.-W., Ca2+-dependent conformational changes in the neuronal Ca2+-sensor recoverin probed by the fluorescent dye Alexa647. *Proteins: Structure, Function, and Bioinformatics* **2006,** *66* (2), 492-499.
23. Hötzer, B.; Ivanov, R.; Brumbarova, T.; Bauer, P.; Jung, G., Visualization of Cu2+ uptake and release in plant cells by fluorescence lifetime imaging microscopy. *FEBS Journal* **2011**, no-no.
24. Gerritsen, H. C.; Sanders, R.; Draaijer, A.; Ince, C.; Levine, Y. K., Fluorescence Lifetime Imaging of Oxygen in Living Cells. *J. Fluoresc.* **1997,** *7*, 11-15.
25. Ribou, A.-C.; Vigo, J.; Salmon, J.-M., Lifetime of Fluorescent Pyrene Butyric Acid Probe in Single Living Cells for Measurement of Oxygen Fluctuation. *photochem. Photobiol.* **2004,** *80*, 274-280.
26. Collins, S. F.; Baxter, G. W.; Wade, S. A.; Sun, T.; Grattan, K. T. V.; Zhang, Z. Y.; Palmer, A. W., Comparison of fluorescence-based temperature sensor schemes: Theoretical analysis and experimental validation. *J. Appl. Phys.* **1998,** *84* (9), 4649-4654.
27. Vetrone, F.; Naccache, R.; Zamarron, A.; Fuente, A. J. d. l.; Sanz-Rodriguez, F.; Maestro, L. M.; Rodriguez, E. M.; Jaque, D.; Sole, J. G.; Capobianco, J. A., Temperature Sensing Using Fluorescent Nanothermometers. *ACS Nano* **2010,** *4*, 3254-3258.
28. Skala, M. C.; Riching, K. M.; Gendron-Fitzpatrick, A.; Eickhoff, J.; Eliceiri, K. W.; White, J. G.; Ramanujam, N., In vivo multiphoton microscopy of NADH and FAD redox states, fluorescence lifetimes, and cellular morphology in precancerous epithelia. *Proc. Natl. Acad. Sci. U.S.A.* **2007,** *104* (49), 19494-19499.
29. Galletly, N. P.; McGinty, J.; Dunsby, C.; Teixeira, F.; Requejo-Isidro, J.; Munro, I.; Elson, D. S.; Neil, M. A. A.; Chu, A. C.; French, P. M. W.; Stamp, G. W., Fluorescence lifetime imaging distinguishes basal cell carcinoma from surrounding uninvolved skin. *Br. J. Dermatol.* **2008,** *159* (1), 152-161.
30. Elson, D. S.; Jo, J. A.; Marcu, L., Miniaturized side-viewing imaging probe for fluorescence lifetime imaging (FLIM): validation with fluorescence dyes, tissue structural proteins and tissue specimens. *New J. Phys.* **2007,** *9* (5), 127-127.
31. McConnell, G.; Girkin, J. M.; Ameer-Beg, S. M.; Barber, P. R.; Vojnovic, B.; NG, T.; Banerjee, A.; Watson, T. F.; Cook, R. J., Time-correlated single-photon counting fluorescence lifetime confocal imaging of decayed and sound dental structures with a white-light supercontinuum source. *J. Microsc.* **2007,** *225*, 126-136.
32. Schweitzer, D.; Schenke, S.; Hammer, M.; Schweitzer, F.; Jentsch, S.; Birckner, E.; Becker, W.; Bergmann, A., Towards metabolic mapping of the human retina. *Microsc. Res. Tech.* **2007,** *70* (5), 410-419.
33. Comelli, D.; Valentini, G.; Cubeddu, R.; Toniolo, L., Fluorescence lifetime imaging and Fourier transform infrared spectroscopy of Michelangelo's David. *Appl. Spectrosc.* **2005,** *59* (9), 1174-1181.

34. Holmes, J. W., The Relevance of Pressure-Sensitive Paint to Aerodynamic Research. *J. Fluoresc.* **1993,** *3*, 179-183.
35. Seah, L. K.; Dinish, U. S.; Phang, W. F.; Chao, Z. X.; Murukeshan, V. M., Fluorescence optimisation and lifetime studies of fingerprints treated with magnetic powders. *Forensic Sci. Int.* **2005,** *152* (2-3), 249-257.
36. Rusk, N., The fluorescence microscope. *Nat. Milestones in Light Microscopy* **2009,** *Milestone 4*.
37. Minsky, M., Memoir on inventing the confocal scanning microscope. *Scanning* **1988,** *10* (4), 128-138.
38. Amos, W. B.; White, J. G., How the Confocal Laser Scanning Microscope entered Biological Research. *Biol. Cell* **2003,** *95* (6), 335-342.
39. Pierce, S. K.; Liu, W., The tipping points in the initiation of B cell signalling: how small changes make big differences. *Nat. Rev. Immunol.* **2010,** *10* (11), 767-777.
40. Schermelleh, L.; Heintzmann, R.; Leonhardt, H., A guide to super-resolution fluorescence microscopy. *J. Cell Biol.* **2010,** *190* (2), 165-175.
41. Vicidomini, G.; Schmidt, R.; Egner, A.; Hell, S. W.; Schönle, A., Automatic deconvolution in 4Pi-microscopy with variable phase. *Opt. Express* **2010,** *18*, 10154-10167.
42. Gustafsson, M. G. L., Nonlinear structured-illumination microscopy: Wide-field fluorescence imaging with theoretically unlimited resolution. *Proceedings of the National Academy of Sciences* **2005,** *102* (37), 13081-13086.
43. Westphal, V.; Hell, S. W., Nanoscale Resolution in the Focal Plane of an Optical Microscope. *Phys. Rev. Lett.* **2005,** *94* (14), 143903.
44. Rittweger, E.; Han, K. Y.; Irvine, S. E.; Eggeling, C.; Hell, S. W., STED microscopy reveals crystal colour centres with nanometric resolution. *Nat. Photonics* **2009,** *3* (3), 144-147.
45. Bates, M.; Huang, B.; Dempsey, G. T.; Zhuang, X., Multicolor Super-Resolution Imaging with Photo-Switchable Fluorescent Probes. *Science* **2007,** *317* (5845), 1749-1753.
46. Jones, S. A.; Shim, S.-H.; He, J.; Zhuang, X., Fast, three-dimensional super-resolution imaging of live cells. *Nat. Methods* **2011,** *8* (6), 499-505.
47. Rust, M. J.; Bates, M.; Zhuang, X., Sub-diffraction-limit imaging by stochastic optical reconstruction microscopy (STORM). *Nat. Methods* **2006,** *3* (10), 793-796.
48. Cox, S.; Rosten, E.; Monypenny, J.; Jovanovic-Talisman, T.; Burnette, D. T.; Lippincott-Schwartz, J.; Jones, G. E.; Heintzmann, R., Bayesian localization microscopy reveals nanoscale podosome dynamics. *Nat. Methods* **2011,** *9* (2), 195-200.
49. Scheuring, S.; Boudier, T.; Sturgis, J. N., From high-resolution AFM topographs to atomic models of supramolecular assemblies. *J. Struct. Biol.* **2007,** *159* (2), 268-276.
50. Auksorius, E.; Boruah, B. R.; Dunsby, C.; Lanigan, P. M. P.; Kennedy, G.; Neil, M. A. A.; French, P. M. W., Stimulated emission depletion microscopy with a supercontinuum source and fluorescence lifetime imaging. *Opt. Lett.* **2008,** *33* (2), 113-115.
51. Axelrod, D.; Koppel, D. E.; Schlessinger, J.; Elson, E.; Webb, W. W., Mobility Measurement by Analysis of Fluorescence Photobleaching Recovery Kinetics. *Biophys. J.* **1976,** *16*, 1055-1069.
52. Kappel, C.; Eils, R., Fluorescence recovery after photobleaching with the Leica TCS SP2. *Confocal Application Letter* **2004,** *18*, 1-12.

53. Visser, A. J. W. G.; Hink, M. A., New Perspectives of Fluorescence Correlation Spectroscopy. *J. Fluoresc.* **1999,** *9*, 81-87.
54. Levin, M. K.; Carson, J. H., Fluorescence correlation spectroscopy and quantitative cell biology. *Differentiation* **2004,** *72*, 1-10.
55. Kim, S. A.; Heinze, K. G.; Schwille, P., Fluorescence correlation spectroscopy in living cells. *Nat. Methods* **2007,** *4* (11), 963-973.
56. Elson, Elliot L., Fluorescence Correlation Spectroscopy: Past, Present, Future. *Biophys. J.* **2011,** *101* (12), 2855-2870.
57. García-Sáez, A. J.; Schwille, P., Fluorescence correlation spectroscopy for the study of membrane dynamics and protein/lipid interactions. *Methods* **2008,** *46* (2), 116-122.
58. Festy, F.; Ameer-Beg, S. M.; Ng, T.; Suhling, K., Imaging proteins in vivo using fluorescence lifetime microscopy. *Mol. BioSyst.* **2007,** *3* (6), 381-391.
59. Förster, T., Energiewanderung und Fluoreszenz, *Naturwiss* **1946,** 33(6), 166-175; English translation by K. Suhling, Energy migration and fluorescence. *J. Biomed. Opt.* **2012,** *17* (1), 011002.
60. Valeur, B., Molecular Fluorescence. *Wiley-VCH, Weinheim* **2002**.
61. Wahl, P., Aanlysis of Fluorescence Anisotropy Decays by a Least Square Method. *Biophys. Chem.* **1979,** *10*, 91-104.
62. Rachofsky, E. L.; Wolf, B.; Bialik, C. N.; Ross, J. B. A.; Laws, W. R., A General Method for Constrained Analysis of Fluorescence Anisotropy Decay: Application of the Steady-State Anisotropy. *J. Fluoresc.* **1999,** *9*, 379-390.
63. Gryczynski, I.; Malak, H.; Lakowicz, J. R., Three-photon induced fluorescence of 2,5-diphenyloxazole with a femtosecond Ti:sapphire laser. *Chem. Phys. Lett.* **1995,** *245*, 30-35.
64. Birch, D. J. S., Multiphoton excited fluorescence spectroscopy of biomolecular systems. *Spectrochim. Acta Part A* **2001,** *57*, 2313-2336.
65. Vogel, S. S.; Thaler, C.; Blank, P. S.; Koushik, S. V., Time-resolved fluorescence anisotropy. In FLIM Microscopy in Biology and Medicine (eds. Periasamy, A. & Clegg, R.M.) 245-288 (CRC Press, 2009).
66. Axelrod, D., Carbocynine dye orientation in red cell membrane studied by microscopic fluorescence polarization. *Biophys. J.* **1979,** *26*, 557-573.
67. Axelrod, D., Fluorescence Polarization Microscopy. *Meth. Cell Biol.* **1989,** *30*, 333-352.
68. Ha, T.; Laurence, T. A.; Chemla, D. S.; Weiss, S., Polarization Spectroscopy of Single Fluorescent Molecules. *J. Phys. Chem. B* **1999,** *103*, 6839-6850.
69. Bahlmann, K.; Hell, S. W., Depolarization by high aperture focusing. *Appl. Phys. Lett.* **2000,** *77* (5), 612-614.
70. Fisz, J. J., Fluorescence Polarization Spectroscopy at Combined High-Aperture Excitation and Detection: Application to One-Photon-Excitation Fluorescence Microscopy. *J. Phys. Chem. A* **2007,** *111* (35), 8606-8621.
71. Fisz, J. J., Another Treatment of Fluorescence Polarization Microspectroscopy and Imaging. *J. Phys. Chem. A* **2009,** *113* (15), 3505-3516.
72. Siegel, J.; Suhling, K.; Lévêque-Fort, S.; Webb, S. E. D.; Davis, D. M.; Phillips, D.; Sabharwal, Y.; French, P. M. W., Wide-field time-resolved fluorescence anisotropy imaging (TR-FAIM): Imaging the rotational mobility of a fluorophore. *Rev. Sci. Instrum.* **2003,** *74* (1), 182.
73. Sharma, P.; Brown, S.; Walter, G.; Santra, S.; Moudgil, B., Nanoparticles for bioimaging. *Adv. Colloid Interface Sci.* **2006,** *123-126*, 471-485.
74. Bacskai, B. J.; Skoch, J.; Hickey, G. A.; Allen, R.; Hyman, B. T., Fluorescence resonance energy transfer determinations using multiphoton

fluorescence lifetime imaging microscopy to characterize amyloid-beta plaques. *J. Biomed. Opt.* **2003,** *8* (3), 368-375.
75. McCann, F. E.; Suhling, K.; Carlin, L. M.; Eleme, K.; Taner, S. B.; Yanagi, K.; Vanherberghen, B.; French, P. M. W.; Davis, D. M., Imaging immune surveillance by T cells and NK cells. *Immunol. Rev.* **2002,** *189*, 179-192.
76. Chalfie, M.; Tu, Y.; Euskirchen, G.; Ward, W.; Prasher, D., Green fluorescent protein as a marker for gene expression. *Science* **1994,** *263*, 802-805.
77. Tregidgo, C.; Levitt, J. A.; Suhling, K., Effect of refractive index on the fluorescence lifetime of green fluorescent protein. *J. Biomed. Opt.* **2008,** *13* (3), 031218.
78. Manen, H.-J. v.; Verkuijlen, P.; Wittendorp, P.; Subramaniam, V.; Berg, T. K. v. d.; Roos, D.; Otto, C., Refractive Index Sensing of Green Fluorescent Proteins in Living Cells Using Fluorescence Lifetime Imaging Microscopy. *Biophys. J.* **2008,** *94* (8), L67-L69.
79. Baker, B. J.; Mutoh, H.; Dimitrov, D.; Akemann, W.; Perron, A.; Iwamoto, Y.; Jin, L.; Cohen, L. B.; Isacoff, E. Y.; Pieribone, V. A.; Hughes, T.; Knöpfel, T., Genetically encoded fluorescent sensors of membrane potential. *Brain Cell Biology* **2008,** *36* (1-4), 53-67.
80. Rumbaut, R. E.; Sial, A. J., Differential Phototoxicity of Fluorescent Dye-Labeled Albumin Conjugates. *Microcirulation* **1999,** *6*, 205-213.
81. Waldo, G. S.; Standish, B. M.; Berendzen, J.; Terwilliger, T. C., Rapid protein-folding assay using green fluorescent protein. *Nat. Biotechnol.* **1999,** *17*, 691-695.
82. Selvin, P. R., The renaissance of fluorescence resonance energy transfer. *Nat. Struct. Biol.* **2000,** *7*, 730-734.
83. Müller-Taubenberger, A.; Anderson, K. I., Recent advances using green and red fluorescent protein variants. *Applied Microbiology and Biotechnology* **2007,** *77* (1), 1-12.
84. Gather, M. C.; Yun, S. H., Single-cell biological lasers. *Nat. Photonics* **2011,** *5*, 406-410.
85. Yang, F.; Moss, L. G.; George N. Phillips, J., The molecular structure of green fluorescent protein. *Nat. Biotechnol.* **1996,** *14*, 1246-1251.
86. Algar, W. R.; Tavares, A. J.; Krull, U. J., Beyond labels: A review of the application of quantum dots as integrated components of assays, bioprobes, and biosensors utilizing optical transduction. *Anal. Chim. Acta* **2010,** *673* (1), 1-25.
87. Gao, X.; Cui, Y.; Levenson, R. M.; Chung, L. W. K.; Nie, S., In vivo cancer targeting and imaging with semiconductor quantum dots. *Nat. Biotechnol.* **2004,** *22* (8), 969-976.
88. Ballou, B.; Lagerholm, B. C.; Ernst, L. A.; Bruchez, M. P.; Waggoner, A. S., Noninvasive Imaging of Quantum Dots in Mice. *Bioconjugate Chem.* **2004,** *15*, 79-86.
89. Hardman, R., A Toxicologic Review of Quantum Dots: Toxicity Depends on Physicochemical and Environmental Factors. *Environ. Health Perspect.* **2006,** *114* (2), 165-172.
90. Suhling, K.; Siegel, J.; Lanigan, P. M. P.; Lévêque-Fort, S.; Webb, S. E. D.; Phillips, D.; Davis, D. M.; French, P. M. W., Time-resolved fluorescence anisotropy imaging applied to live cells. *Opt. Lett.* **2004,** *29*, 584-586.
91. Corti, H. R.; Frank, G. A.; Marconi, M. C., An Alternate Solution of Fluorescence Recovery Kinetics after Spot-Bleaching for Measuring Diffusion

Coefficients. 2. Diffusion of Fluorescein in Aqueous Sucrose Solutions. *J. Solution Chem.* **2008,** *37* (11), 1593-1608.
92. Lavis, L. D.; Raines, R. T., Bright Ideas for Chemical Biology. *ACS Chem. Biol.* **2008,** *3*, 142-155.
93. Kee, H. L.; Kirmaier, C.; Yu, L.; Thamyongkit, P.; Youngblood, W. J.; Calder, M. E.; Ramos, L.; Noll, B. C.; Bocian, D. F.; Scheidt, W. R.; Birge, R. R.; Lindsey, J. S.; Holten, D., Structural Control of the Photodynamics of Boron-Dipyrrin Complexes. *J. Phys. Chem. B* **2005,** *109*, 20433-20443.
94. Haidekker, M. A.; Brady, T. P.; Lichlyter, D.; Theodorakis, E. A., Effects of solvent polarity and solvent viscosity on the fluorescent properties of molecular rotors and related probes. *Bioorganic Chemistry* **2005,** *33* (6), 415-425.
95. Zhu, L.-L.; Li, X.; Ji, F.-Y.; Ma, X.; Wang, Q.-C.; Tian, H., Photolockable Ratiometric Viscosity Sensitivity of Cyclodextrin Polypseudorotaxane with Light-Active Rotor Graft. *Langmuir* **2009,** *25*, 3482-3486.
96. Kottas, G. S.; Clarke, L. I.; Horinek, D.; Michl, J., Artificial Molecular Rotors. *Chem. Rev.* **2005,** *105*, 1281-1376.
97. Haidekker, M. A.; Theodorakis, E. A., Environment-sensitive behavior of fluorescent molecular rotors. *J. Biol. Eng.* **2010,** *4* (1), 11.
98. Haidekker, M. A.; Nipper, M.; Mustafic, A.; Lichlyter, D.; Dakanali, M.; Theodorakis, E. A., Dyes with Segmental Mobility: Molecular Rotors. *Advanced Fluorescence Reporters in Chemistry and Biology I: Fundamentals and Molecular Design. New York: Springrt* **2010,** *8*, 267-308.
99. Stsiapura, V. I.; Maskevich, A. A.; Kuzmitsky, V. A.; Uversky, V. N.; Kuznetsova, I. M.; Turoverov, K. K., Thioflavin T as a Molecular Rotor: Fluorescent Properties of Thioflavin T in Solvents with Different Viscosity. *J. Phys. Chem. B* **2008,** *112* (49), 15893-15902.
100. Levitt, J. A.; Kuimova, M. K.; Yahioglu, G.; Chung, P.-H.; Suhling, K.; Phillips, D., Membrane-Bound Molecular Rotors Measure Viscosiy in Live Cells via Fluorescence Lifetime Imaging. *J. Phys. Chem. C* **2009,** *113*, 11634-11642.
101. Uzhinov, B. M.; Ivanov, V. L.; Melnikov, M. Y., Molecular rotors as luminescence sensors of local viscosity and viscous flow in solutions and organized systems. *Russ. Chem. Rev.* **2011,** *80* (12), 1179-1190.
102. Khurana, R.; Coleman, C.; Ionescu-Zanetti, C.; Carter, S. A.; Krishna, V.; Grover, R. K.; Roy, R.; Singh, S., Mechanism of thioflavin T binding to amyloid fibrils. *J. Struct. Biol.* **2005,** *151* (3), 229-238.
103. Förster, T.; Hoffman, G., Die Viskositätsabhängigkeit der Fluoreszenzquantenausbeuten einiger Farbstoffsysteme. *Z. Phys. Chem.* **1971,** *75*, 63-76.
104. Nivaggioli, T.; Tsao, B.; Alexandridis, P.; Hatton, T. A., Microviscosity in Pluronic and Tetronic Poly(ethylene oxide) -Poly(propylene oxide) Block Copolymer Micelles. *Langmuir* **1995,** *11*, 119-126.
105. Berezin, M. Y.; Lee, H.; Akers, W.; Nikiforovich, G.; Achilefu, S., Ratiometric Analysis of Fluorescence Lifetime for Probing Binding Sites in Albumin with Near-Infrared Fluorescent Molecular Probes. *Photochem. Photobiol.* **2007,** *83* (6), 1371-1378.
106. Abugo, O., Fluorescence Properties of Rhodamine 800 in Whole Blood and Plasma. *Anal. Biochem.* **2000,** *279* (2), 142-150.
107. Jameson, D. M.; Ross, J. A., Fluorescence Polarization/Anisotropy in Diagnostics and Imaging. *Chem. Rev.* **2010,** *110*, 2685-2708.
108. Barroso, M. M., Quantum Dots in Cell Biology. *J. Histochem. Cytochem.* **2011,** *59* (3), 237-251.

109. Kuimova, M. K.; Botchway, S. W.; Parker, A. W.; Balaz, M.; Collins, H. A.; Anderson, H. L.; Suhling, K.; Ogilby, P. R., Imaging intracellular viscosity of a single cell during photoinduced cell death. *Nat. Chem.* **2009,** *1* (1), 69-73.
110. Gleason, M. M.; Medow, M. S.; Tulenko, T. N., Excess membrane cholesterol alters calcium movements, cytosolic calcium levels, and membrane fluidity in arterial smooth muscle cells. *Circ. Res.* **1991,** *69*, 216-227.
111. Nadiv, O.; Shinitzky, M.; Manu, H.; Hecht, D.; Charles T. Roberts, J.; Leroith, D.; Zick, Y., Elevated protein tyrosine phosphatase activity and increased membrane viscosity are associated with impaired activation of the insulin receptor kinase in old rats. *Biochem. J.* **1994,** *298*, 443-450.
112. Shinitzky, M., Membrane fluidity in malignancy. *Biochim. Biophys. Acta* **1984,** *738*, 251-261.
113. Koike, T.; Ishida, G.; Taniguchi, M.; Higaki, K.; Ayaki, Y.; Saito, M.; Sakakihara, Y.; Iwamori, M.; Ohno, K., Decreased membrane fluidity and unsaturated fatty acids in Niemann–Pick disease type C fibroblasts. *Biochim. Biophys. Acta* **1998,** *1406*, 327-335.
114. Fedosov, D. A.; Panb, W.; Caswell, B.; Gompper, G.; Karniadakis, G. E., Predicting human blood viscosity in silico. *Proc. Natl. Acad. Sci. U.S.A.* **2011,** *108* (29), 11772-11777.
115. Lim, C. T.; Dao, M.; Suresh, S.; Sow, C. H.; Chew, K. T., Large deformation of living cells using laser traps. *Acta Materialia* **2004,** *52* (7), 1837-1845.
116. Fontes, A.; Castro, M. L. B.; Brandão, M. M.; Fernandes, H. P.; Thomaz, A. A.; Huruta, R. R.; Pozzo, L. Y.; Barbosa, L. C.; Costa, F. F.; Saad, S. T. O.; Cesar, C. L., Mechanical and electrical properties of red blood cells using optical tweezers. *J. Opt.* **2011,** *13* (4), 044012.
117. Pesce, G.; Sasso, A.; Fusco, S., Viscosity measurements on micron-size scale using optical tweezers. *Rev. Sci. Instrum.* **2005,** *76* (11), 115105.
118. Sankaran, J.; Manna, M.; Guo, L.; Kraut, R.; Wohland, T., Diffusion, Transport, and Cell Membrane Organization Investigated by Imaging Fluorescence Cross-Correlation Spectroscopy. *Biophysical Journal* **2009,** *97* (9), 2630-2639.
119. Haidekker, M. A.; Theodorakis, E. A., Molecular rotors-fluorescent biosensors for viscosity and flow. *Org. Biomol. Chem.* **2007,** *5* (11), 1669-1678.
120. Peng, X.; Yang, Z.; Wang, J.; Fan, J.; He, Y.; Song, F.; Wang, B.; Sun, S.; Qu, J.; Qi, J.; Yan, M., Fluorescence Ratiometry and Fluorescence Lifetime Imaging: Using a Single Molecular Sensor for Dual Mode Imaging of Cellular Viscosity. *Journal of the American Chemical Society* **2011,** *133* (17), 6626-6635.
121. Fushimi, K.; Verkman, A. S., Low Viscosity in the Aqueous Domain of Cell Cytoplasm Measured by Picosecond Polarization Microfluofimetry. *J. Cell Biol.* **1991,** *112*, 719-725.
122. Luby-Phelps, K.; Mujumdar, S.; Mujumdar, R. B.; Ernst, L. A.; Galbraith, W.; Waggoner, A. S., A Novel Fluorescence Ratiometric Method Confirms the Low Solvent Viscosity of the Cytoplasm. *Biophys. J.* **1993,** *65*, 236-242.
123. Srivastava, A.; Krishnamoorthy, G., Cell Type and Spatial Location Dependence of Cytoplasmic Viscosity Measured by Time-Resolved Fluorescence Microscopy. *Arch. Biochem. Biophys.* **1997,** *340* (2), 159-167.
124. Kalwarczyk, T.; Ziebacz, N.; Bielejewska, A.; Zaboklicka, E.; Koynov, K.; Szymański, J.; Wilk, A.; Patkowski, A.; Gapiński, J.; Butt, H.-J. r.; Hołyst, R., Comparative Analysis of Viscosity of Complex Liquids and Cytoplasm of Mammalian Cells at the Nanoscale. *Nano Lett.* **2011,** *11* (5), 2157-2163.

125. Nipper, M.; Majd, S.; Mayer, M.; Lee, J.; Theodorakis, E.; Haidekker, M., Characterization of changes in the viscosity of lipid membranes with the molecular rotor FCVJ. *Biochim. Biophys. Acta* **2008,** *1778* (4), 1148-1153.
126. Kung, C. E.; Reed, J. K., Microviscosity Measurements of Phospholipid Bilayers Using Fluorescent Dyes That Undergo Torsional Relaxation. *Biochem. J.* **1986,** *25*, 6114-6121.
127. Nipper, M. E.; Dakanali, M.; Theodorakis, E.; Haidekker, M. A., Detection of liposome membrane viscosity perturbations with ratiometric molecular rotors. *Biochimie* **2011,** *93* (6), 988-994.
128. Kuimova, M. K.; Yahioglu, G.; Levitt, J. A.; Suhling, K., Molecular Rotor Measures Viscosity of Live Cells via Fluorescence Lifetime Imaging. *J. Am. Chem. Soc.* **2008,** *130* (21), 6672-6673.
129. Levitt, J. A.; Chung, P.-H.; Kuimova, M. K.; Yahioglu, G.; Wang, Y.; Qu, J.; Suhling, K., Fluorescence Anisotropy of Molecular Rotors. *ChemPhysChem* **2011,** *12* (3), 662-672.
130. Dix, J. A.; Verkman, A. S., Mapping of fluorescence anisotropy in living cells by ratio imaging-Application to cytoplasmic viscosity. *Biophys. J.* **1990,** *57*, 231-240.
131. Periasamy, N.; Armijo, M.; Verkman, A., Picosecond Rotation of Small Polar Fluorophores in the Cytosol of Sea Urchin Eggs. *Biochemistry* **1991,** *30* (51), 11836-11841.
132. Swaminathan, R.; Hoang, C. P.; Verkman, A. S., Photobleaching Recovery and Anisotropy Decay of Green Fluorescent Protein GFP-S65T in Solution and Cells: Cytoplasmic Viscosity Probed by Green Fluorescent Protein Translational and Rotational Diffusion. *Biophys. J.* **1997,** *72*, 1900-1907.
133. Wandelt, B.; Cywinski, P.; Darling, G. D.; Stranix, B. R., Single cell measurement of micro-viscosity by ratio imaging of fluorescence of styrylpyridinium probe. *Biosens. Bioelectron.* **2005,** *20* (9), 1728-1736.
134. Tregidgo, C., Advances in Time-resolved Fluorescence Microscopy, Ph.D Thesis. **2007**.
135. Becker, W., The bh TCSPC Handbook, Third Edition, Becker & Hickl GmbH. **2008**.
136. O'Connor, D. V.; Phillips, D., Time-correlated Single Photon Counting. *Academic Press* **1984**.
137. Mandel, L.; Wolf, E., Coherence Properties of Optical Fields. *Rev. Mod. Phys.* **1965,** *37* (2), 231-287.
138. Becker, W., Advanced Time-Correlated Single Photon Counting Techniques. Springer-Verlag Berlin. **2005**.
139. Patting, M.; Wahl, M.; Kapusta, P.; Erdmann, R., Dead-time effects in TCSPC data analysis. *Proc. of SPIE* **2007,** *6583*, 658307-1-658307-10.
140. Birch, D. J. S.; Imhof, R. E., Time-Domain Fluorescence Spectroscopy Using Time-Correlated Single-Photon Counting. *Joseph R. Lakowicz (Ed.), Topics in Fluorescence Spectroscopy, Vol. 1, Plenum Press, New York* **1991**, 1-95.
141. Barber, P. R.; Ameer-Beg, S. M.; Gilbey, J.; Carlin, L. M.; Keppler, M.; Ng, T. C.; Vojnovic, B., Multiphoton time-domain fluorescence lifetime imaging microscopy: practical application to protein-protein imteractions using global analysis. *J. R. Soc. Interface* **2009,** *6*, S93-S105.
142. Luchowski, R.; Gryczynski, Z.; Sarkar, P.; Borejdo, J.; Szabelski, M.; Kapusta, P.; Gryczynski, I., Instrument response standard in time-resolved fluorescence. *Rev. Sci. Instrum.* **2009,** *80* (3), 033109.

143. Allen, B. D.; Benniston, A. C.; Harriman, A.; Rostron, S. A.; Yu, C., The photophysical properties of a julolidene-based molecular rotor. *Phys. Chem. Chem. Phys.* **2005,** *7*, 3035-3040.
144. Li, L.-Q.; Davis, L. M., Single photon avalanche diode for single molecule detection. *Rev. Sci. Instrum.* **1993,** *64* (6), 1524-1529.
145. Becker, W.; Su, B.; Holub, O.; Weisshart, K., FLIM and FCS detection in laser-scanning microscopes: Increased efficiency by GaAsP hybrid detectors. *Microsc. Res. Tech.* **2011,** *74*, 804-811.
146. http://sales.hamamatsu.com/assets/applications/ETD/PhotonCounting_TPHO9001E04.pdf, Technical Information-Photon Counting Using Photomultiplier Tubes, HANAMATSU. **2005**.
147. http://sales.hamamatsu.com/assets/pdf/catsandguides/PMT_modules_TPMO0008E02.pdf, Photomultiplier tube modules, HANAMATSU. **2007**.
148. K.K., H. P., R10467U-40 Test Data Sheet. **2010**.
149. Bernd, W., Influence of solvent viscosity on excited state lifetime and fluorescence quantum yield of dye molecules. *Chem. Phys.* **1982,** *66* (3), 351-355.
150. Kaschke, M.; Kleinschmidt, J.; Wilhelmi, B., Computer Simulations of Viscosity Dependent Molecular Relaxation Processes. *Laser Chem.* **1985,** *5*, 119-132.
151. Haidekker, M. A.; L'Heureux, N.; Frangos, J. A., Fluid shear stress increases membrane fluidity in endothelial cells: a study with DCVJ fluorescence. *Am. J. Physiol. Heart Circ. Physiol.* **2000,** *278*, H1406.
152. Haidekker, M. A.; Ling, T.; Anglo, M.; Stevens, H. Y.; Frangos, J. A.; Theodorakis, E. A., New fluorescent probes for the measurement of cell membrane viscosity. *Chem. Biol.* **2001,** *8*, 123-131.
153. Paul, A.; Samanta, A., Free Volume Dependence of the Internal Rotation of a Molecular Rotor Probe in Room Temperature Ionic Liquids. *J. Phys. Chem. B* **2008,** *112*, 16626-16632.
154. Howell, S.; Dakanali, M.; Theodorakis, E. A.; Haidekker, M. A., Intrinsic and Extrinsic Temperature-Dependency of Viscosity-Sensitive Fluorescent Molecular Rotors. *J. Fluoresc.* **2012,** *22* (1), 457-465.
155. Strickler, S. J.; Berg, R. A., Relationship between Absorption Intensity and Fluorescence Lifetime of Molecules. *J. Chem. Phys.* **1962,** *37* (4), 814-822.
156. El-Bayoumi, M. A.; Dalle, J.-P.; O'Dwyer, M. F., Fluorescence Lifetimes of Molecules that Undergo Large Configurational Changes upon Excitation. *J. Am. Chem. Soc.* **1970,** *92*, 3494-3495.
157. Frank, H. A.; Desamero, R. Z. B.; Chynwat, V.; Gebhard, R.; Hoef, I. v. d.; Jansen, F. J.; Lugtenburg, J.; Gosztola, D.; Wasielewski, M. R., Spectroscopic Properties of Spheroidene Analogs Having Different Extents of π-Electron Conjugation. *J. Phys. Chem. A* **1997,** *101*, 149-157.
158. Susdorf, T.; Bansal, A. K.; Penzkofer, A.; Guo, S.-L.; Shi, J.-M., Absorption and emission spectroscopic characterization of some azo dyes and a diamino-maleonitrile dye. *Chem. Phys.* **2007,** *333* (1), 49-56.
159. Sun, Y.-P.; Wang, P.; Hamilton, N. B., Fluorescence Spectra and Quantum Yields of Buckminsterfullerene (C60) in Room-Temperature Solutions. No Excitation Wavelength Dependence. *J. Am. Chem. Soc.* **1993,** *115*, 6378-6381.

160. Cohen, B.; Crespo-Hernandez, C. E.; Kohler, B., Strickler-Berg analysis of excited singlet state dynamics in DNA and RNA nucleosides. *Faraday Discuss.* **2004,** *127*, 137-147.
161. Hui Jin, M. L.; Arzhantsev, S.; Li, X.; Maroncelli, M., Photophysical Characterization of Benzylidene Malononitriles as Probes of Solvent Friction. *J. Phys. Chem. B* **2010,** *114*, 7565-7578.
162. Toptygin, D.; Savtchenko, R. S.; Meadow, N. D.; Roseman, S.; Brand, L., Effect of the Solvent Refractive Index on the Excited-State Lifetime of a Single Tryptophan Residue in a Protein. *J. Phys. Chem. B* **2002,** *106* (14), 3724-3734.
163. Jędrzejewska, B.; Pietrzak, M.; Pączkowski, J., Solvent Effects on the Spectroscopic Properties of Styrylquinolinium Dyes Series. *J. Fluoresc.* **2010,** *20* (1), 73-86.
164. Loutfy, R. O.; Law, K. Y., Electrochemistry and Spectroscopy of Intramolecular Charge-Transfer Complexes. p-N,N-Dialkylamlnobenzylidenemalononitrlles. *J. Phys. Chem.* **1980,** *84*, 2803-2808.
165. Kawski, A., On the Estimation of Excited-State Dipole Moments from Solvatochromic Shifts of Absorption and Fluorescence Spectra. *Z. Naturforsch.* **2002,** *57a*, 255-262.
166. Acemioglu, B.; Arik, M.; Efeoglu, H.; Onganer☼, Y., Solvent effect on the ground and excited state dipole moments of fluorescein. *J. Mol. Struct. (THEOCHEM)* **2001,** *548*, 165-171.
167. Raikar, U. S.; Tangod, V. B.; Mannopantar, S. R.; Mastiholi, B. M., Ground and excited state dipole moments of coumarin 337 laser dye. *Opt. Commun.* **2010,** *283* (21), 4289-4292.
168. Akerlof, G., Dielectric Constants of Some Organic Solvent-Water Mixtures at Various Temperature. *J. Am. Chem. Soc.* **1932,** *54*, 4125-4139.
169. Reynolds, J. A.; Hough, J. M., Formulae for Dielectric Constant of Mixtures. *Proc. Phys. Soc. B* **1957,** *70*, 769-775.
170. Jouyban, A.; Soltanpour, S.; Chan, H.-K., A simple relationship between dielectric constant of mixed solvents with solvent composition and temperature. *Int. J. Pharm.* **2004,** *269* (2), 353-360.
171. Suhling, K.; Levitt, J. A.; Chung, P.-H.; Kuimova, M. K.; Yahioglu, G., Fluorescence Lifetime Imaging of Molecular Rotors in Living Cells. *J. Vis. Exp.* **2012,** *60*, e2925.
172. M. Ravi, A. S.; Radhakrishnan, T. P., Excited State Dipole Moments form an Efficient Analysis of Solvatochromic Stokes Shift Data. *J. Phys. Chem.* **1994,** *98*, 9133-9136.
173. Kendall, J.; Monroe, K. P., The viscosity of liquids. II The viscosity-composition curve for ideal liquid mixtures. *J. Am. Chem. Soc.* **1917,** *39*, 1787-1802.
174. Jouyban, A.; Khoubnasabjafari, M.; Vaez-Gharamaleki, Z.; Fekari, Z.; Jr., W. E. A., Calculation of the viscosity of binary liquids at various temperature using Jouyban-Acree Model. *Chem. Pharm. Bull.* **2005,** *53*, 519-523.
175. Newman, A. A., Physical Properties of Glycerol, Glycerol, Leonard Hill, London. **1968**, 15.
176. Kawski, A.; Bojarski, P.; Kukliński, B., Estimation of ground- and excited-state dipole moments of Nile Red dye from solvatochromic effect on absorption and fluorescence spectra. *Chem. Phys. Lett.* **2008,** *463* (4-6), 410-412.
177. Williams, A. T. R.; Winfield, S. A.; Miller, J. N., Relative fluorescence quantum yields using a computer-controlled luminescence spectrometer. *The Analyst* **1983,** *108* (1290), 1067.

178. Dhami, S.; Mello, A. J. D.; Rumbles, G.; Bishop, S. M.; Phillips, D.; Beeby, A., Phthalocyanine Fluorescence at High-Concentration - Dimers or Reabsorption Effect? *Photochem. Photobiol.* **1995,** *61* (4), 341-346.
179. Weber, G.; Teale, F. W. J., Determination of the absolute quantum yield of fluorescent solutions. *Trans. Faraday Soc.* **1957,** *53*, 646-655.
180. Loutfy, R. O., Fluorescence probes for polymer free-volume. *Pure Appl. Chem.* **1986,** *58*, 1239-1248.
181. Loutfy, R. O.; Arnold, B. A., Effect of Viscosity and Temperature on Torsional Relaxation of Molecular Rotors. *J. Phys. Chem.* **1982,** *86*, 4205-4211.
182. McLoskey, D.; Campbell, D.; Allison, A.; Hungerford, G., Fast time-correlated single-photon counting fluorescence lifetime acquisition using a 100 MHz semiconductor excitation source. *Meas. Sci. Technol.* **2011,** *22* (6), 067001.
183. Doolittle, A. K., Studies in Newtonian Flow. III. The Dependence of the Viscosity of Liquids on Molecular Weight and Free Space (in Homologous Series). *J. Appl. Phys.* **1952,** *23* (2), 236-239.
184. Greenspan, P.; Fowler, S. D., Spectrofluorometric studies of the lipid probe, nile red. *J. Lipid Res.* **1985,** *26*, 781-789.
185. Sackett, D. L.; Wolff, J., Nile Red As a Polarity-Sensitive Fluorescent Probe of Hydrophobic Protein Surfaces. *Anal. Biochem.* **1987,** *167*, 228-234.
186. Welte, Michael A., Fat on the move: intracellular motion of lipid droplets. *Biochem. Soc. Trans.* **2009,** *37* (5), 991-996.
187. Guo, Y.; Cordes, K. R.; Farese, R. V.; Walther, T. C., Lipid droplets at a glance. *J. Cell Sci.* **2009,** *122* (6), 749-752.
188. Suzuki, M.; Shinohara, Y.; Ohsaki, Y.; Fujimoto, T., Lipid droplets: size matters. *J. Electron Microsc.* **2011,** *60* (supplement 1), S101-S116.
189. Fujimoto, T.; Ohsaki, Y.; Cheng, J.; Suzuki, M.; Shinohara, Y., Lipid droplets: a classic organelle with new outfits. *Histochem. Cell Biol.* **2008,** *130* (2), 263-279.
190. Edward, J. T., Molecular Volumes and the Stokes-Einstein Equation. *J. Chem. Educ.* **1970,** *47* (4), 261-270.
191. Gutkowski, K. I.; Japas, M. L.; Aramendía, P. F., Fluorescence of dicyanovinyl julolidine in a room-temperature ionic liquid. *Chem. Phys. Lett.* **2006,** *426* (4-6), 329-333.
192. Rizzo, M. A.; Piston, D. W., High-Contrast Imaging of Fluorescent Protein FRET by Fluorescence Polarization Microscopy. *Biophys. J.* **2005,** *88* (2), L14-L16.
193. Sergent, N.; Levitt, J. A.; Green, M.; Suhling, K., Rapid wide-field photon counting imaging with microsecond time resolution. *Opt. Express* **2010,** *18* (24), 25292-25298.
194. Picou, C. L.; Stevens, E. D.; Shah, M.; Boyer, J. H., Structure of 4,4-Difluoro- 1,3,5,7,8-pentamethyl-3a,4a-diaza-4-bora-s-indacene. *Acta Cryst.* **1990,** *C46*, 1148-1150.
195. Prieto, J. B.; Arbeloa, F. L.; Martınez, V. M.; Arbeloa, I. L., Theoretical study of the ground and excited electronic states of pyrromethene 546 laser dye and related compounds. *Chem. Phys.* **2004,** *296* (1), 13-22.
196. Schaffer, J.; Volkmer, A.; Eggeling, C.; Subramaniam, V.; Striker, G.; Seidel, C. A. M., Identification of Single Molecules in Aqueous Solution by Time-Resolved Fluorescence Anisotropy. *J. Phys. Chem. A* **1999,** *103*, 331-336.
197. Vishwasrao, H. D., Conformational Dependence of Intracellular NADH on Metabolic State Revealed by Associated Fluorescence Anisotropy. *J. Biol. Chem.* **2005,** *280* (26), 25119-25126.

198. Ko, C. W.; Wei, Z.; Marsh, R. J.; Armoogum, D. A.; Nicolaou, N.; Bain, A. J.; Zhou, A.; Ying, L., Probing nanosecond motions of plasminogen activator inhibitor-1 by time-resolved fluorescence anisotropy. *Mol. BioSyst.* **2009,** *5* (9), 1025-1031.
199. Bhattacharya, B.; Nakka, S.; Guruprasad, L.; Samanta, A., Interaction of Bovine Serum Albumin with Dipolar Molecules: Fluorescence and Molecular Docking Studies. *J. Phys. Chem. B* **2009,** *113*, 2143-2150.
200. Yu, Q.; Heikal, A. A., Two-photon autofluorescence dynamics imaging reveals sensitivity of intracellular NADH concentration and conformation to cell physiology at the single-cell level. *J. Photochem. Photobiol. B* **2009,** *95* (1), 46-57.
201. Zheng, W.; Li, D.; Qu, J. Y., Monitoring changes of cellular metabolism and microviscosity in vitro based on time-resolved endogenous fluorescence and its anisotropy decay dynamics. *J. Biomed. Opt.* **2010,** *15* (3), 037013.
202. Ludescher, R. D.; Peting, L.; Hudson, S.; Hudson, B., Time-resolved fluorescence anisotropy for systems with lifetime and dynamic heterogeneity. *Biophys. Chem.* **1987,** *28*, 59-75.
203. Corporation, D. C., XIAMETER® PMX-200 Silicone Fluid, 50-1,000 CS. **2010,** *Ref. No. 95-516B-01*.
204. Cowie, J. M. G.; Toporowski, P. M., Association in the Binary Liquid System Dimethyl Sulphoxide-Water. *Can. J. Chem.* **1961,** *39*, 2240-2243.
205. Ben-Amotz, D.; Harris, C. B., Torsional dynamics of molecules on barrierless potentials in liquids. I. Temperature and wavelength dependent picosecond studies of triphenyl-methane dyes. *J. Chem. Phys.* **1987,** *86* (9), 4856-4870.
206. Wen, W.; Huang, X.; Yang, S.; Lu, K.; Sheng, P., The giant electrorheological effect in suspensions of nanoparticles. *Nat. Mater.* **2003,** *2* (11), 727-730.
207. Suhling, K.; Siegel, J.; Phillips, D.; French, P. M. W.; Leveque-Fort, S.; Webb, S. E. D.; Davis, D. M., Imaging the Environment of Green Fluorescent Protein. *Biophys. J.* **2002,** *83*, 3589-3595.
208. Hawe, A.; Sutter, M.; Jiskoot, W., Extrinsic Fluorescent Dyes as Tools for Protein Characterization. *Pharmaceutical Research* **2008,** *25* (7), 1487-1499.
209. Arbeloa, F. L.; Arbeloa, T. L.; Arbeloa, I. L., Electronic spectroscopy of pyrromethene 546. *Photochem. Photobiol.* **1999,** *121*, 188-182.
210. http://www.exciton.com/pdfs/p546.pdf, Pyrromethene 546. *Exciton*.
211. López Arbeloa, F.; Bañuelos, J.; Martínez, V.; Arbeloa, T.; López Arbeloa, I., Structural, photophysical and lasing properties of pyrromethene dyes. *Int. Rev. Phys. Chem.* **2005,** *24* (2), 339-374.
212. Bergstrom, F.; Mikhalyov, I.; Hagglof, P.; Wortmann, R.; Ny, T.; Johansson, L. B.-Å., Dimers of Dipyrrometheneboron Difluoride (BODIPY) with Light Spectroscopic Applications in Chemistry and Biology. *J. Am. Chem. Soc.* **2002,** *124*, 196-204.
213. Acebal, P.; Blaya, S.; Carretero, L., Ab initio study of absorption and emission spectra of PM567. *Chem. Phys. Lett.* **2003,** *374* (3-4), 206-214.
214. Calzaferri, G.; Rytz, R., Electronic Transition Oscillator Strength by the Extended Huckel Molecular Orbital Method. *J. Phys. Chem.* **1995,** *99*, 12141-12150.
215. Schmitt, A.; Hinkeldey, B.; Wild, M.; Jung, G., Synthesis of the Core Compound of the BODIPY Dye Class: 4,4´-Difluoro-4-bora-(3a,4a)-diaza-s-indacene. *J. Fluoresc.* **2009,** *19* (4), 755-758.

216. Prieto, J. B.; Arbeloa, F. L.; Martinez, V. M.; Lopez, T. A.; Arbeloa, I. L., Structural and spectroscopic characteristics of Pyrromethene 567 laser dye. A theoretical approach. *Phys. Chem. Chem. Phys.* **2004,** *6*, 4247-4253.
217. Yu, Q.; Proia, M.; Heikal, A. A., Integrated biophotonics approach for noninvasive and multiscale studies of biomolecular and cellular. *J. Biomed. Opt.* **2008,** *13*, 041315.
218. Ghoneim, N., Photophysics of Nile red in solution Steady state spectroscopy. *Spectrochimica Acta Part A* **2000,** *56*, 1003-1010.
219. Sarkar, N.; Das, K.; Nath, D. N.; Bhattacharyya, K., Twisted Charge Transfer Process of Nile Red in Homogeneous Solution and in Faujasite Zeolite. *Langmuir* **1994,** *10*, 326-329.
220. Yablon, D. G.; Schilowitz, A. M., Solvatochromism of Nile Red in Nonpolar Solvents. *Appl. Spectrosc.* **2004,** *48* (7), 843-847.
221. Grant, D. M.; Zhang, W.; McGhee, E. J.; Bunney, T. D.; Talbot, C. B.; Kumar, S.; Munro, I.; Dunsby, C.; Neil, M. A. A.; Katan, M.; French, P. M. W., Multiplexed FRET to Image Multiple Signaling Events in Live Cells. *Biophys. J.* **2008,** *95* (10), L69-L71.